SUPERFLUID DENSITY MEASUREMENTS OF HIGH-TEMPERATURE SUPERCONDUCTING FILMS

BY

KEVIN DANIEL OSBORN

B.S., Mary Washington College, Va., 1992
M.S., University of Tennessee at Knoxville, 1995

THESIS

Submitted in partial fulfillment of the requirements
for the degree of Doctor of Philosophy in Physics
in the Graduate College of the
University of Illinois at Urbana-Champaign, 2001

Urbana, Illinois

SUPERFLUID DENSITY MEASUREMENTS OF HIGH-TEMPERATURE SUPERCONDUCTING FILMS

Kevin Daniel Osborn, Ph.D.
Department of Physics
University of Illinois at Urbana-Champaign, 2001
Dale J. Van Harlingen, Advisor

We have constructed a precision two-coil inductive system suitable for measuring the superfluid density of superconducting films. With this system we measure several intrinsic properties of $YBa_2Cu_3O_{7-x}$ (YBCO) and $Bi_2Sr_2CaCu_2O_{8+\delta}$ (Bi-2212) films. Two competing models of the pseudogap are compared to the temperature dependence of the superfluid density as a function of doping in Bi-2212. Near zero temperature, a maximum in the superfluid density as a function of hole doping is observed at approximately 0.19 holes per unit Cu, in agreement with a model of the pseudogap with competing order. At temperatures close to the T_c, the superfluid density exhibits critical phase fluctuations described by an XY model. These phase fluctuations are compared to a model of the pseudogap described by preformed pairs. In contrast to previous reports on YBCO films, we find that the phase transition in a YBCO film is described by 3D-XY critical fluctuations. In heavily underdoped Bi-2212, we find a drop in superfluid density that is approximately described by a Kosterlitz-Thouless-Berezinskii (KTB) transition. However, in Bi-2212 films near optimal and critical doping, we find evidence for 3D-XY static and dynamic fluctuations. The dynamic critical exponent, z, in thin optimally-doped Bi-2212 films is directly observed as diffusive (z=2) at T_c when the correlation length exceeds the film thickness (D=2). In the 3D regime we find evidence for $z \approx 1.5$, indicative of a propagating mode.

This thesis is dedicated to my wife, Christine. Her friendship and encouragement has been invaluable throughout this research.

Acknowledgments

There are many ways in which people contributed to this work, from encouragement to assistance. My advisor, Dale Van Harlingen, offered opinions, suggestions, and support throughout this research for which I am very grateful. In addition, I thank him for many informal discussions on physics research that have sustained and broadened my interests in physics.

I am very grateful for the access to high quality samples. I would like to thank Jim Eckstein for encouraging me to measure Bi-2212 films from his research group with the two-coil inductive technique, and Seongshik Oh for growing several epitaxially-grown Bi-2212 films presented in this work. I also acknowledge Tiziana Di Luccio for providing Sr doped Bi-2212 films. Laser-ablated YBCO films were provided by Chris Michaels, William Neils, and Joe Hilliard. I also thank John Corson and Joe Orenstein for discussions on their terahertz spectroscopy measurements on Bi-2212 films.

Next I would like to thank members of the DVH Group. Brian Yanoff, Britton Plourde, Joe Hilliard, Mark Wistrom, William Neils, Tony Bonetti, and Trevis Crane have all assisted with some piece of lab equipment, for which I am very grateful. Tony Banks, an unofficial member, also deserves special mention for maintaining various MRL facilities. I would also like to thank Ray Strange for loaning me a turbo pumping station, on many occasions.

I am also thankful for interactions with theorists in the physics department. Harry Westfahl, Vivek Aji, and Nigel Goldenfeld have helped in the interpretation of my results. I would like to thank Simon Kos, Dan Sheehy, and Revaz Ramazashvili for many helpful discussions on extending the theory and utility of the two-coil inductive technique. Paul Goldbart deserves credit for hosting the Mesoscopic Seminar. The seminar is a great forum for learning important topics in condensed matter physics and has led me into interesting discussions with Adam Abeyta, Igor Roshchin, Horacio Castillo, Inanc Adagideli and others.

Lastly, I gratefully acknowledge the support of the Department of Energy under award number DEFG02-96ER45439.

Table of Contents

1 Phase Transitions in High-Temperature Superconductors

The superfluid density is intimately tied to the properties of a high-temperature superconductor. At zero temperature the superfluid density is proportional to the density of superconducting electrons over the effective mass. Near the transition temperature, the superfluid density is renormalized by phase fluctuations, which are strong in the high-temperature superconductors due to the small coherence length, large penetration depth, large anisotropy, and high transition temperature.

Since the experiments in this thesis study the doping dependence of the superfluid density with emphasis on the phase transition, I will cover various concepts related to the superfluid density in high-temperature superconductors. First, I will introduce the phase diagram and discuss implications on the measured superfluid density. Then I will describe how critical phase fluctuations in 2D-XY and 3D-XY models vary from mean-field theory. Finally, I will discuss the predictions of the 3D-XY Model and the Coupled Layer Model, on the phase transition in high-temperature superconductors.

1.1 High-Temperature Superconductor Phase Diagram

A high-temperature superconductor (HTS) can enter into many different states by varying the doping level. Figure 1 shows the phase diagram for a HTS as a function of temperature and doping, where the superconducting (SC) state is found below the

transition temperature T_c. The HTS is an antiferromagnet (AF) at very low doping and has quasiparticles at high doping, indicative of a Fermi Liquid (FL). Between these two states are the pseudogap (PG) regime and the superconducting (SC) state. These latter two neighboring regions of the phase diagram seem contradictory since the pseudogap regime has a very low density of carriers and is similar to a Mott insulator, whereas the superconducting state (SC) is formed with electrons despite the unscreened Coulomb repulsion.

Studying the transition from the superconducting state into the pseudogap regime may lead to a greater understanding of both phases since they share a phase boundary. The pseudogap regime is identified as a suppression in the density of states, which persists up to a temperature T*, observed in many experiments on the underdoped side of the phase diagram[1]. As shown in Figure 1, there are two proposed shapes of the T* line near the superconducting state in the phase diagram, which correspond to two contrasting models of the interaction between the pseudogap and the superconducting regions. The models are the preformed-pair model and the second-order-parameter model, which have T* lines drawn as “a” and “b”, respectively.

The preformed-pair model[2], proposed by Emery and Kivelson, describes the pseudogap with pairs that form as a precursor to superconductivity. Since underdoped high-temperature superconductors generally have a lower superfluid density and a higher anisotropy than overdoped high-temperature superconductors, fluctuations may significantly limit the transition temperature in the underdoped cuprates. Studies by

Uemura on the underdoped cuprates show that the transition temperature increases linearly with the zero-temperature superfluid density[3]. Emery and Kivelson pointed out that the transition temperature in a wide array of the high-temperature superconductors can be estimated from the zero-temperature superfluid density in a model of classical fluctuations. In the preformed-pair model, the T* line is expected to merge with the superconducting transition line, as shown by curve "a" in Figure 1, since phase fluctuations describe the beginning of the pseudogap as doping is decreased.

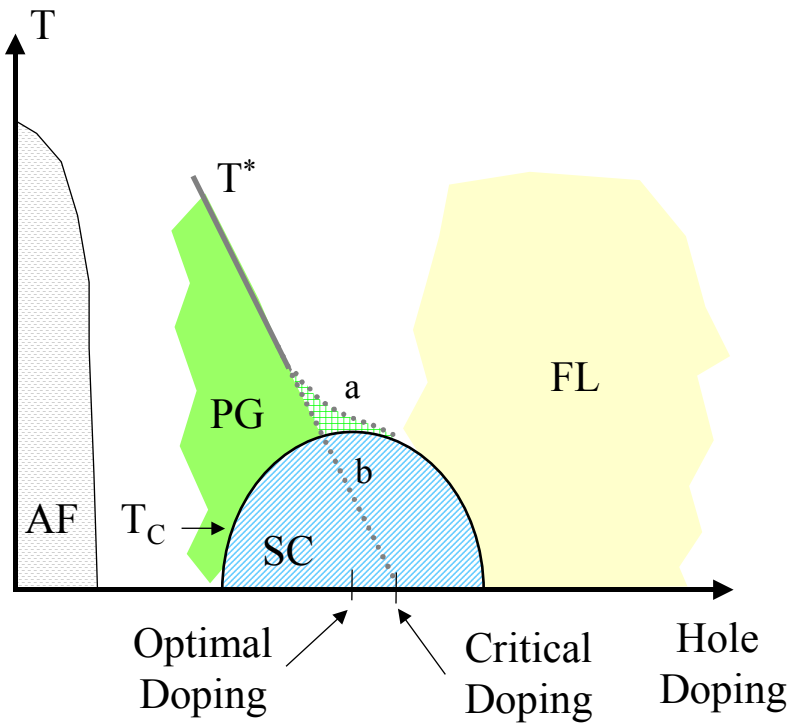

Figure 1: High-temperature superconductor phase diagram. Antiferromagnetic (AF), Fermi liquid (FL), pseudogap (PG) and superconducting (SC) regions are shown.

In more recent theories T* describes the temperature for charge within stripes to develop superconducting correlations[4]. In this version of the preformed-pair model there is a

mean-field temperature between T* and T_C, where the stripes Josephson couple, and the bulk superconducting order parameter is formed[5]. The mean-field temperature will be discussed more below. At T_C the superconducting stripes produce sufficient phase stiffness for long-range order.

In contrast, the second order-parameter model asserts that an order parameter describing the pseudogap competes with the superconducting order. Loram and Tallon have observed that the jump in the electronic specific heat decreases as the psuedogap forms, implying the pseudogap removes Fermi surface from the superconducting state[6, 7]. One possible second order-parameter model describes the pseudogap order as a d-density wave, which interacts with the superconducting order parameter[8].

Loram and Tallon have argued that T* crosses through the superconducting region and reaches T=0 at critical doping (T* is shown as curve "b" in Figure 1)[9]. Critical doping has been observed in several measurements at approximately 0.19 holes per unit cell, where the condensation energy is a maximum[10], and may implicate a quantum critical point[9]. In addition, at critical doping the transition temperature is reduced less by impurities than other doping states, and is therefore more robust[11,12]. Measurements on Tl-1212[12], and LSCO-214[13] polycrystalline samples also reveal a maximum in the low-temperature superfluid density near critical doping.

Many experiments are also consistent with the preformed pair model. Evidence for phase fluctuations significantly above the transition temperature are present in measurements of

the Nernst effect[14] and terahertz ac conductivity[15]. In addition, a recent analysis of thermal expansion data indicates phase fluctuations are present in optimally-doped, but not over-doped samples[16].

1.2 Superfluid Density

Closely tied to both of these scenarios is the superfluid density as a function of temperature and hole doping, $\rho(T, p)$. The superfluid density, defined in equations (1.13) and (1.14), is primarily reduced by quasiparticle excitations[17] at low temperatures and classical phase fluctuations[18] near the transition temperature. Early arguments in support of the preformed-pair model argued that the linear dependence of the low-temperature superfluid density was due to classical phase fluctuations[19]. Subsequent theoretical work showed that phase fluctuations will instead give a T^2 dependence to the superfluid density in the limit of zero temperature[20].

In a preformed-pair model, T_C is reduced significantly by phase fluctuations in the underdoped cuprates, in contrast to the overdoped cuprates. In Figure 2 the phase diagram is shown with 1) $T_{\phi,}$ the onset temperature of strong phase fluctuations 2) T_C the temperature at which long-range phase coherence is lost and 3) T_{MF} , the temperature of mean-field pairing. Although T* may represent the onset of local pairing, such as the formation of stripes, T_{MF} identifies where stripes may couple through the Josephson effect[5]. Phase fluctuations, present up to T_{MF}, where $T_C<T_{MF}<T^*$ are consistent with high frequency conductivity measurements[15]. Figure 2 shows that the range of phase

fluctuations $T_{MF} - T_\phi$ is larger on the underdoped side of the phase diagram, as implied by the preformed pair model.

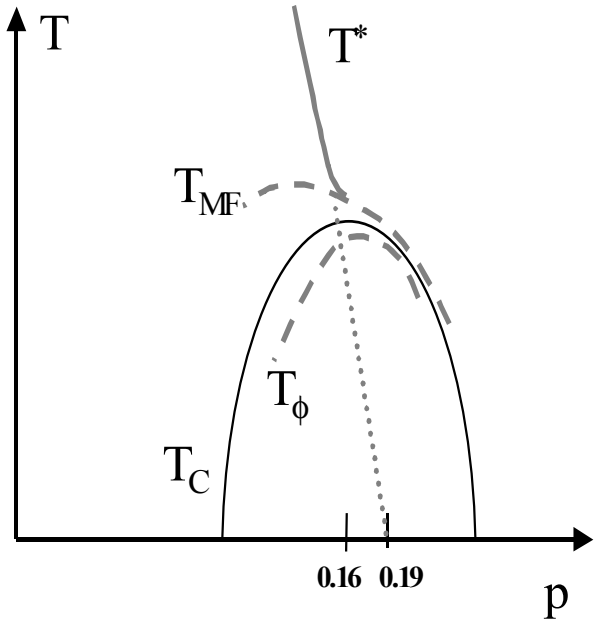

Figure 2: High-temperature superconductor phase diagram near T_C with the temperature at which phase fluctuations set in T_ϕ, and the mean-field transition temperature T_{MF}. The number of holes per Cu is p. Optimal and critically doped states are at p=0.16 and p=0.19, respectively.

In the second order-parameter model, the superfluid density changes below critical doping due to the onset of the pseudogap. In this scenario T* crosses the superconducting phase and reaches T=0 at critical doping, represented by a dotted line in Figure 2. In this model the loss of zero-temperature superfluid density with decreasing doping is associated with a competing order parameter. Another possible prediction of this model is a feature at intermediate temperature as the superfluid density crosses the T* line, $\rho(T) = \rho(T^*)$. For example, if the T* line is the transition line for a second

order parameter that competes with the superconducting state, the superfluid density might change slope as the superconductor is cooled through T*. In the d-density wave model, the superfluid density is predicted to crossover to a slower, $\sqrt{T}$, reduction in superfluid density for the extremely underdoped cuprates, although phase fluctuations are expected to modify this mean-field prediction[21]. A recent observation of two distinct gaps in the tunneling spectra (i.e. a pseudogap and a superconducting gap) supports the second order-parameter model[22].

1.3 Classic Models of Superconductivity

The London Equations

Since high-temperature superconductors have a short coherence length, the local limit applies and London's equation describes the supercurrent flow far below the transition temperature. London's first equation stated that the time derivative of the supercurrent $\vec{J}_s$ is proportional to the electric field

$$\frac{\partial \vec{J}_s}{\partial t} = \frac{n_s e^2}{m} \vec{E} . \tag{1.1}$$

The superconducting electrons n_s, electron charge e, and electron (effective) mass m describe the acceleration of electrons. The penetration depth λ followed from London's second equation and allowed one to rewrite equation (1.1) as

$$\frac{\partial \vec{J}_s}{\partial t} = \frac{1}{\mu_0 \lambda^2} \vec{E} . \tag{1.2}$$

Note that the penetration depth is not dependent on the pairing of electrons. In a superconductor λ^{-2} and n_s / m, are reduced by the quasiparticle excitations close to T=0. In a high-temperature superconductor electron pairing exists even as λ^{-2} reaches zero at T_C due to phase fluctuations, as discussed in sections (1.4) and (1.5). If the fields depend on time ($e^{i\omega t}$) and the scalar potential is zero ($\vec{E} = -\partial\vec{A}/\partial t$), we can rewrite equation (1.2) as

$$\vec{J}_s = -\frac{1}{\mu_0 \lambda^2}\vec{A} \tag{1.3}$$

in terms of the vector potential $\vec{A}$. In addition, Ohm's law can be written in terms of the complex conductivity $\sigma = \sigma_1 - i\sigma_2$ as

$$\vec{J} = -i\omega\sigma\vec{A}. \tag{1.4}$$

Since at low magnetic fields the imaginary conductivity, σ_2, is caused by the supercurrent,

$$\sigma_2\omega = \frac{1}{\mu_0\lambda^2} = \frac{n_s e^2}{m}. \tag{1.5}$$

The Ginzburg-Landau Theory

In Ginzburg-Landau theory, the order parameter $\psi(\vec{r}) = |\psi(\vec{r})|e^{i\phi(\vec{r})}$ defines the local phase and amplitude of the order. For an isotropic superconductor in zero applied field, the free energy density is

$$f = \frac{\hbar^2}{2m^*}\left|\left(\nabla - \frac{i2e}{\hbar}\vec{A}(\vec{r})\right)\psi(\vec{r})\right|^2 + \alpha(T)|\psi(\vec{r})|^2 + \frac{\beta}{2}|\psi(\vec{r})|^4 + \frac{1}{2\mu_0}\left(\nabla\times\vec{A}\right)^2, \tag{1.6}$$

where the pair mass is $m^*=2m$ and β is a positive constant. The parameter α is proportional to $T-T_c$. The Ginzburg-Landau correlation length is $\xi = \hbar / \sqrt{2m^*|\alpha|}$. Below the transition temperature the mean-field density of pairs is $n_s/2 = |\psi|^2 = |\alpha|/\beta = m^*/(4\mu_0 e^2 \lambda^2)$.

Anisotropy in this model is produced by an anisotropic effective mass. In a high-temperature superconductor, the c-axis effective mass of an electron m_c is different from the a- or b-axis effective mass m_{ab}. As a result, the anisotropy in the penetration depth, $\lambda_{ab} \neq \lambda_c$, and coherence length $\xi_{ab} \neq \xi_c$ can be described by the anisotropy parameter

$$\gamma \equiv \left(\frac{m_c}{m_{ab}} \right)^{1/2} = \frac{\lambda_c}{\lambda_{ab}} = \frac{\xi_{ab}}{\xi_c}, \tag{1.7}$$

and equation (1.3) becomes

$$J_i = -\frac{1}{\mu_0 \lambda_i^2} A_i . \tag{1.8}$$

Fisher, Fisher, and Huse have written the long-wavelength form of the free energy density as

$$f = \frac{1}{2} k_B \left[\nabla\phi - \frac{2\pi \vec{A}}{\Phi_0} \right] \vec{\rho}_s \left[\nabla\phi - \frac{2\pi \vec{A}}{\Phi_0} \right] + \frac{1}{2\mu_0} \left(\nabla \times \vec{A} \right)^2, \tag{1.9}$$

where the superfluid density tensor $\vec{\rho}_s$ is diagonal with components

$$(\rho_s)_{ii} = \rho_{s,i} = \frac{\Phi_0^2}{4\pi^2 k_B \mu_0 \lambda_i^2} \text{ [K/m]}^{18}. \tag{1.10}$$

Equation (1.9) is closely related to the free energy in a d-Dimensional XY model[23],

$$F = \frac{1}{2} k_B \int d^d x \rho_d \left[\nabla \phi(x) \right]^2 , \tag{1.11}$$

where ρ_d is called the spin-wave stiffness in magnetic systems and the superfluid density in superfluid systems. From equation (1.5) we can rewrite equation (1.10) as $\rho_{s,i} = \frac{\hbar^2 n_s}{4 k_B m_i}$, where m_i is the effective mass of an electron and n_s is the effective density of paired electrons.

For the anisotropic G-L model to be applicable, the c-axis correlation length must be comparable to the layer spacing $\xi_c \geq d$. Since $\xi_c \ll d$ at T=0 in HTS, and $\xi_c(T) \approx \xi_c(0)(1 - T/T_C)^{-1/2}$ in G-L theory, an estimate of the crossover temperature T_{2D-3D} from 2D to 3D behavior can be made[24]. The anisotropy is estimated as $\gamma \approx 7$ and $\gamma \approx 150$ for YBCO and BSCCO respectively[25]. In YBCO the crossover is predicted to occur at $T_{2D-3D} \sim 0.84 T_C$, which is in agreement with magnetization measurements. A similar treatment of BSCCO gives $T_{2D-3D} \sim 0.999 T_C$. Since critical (rather than mean-field) fluctuations describe superconducting transition temperature over at least a few degrees K in HTS, the mean field fluctuations are 3D (2D) as we approach the critical fluctuations in YBCO (BSCCO).

Fluctuations observed in conventional superconductors[26] are described in a mean-field model and may describe fluctuations outside of the XY critical regime discussed in the next section. The crossover to mean field fluctuations is called the "Ginzburg criterion". One estimate for the onset of mean-field fluctuations below T_c is calculated by setting the

ordering free energy in a correlation volume equal to the thermal energy[18]:

$\alpha^2 \xi_{ab}{}^2 \xi_c / (2\beta) \simeq k_B T$. Rewriting this criteria in mean-field theory with the definition of the superfluid density given in equation (1.10), gives

$$\rho_{s,ab} \xi_c \simeq c_s T \,, \tag{1.12}$$

where c_s is 4 and $\xi_c = \xi_{ab}/\gamma$. In the 3D-XY fluctuation model described below, $c_s \simeq 0.5$ is a universal constant, which implies that mean-field fluctuations exist at a lower temperature than XY critical fluctuations.

To fully describe our data in terms of critical fluctuations discussed in the next section, we use a generalized superfluid density

$$\rho \equiv \frac{\Phi_0^2 i\sigma\omega d}{4\pi^2 k_B} \text{ [K]}, \tag{1.13}$$

where d is the thickness of a unit cell and σ is the in-plane complex conductivity described in equation (1.4). This is related to equation (1.10) by

$$\mathrm{Re}[\rho] = \rho_{s,ab}\, d = \frac{\Phi_0^2 d}{4\pi^2 k_B \mu_0 \lambda_{ab}^2}, \tag{1.14}$$

since our experiment measures the conductivity in the ab plane and $\rho = \rho_{s,ab}\, d$ at our measurement frequencies. Equation (1.14) can be rewritten as

$$\mathrm{Re}[\rho] = \frac{d}{\lambda^2} 6.24 \cdot 10^{-3} \,\mathrm{m \cdot K}\,. \tag{1.15}$$

In optimally doped $Bi_2Sr_2Ca_1Cu_2O_{8+\delta}$, $\mathrm{Re}[\rho(0)] \simeq 143$ K, since $\lambda_0 \simeq 2600\,\mathring{\mathrm{A}}$ and a unit cell thickness is $d = 15.4\,\mathring{\mathrm{A}}$.

1.4 Critical Fluctuation Theories

The Kosterlitz-Thouless-Berezinskii (KTB) Transition

The KTB transition[27] describes the critical fluctuations of a 2D superfluid sheet or a 2D-XY Model. In this model, the energy can be written in terms of the phases ϕ_i at each square lattice site by $H = -J\sum_{\langle i,j\rangle}\cos(\phi_i - \phi_j)$, where J is a positive constant. The KTB transition has been observed in superfluid helium films[28], superconducting arrays[29], thin conventional superconducting films[30], and superconducting wire networks[31].

The main feature predicted in a KTB transition is a universal drop in ρ at a temperature given by

$$\rho(T_{KTB}) = \tfrac{2}{\pi} T_{KTB}\,. \tag{1.16}$$

An intuitive justification of the KTB transition temperature can be given by considering the free energy of a system with one vortex. The energy of a adding a vortex to a 2D superfluid is

$$E_{1V} = \tfrac{1}{2} k_B \rho \int (\nabla\phi)^2 d^2\mathrm{r} = k_B \pi \rho n^2 \ln[L/\xi_0]\,, \tag{1.17}$$

where *n* is the number of flux quanta within the vortex, L is the system size, and ξ_0 is the size of a vortex core. The entropy of a film with a single vortex is the log of the number of vortex positions

$$S_{1V} = k_B \ln[(L/\xi_0)^2]. \tag{1.18}$$

The energy cost of adding a vortex diverges with the system size. However the free energy, $F_{1V} = E_{1V} - TS_{1V}$, is lowered by the vortex at

$$T = \frac{\pi n^2 \rho}{2}, \tag{1.19}$$

where n=1 dominates in equilibrium thermodynamics. Although a detailed description is more complex, at the same temperature a superfluid film will create free vortex-antivortex pairs to lower the free energy, as described by a KTB transition. A vortex-antivortex pair has a logarithmic interaction similar to equation (1.17), except the length L is changed to the distance between the vortex-antivortex pairs. The correlation length above T_{KTB} at which vortex-antivortex pairs unbind is

$$\xi_{KTB} \simeq \xi_0 e^{\left(\frac{b(T_{MF}-T_{KTB})}{T-T_{KTB}}\right)^{1/2}}, \tag{1.20}$$

where b is a constant of order unity[41].

Since superconductors are charged superfluids, finite size effects will eventually modify the transition. In a 2D-XY model, the logarithmic interaction between the vortices is modified beyond the 2D screening length $\lambda_\perp = \lambda^2 / d$, which is equal to 0.98 cm/T_C (K) at the transition temperature[32]. In high-temperature superconductors the adjacent planes cause the interaction of vortices to grow linearly beyond a characteristic Josephson screening length [41], which is important in the Coupled Layer Model (CLM) described below.

Models for the dynamics in a 2D-XY system are theoretically described by the diffusion of vortices[33,34]. Since vortices renormalize the superfluid density and a larger

measurement frequency will allow less time for vortices to diffuse in a cycle, higher frequencies effectively measure shorter distances. According to the dynamic model, at sufficiently high frequencies, the superfluid density is not renormalized by phase fluctuations and the bare superfluid density is measured.

Scaling Theory and the 3D-XY Transition

In 1991 critical fluctuation effects were observed[35] in bulk high-temperature superconductors and it was recognized that high-temperature superconductors exhibit 3D-XY critical fluctuations over an observable temperature range[18, 36, 37]. Fisher, Fisher and Huse wrote scaling relations for the complex conductivity σ in the XY Model. The predictions are particularly powerful for the 3D-XY model (D=3). Since $\rho \sim \xi^{2-D}$, we write the general scaling function as

$$\rho = \xi^{2-D} S(\omega\xi^z, E\xi^{z+1}), \tag{1.21}$$

where ξ, ω, and z are the correlation length, frequency, and dynamic critical exponent, respectively. The time scale of the fluctuations is $\tau \sim \xi^z$, where z is described in the classification scheme of Hohenberg and Halperin[38]. In 3D, model E dynamics describes a propagating mode and z=1.5, whereas model A dynamics describes diffusive behavior (z=2). The correlation length depends on the temperature with a functional form

$$\xi \sim \left|T - T_C\right|^{-\nu}, \tag{1.22}$$

where the static critical exponent $\nu \approx 2/3$ for D=3.

In the limit that ρ is frequency and field independent in a 3D system, equations (1.21) and (1.22) give the superfluid density as $\rho \sim |T - T_C|^{2/3}$. In contrast, Ginzburg-Landau mean-field theory gives $\rho \sim |T - T_C|$, and $\xi \sim |T - T_C|^{-1/2}$.

When the response is field independent, equation (1.21), gives the phase angle scaling relation

$$\phi_\rho = P(\omega\xi^z), \tag{1.23}$$

where $\omega\xi^z$ diverges at T_C. At this critical temperature, the phase of the superfluid density takes a frequency independent value equal to

$$\phi_c = \tfrac{\pi}{2}\tfrac{D-2}{z} \tag{1.24}$$

and the magnitude of the superfluid density varies as

$$|\rho| \sim \omega^{\frac{D-2}{z}}. \tag{1.25}$$

When the ρ depends on the frequency and the applied field, the scaling relationship at T_C is

$$\rho = \omega^{(D-2)/z} S(\omega E^{-z/(z+1)}). \tag{1.26}$$

1.5 Models of the Superconducting Transition

There are two types of models used to describe the zero-field phase transition in high-temperature superconductors. One model directly applies the 3D-XY theory, which is

predicted to apply even for large anisotropies[39]. The second model assumes the layers of the superconductor are weakly coupled and the KTB correlation length accounts for the crossover temperatures. This model is intended to describe the delayed unbinding of vortex-antivortex pairs due to the adjacent layers. At present, simulations show a complex relationship between 2D and 3D behaviors[40,41] and are inadequate to predict a model of the transition.

3D-XY

An estimate for the 3D regime in terms of the 3D-XY model gives a good description of the critical regime in YBCO. Analogous to the vortex-antivortex pairs in a 2D-XY transition, the 3D-XY transition is associated with vortex loops. The range of the critical fluctuations can be estimated from theory[42]. The c-axis correlation length is predicted to be related to the in-plane penetration length by

$$\xi_c \simeq c_s \pi \lambda_{ab}^2 / \Lambda_{T_C} , \tag{1.27}$$

where the thermal length is

$$\Lambda_T \equiv \frac{\Phi_0^2}{4\pi\mu_0 k_B T} \simeq \frac{2\times 10^8}{T} \text{ K Å} , \tag{1.28}$$

and $c_s \approx 0.5$ is a universal constant. From equations (1.14), (1.27), and (1.28) we see that

$$\rho = c_s d\, T_C / \xi_c . \tag{1.29}$$

This implies that when $\xi_c = d$, the superfluid density identifies the crossover $T_{cr}{}^{3D}$ into 3D-XY fluctuations as the c-axis correlation length exceeds the layer

spacing $\rho(T_{cr}^{3D}) = c_s T_c$. In addition, films can have an additional crossover T_{cr}^{2D} as the c-axis correlation length exceeds the thickness of the film. If the film is sufficiently thin, the c-axis correlation length can exceed the film thickness so that the three-dimensional to two-dimensional crossover is observed just below T_C. Below the crossover, the film should behave similar to a YBCO crystal; above the crossover the film may exhibit a drop in the superfluid density similar to a KTB transition. From equation (1.29), we can see that ξ_c is equal to the thickness of *n* layers when

$$\rho(T_{cr}^{2D}) = \frac{c_s}{n} T_c, \tag{1.30}$$

which is approximate if ρ is frequency dependent. The film will appear quasi-2D when the c-axis correlation length is smaller than the layer spacing ($\rho \geq 0.5 T_c$) or larger than the film thickness ($\rho \leq \frac{0.5}{n} T_c$) in the static limit. For comparison, a KTB model predicts a transition at $\rho = \frac{2}{\pi} T_C$ for an isolated layer and $\rho = \frac{2}{\pi n} T_C$ for a coherent film (assuming $d << \lambda$).

Coupled Layer Model

Glazman and Koshelev proposed a coupled layer model to describe the transition in Bi and Tl based cuprate superconductors. They recognized that the 2D-3D crossover in these cuprates occur at a temperatures higher than the onset of phase fluctuations[41, 43]. In this model, the characteristic temperatures are determined using the correlation length given by KTB theory and the Josephson coupling between the planes.

Figure 3 shows the characteristic temperatures near the transition temperature, as proposed by Glazman *et al*. The mean field transition temperature, T_{MF}, is the transition temperature in the absence of phase fluctuations. Close to the transition temperature T_C, 3D fluctuations are present. As the sample is cooled, the 3D fluctuations crossover to 2D fluctuations at T_{3D}^f. At temperatures around the transition temperature for a 2D system, T_{KTB}, 2D fluctuations occur. Strong 2D fluctuations vanish at a temperature T_{2D}^f.

The phase transition (T_C) does not occur at T_{KTB} because the vortex-antivortex pairs are bound by a linear potential at distances larger than the Josephson screening length, $\Lambda = \gamma d$. Once the KTB correlation length reaches the Josephson screening length, the vortex-antivortex pairs can unbind at short length scales, and induce the 3D phase transition.

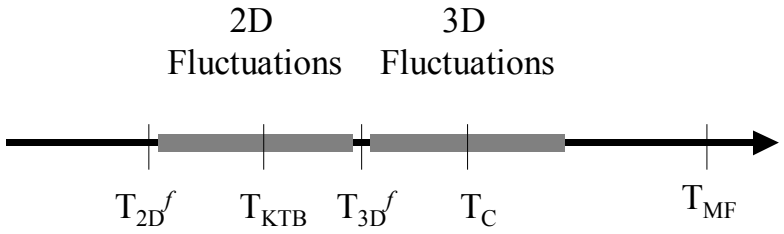

Figure 3: Characteristic temperatures in BSCCO in the coupled layer model. In a temperature range around the transition temperature, T_C, 3D fluctuations are present. In a temperature range around the KTB temperature, T_{KTB}, strong 2D fluctuations are present.

From Equation (1.20), one can estimate the transition temperature as

$$T_C = T_{KTB} + \frac{b(T_{MF} - T_{KTB})}{(\ln[\gamma d / \xi_0])^2} \tag{1.31}$$

At low-temperatures the correlation length is much smaller than the interlayer spacing. An estimate of the onset of strong 2D fluctuations[41] is given by

$$T_{2D}^{f} \simeq T_{MF} - \tfrac{1}{2}(T_{MF} - T_{KTB}) \ln[\gamma d / \xi_0]. \tag{1.32}$$

Using values of $\gamma = 150$, d=15.4 Å, and $\xi_0 = 25$ Å in equations (1.31) and (1.32) give the relationships

$$T_C \simeq T_{KTB} + (T_{MF} - T_{KTB}) b / 20 \tag{1.33}$$

and

$$T_{2D}^{f} \simeq T_{MF} - 2.3 \times (T_{MF} - T_{KTB}). \tag{1.34}$$

Unfortunately, equations (1.33) and (1.34) are difficult to verify, since b is unknown and T_{2D}^{f} is a crossover temperature. This model is similar to the 3D-XY model in that they both predict 3D phase fluctuations around T_c. However, in the 3D-XY model the characteristic temperatures are directly predicted from the 3D-XY correlation length.

2 Experimental Technique

The two-coil inductive technique is a sensitive probe of the penetration depth in superconducting films. In this technique the mutual inductance is measured between two coils, typically on opposite sides of a film. The screening currents induced in the film strongly reduce the measured mutual inductance from which the penetration depth is calculated.

2.1 Introduction

The two-coil inductive technique has been implemented in various experiments to measure the penetration depth. The technique was first demonstated in a superconducting film by Fiory *et al*. in 1980[44]. The low temperature penetration depth in high-temperature superconductors has been studied in $Y_1Ba_2Cu_3O_7$[45], $La_{2-x}Sr_xCuO_4$[46], and $Nd_{1.85}Ce_{0.15}CuO_4$[47] films. Near the transition temperature, YBCO [48, 49, 50], Al/Al-Oxide [44], In/In-Oxide[51], and MoGe Films[52], as well as superconducting wire networks[31], and both conventional[53] and high-T_C[54] proximity systems have been studied with this technique.

The two-coil inductive technique has many advantages over other techniques to measure the superfluid density of a film. Parallel resonators are very sensitive to $\Delta\lambda$, however the value of λ is not measured[55,79]. Other resonator techniques, such as a coplanar stripline[56], require patterning which precludes other measurements. Terahertz

spectroscopy measures the complex conductivity of films, but measures the phase stiffness over short length scales and therefore should be considered a complementary probe to our measurements[57]. Terahertz spectroscopy cannot be performed on most of the films we have measured due to the optical properties of the $SrTiO_3$ substrate[58].

Near the transition temperature, the sample has a finite real component of conductivity (imaginary part of ρ). The purpose of the experiment is to extract the complex conductivity as a function of temperature. In the next section, the experimental setup to measure the mutual inductance is described. Then the programs used to determine the complex conductivity from the data are discussed. The final section summarizes the theories of the mutual inductance as a function of complex conductivity $M(\hat{\sigma})$.

2.2 Experimental Design

The circuit for the measurements is shown in Figure 4. Current from a home-built source at known frequency and amplitude is sent through the drive coil. A second coil on the opposite side of the film measures a voltage related to the drive current by the mutual inductance and frequency $M = V/(i\omega I)$. A Stanford Research lock-in amplifier with a phase reference from the current source, measures the voltage across the receive coil with $10M\Omega$ input impedance. Typical measurement frequencies are 10 – 100 kHz.

The sample and coils are cooled by He^4 gas in a flow-through dewar. The temperature of the incoming gas is controlled at the bottom of the dewar and the sample temperature is

monitored by a Si diode attached to the substrate. Labview programs control settings and receive data from the lock-ins and temperature controller. In a typical experimental run, the temperature is continuously ramped, while the magnitude and phase of the mutual inductance is recorded.

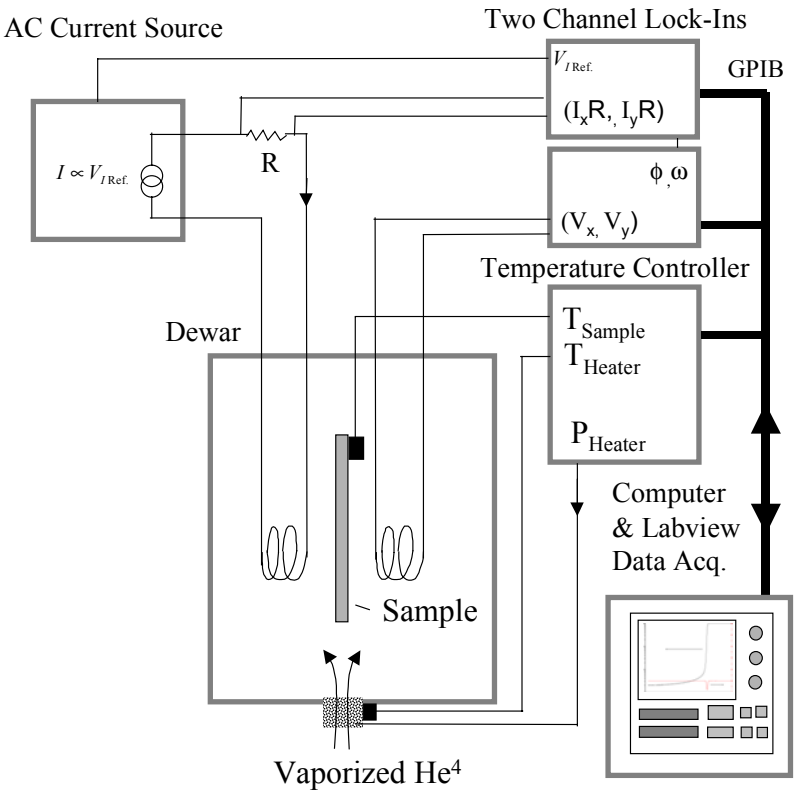

Figure 4: Two-coil inductive measurement system. In the dewar, the sample temperature is controlled by the continuous flow of He^4 gas. The two coils used to measure the mutual inductance are on opposite sides of the film.

A second lock-in is used to improve the analysis in two different implementations. The second lock-in can be used to measure a second frequency simultaneously. In this case, the second measurement gives an important check on the system and the film, since the

mutual inductance away from the transition should be independent of the frequency. In our measurements, there is less than a 1% difference in the low temperature mutual inductance over our frequency range. The second lock-in can also measure the phase and amplitude of the drive current, which is used to measure errors in the phase and amplitude of the current source. The applied current varies less than 0.5% from the nominal current over the frequency range from 10 kHz to 100 kHz. Our measurement frequency and RMS current amplitude is 80 kHz and 40 μA, unless specified otherwise. To maximize the performance of our measurement, the drive coil is placed on the film side of the substrate with a thin-film resistor inserted in series to stabilize the impedance of the circuit. The receive coil is placed on the opposite side of the substrate. This arrangement minimizes the leakage of flux around the edges of the film.

The coils are flat, similar to those used by Claussen[53], with an average radius of 1.5mm and a thickness of 0.2 mm. The coil posts are machined from Vespel with a thin wall of Vespel at the end of the post to allow the coil to be placed close to a film. The coils are slowly wound with copper wire on a coil-winder and typically have 120 turns. Measurements of the coil forms are taken with a microscope before and after the coil is wound to precisely determine the dimensions used in calculating the penetration depth. The resistance of a coil is approximately 3 ohms and the self inductance is approximately 10μH. The mutual inductance and distance between the coils is approximately 1.5 μH and 1.6 mm, respectively, for a film on a 1 mm thick substrate.

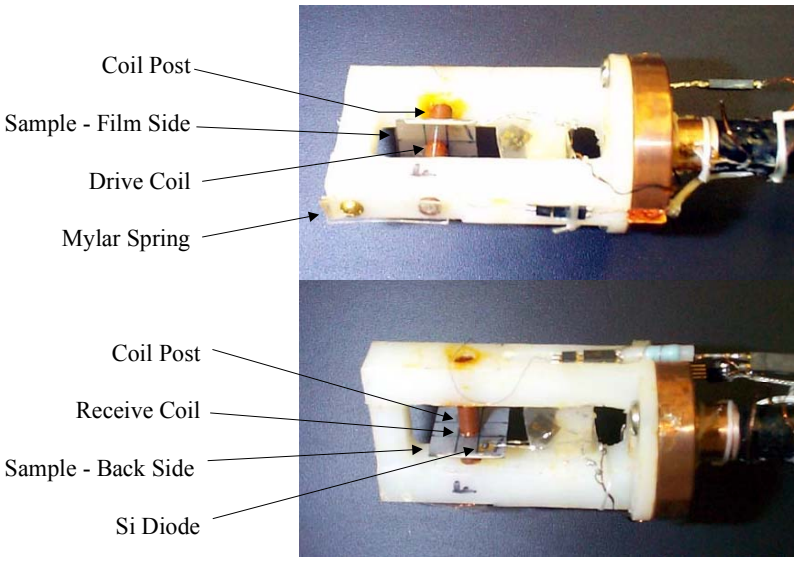

Figure 5: Two-Coil Inductive Insert. Film is held in place between the drive and receive coil by a Mylar spring.

The samples are coated with PMMA resist and a 0.1mm thick coverslip is placed on top of the resist during measurement to protect the surface from scratches. The film is mounted between the coil posts using rubber cement for friction. To keep the sample in place the posts press against the film with the force exerted by a mylar spring at the opposite end of one of the coil posts. The variation in the mutual inductance from thermal expansion is approximately 1% from 4.2 to 300 Kelvin, which allows sensitive measurements close to T_C.

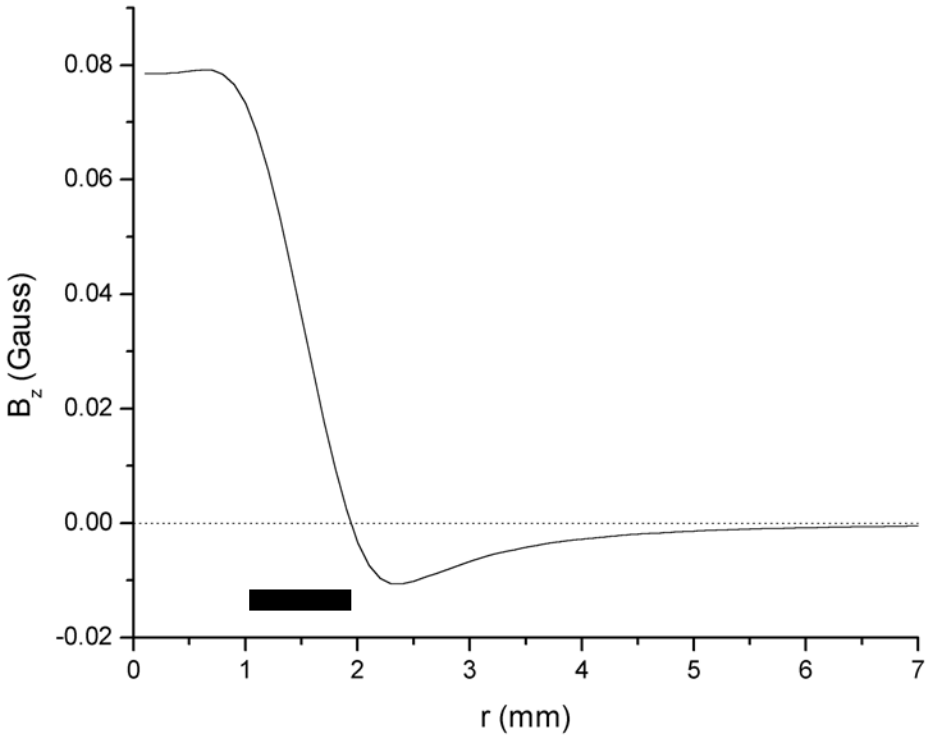

Figure 6: Amplitude of ac magnetic field in z direction applied to film as a function of radial position for I=40 μA. The radius of the drive coil turns is represented by a rectangle that is between 1 and 2 mm along the film radius.

In Figure 6 the radial dependence of the RMS z component of the magnetic field applied to the film is shown with a drive current amplitude of 40 μA. As the temperature is lowered below T_C the total field at the film will be much smaller due to the screening currents in the film. The coil is placed 0.35 mm from the film. At the mean radius of the coil, 1.5 mm, the z component of the field drops rapidly. The coil turns have a radius between 1 and 2 mm, which is partially responsible for the strong variation in field at those lengths in Figure 6. The lower critical field, H_{C1}, is 690 Gauss and 120 Gauss for fields along the c and a-b axis respectively, in YBCO[59]. In BSCCO, the critical field is

100 Gauss along the c-axis and 2 Gauss along a-b axis[60]. Our ac measurement fields are generally much smaller than H_{c1}.

2.3 Data Analysis Programs

The numerical inversion allows us to obtain the complex conductivity as a function of the measured mutual inductance $\hat{\sigma}(M)$, from a known formula for $M(\hat{\sigma})$. As will be discussed above, $\rho \sim i\omega\sigma$, and therefore the inversion program also finds $\rho(M)$. An example of raw and inverted data is shown in Figure 7. In the upper two panels the measured in-phase and out-of phase mutual inductance is shown. Note that the mutual inductance drops nearly 3 orders of magnitude due to the screening of the film. After the inversion, real and imaginary components of the superfluid density are obtained, as shown in the bottom panel.

To obtain the complex conductivity (or ρ), the raw mutual inductance data is used in two Mathematica programs. The first program calculates the separation between the two coils from the mutual inductance above the transition temperature. The second program calculates the mutual inductance for a set of complex conductivities and then numerically finds the complex conductivity for the raw mutual inductance data.

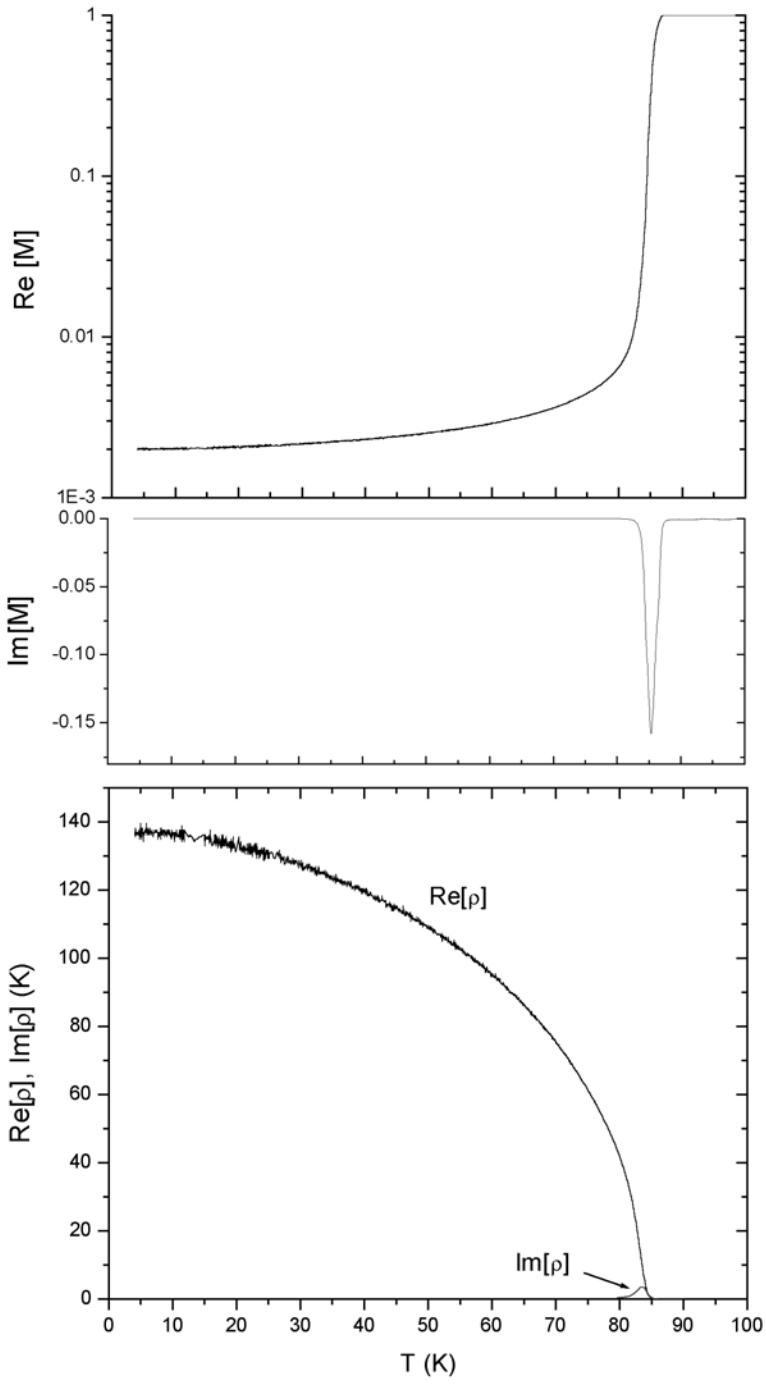

Figure 7: Upper two panels: normalized mutual inductance components Re[M] and Im[M]. Bottom panel: calculated Re[ρ] and Im[ρ] versus temperature.

To calculate the mutual inductance for the coils, the coil sum in equation (2.1) is replaced by an integral over the coil cross-section. A mutual inductance formula for the rectangular cross section coil is used that requires only one numerical integration, which facilitates an accurate calculation. In the first program, the coil separation is numerically found by adjusting the coil separation until the calculated mutual inductance is equal to the measured mutual inductance.

The program that inverts the data is more complex. The real and imaginary parts of the mutual inductance are calculated for a grid of real and imaginary conductivities. The raw data are imported and the finite-film diameter correction of equation (2.13) is applied. Finally, a minimization routine is implemented to find the best fit for the complex conductivity from the complex mutual inductance data points.

To improve the numerical inversion, a function of the mutual inductance $g = m^{-1} - 1$ is used for the numerical inversion, where m is the normalized mutual inductance. The function g is easier to approximate than m, because g is approximately linear in the conductivity, as seen from equation (2.8)[30]. Since the mutual inductance is complex, a grid of complex conductivity values defines a surface for the real and imaginary parts of *g*. The surfaces for *g* are computed for a set of complex conductivities. Next g is calculated for the raw data. Finally, a minimization routine finds the best match for the *g* to find σ. A logarithmic scale used in the program allows precise inversion of the conductivity over several decades.

A new mutual inductance calculation is made for each experiment, since every experiment has a unique film thickness and coil separation. A self consistency check confirms the reliability of the program. The computation time for all calculations is less than 2 hours in Mathematica running on a 400 MHz PC.

2.4 Mutual Inductance Theory

There are various expressions for the mutual inductance between two-coils on opposite sides of a conducting film. First we will present a general expression, for a finite-thickness infinite-diameter film. Even though the general expression is used for the data analysis, various intuitive limits follow to relate the raw data to the extracted data. Next formulas that account for the finite film diameter are discussed. Finally, an expression for a film with edges screened by a superconducting tube is presented, which may be useful in future experiments and serves as a comparison to the standard technique.

The mutual inductance between two coils with a film placed between them can be expressed exactly in certain limits. The field from the drive coil induces currents in the film with a complex conductivity $\sigma = \sigma_1 - i\sigma_2$. The currents in the film lower the mutual inductance between the coils. The complex conductivity defines a complex screening length $\lambda_\omega = (i\mu_0\omega\sigma)^{-1/2}$, which is equal to the penetration depth λ when σ_1 is zero ($\sigma = -i\sigma_2$).

In the measurements presented, the frequency is sufficiently low that the complex conductivity σ of the superconducting film at low temperatures only measures the imaginary conductivity, which corresponds to the screening due to the superfluid ($\sigma = -i\sigma_2$). In general, a finite σ_1 can be caused by a quasiparticle current as seen in microwave measurements; at our experimental frequencies σ_1 is only measurable near the superconducting phase transition.

General Expression: Infinite-Diameter Film

The fields for a drive coil above a finite-thickness conducting film was first derived by Dodd and Deeds[61]. The theory was extended by Clem and Coffey to allow the mutual inductance to be calculated in superconducting films with vortices[62]. This formula is a general analytical expression that is used to extract the complex conductivity from our the mutual inductance data. Recently Coffey has calculated the mutual inductance for a film with a permeability $\mu \neq \mu_0$, which is relevant for superconductors with antiferromagnetic ordering[63].

The general expression for the mutual inductance is

$$M_{\text{infinite}} = \mu_0 \pi \sum_{i,j} r_i r_j \int_0^\infty dq \mathrm{J}_1(qr_i)\mathrm{J}_1(qr_j) e^{-q(z_i - z_j)} f(q,Q,d), \tag{2.1}$$

where J_1 is a Bessel Function of the first type,

$$f(q,Q,d) = e^{qd}\left[\cosh(\mathrm{Q}d) + \tfrac{\mathrm{Q}^2+q^2}{2q\mathrm{Q}}\sinh(\mathrm{Q}d)\right]^{-1}, \tag{2.2}$$

and $Q^2 = q^2 + \lambda_\omega^{-2}$. The coordinates for the drive and receive coil turns are given by (r_i, z_i) and (r_j, z_j). If the conductance of the film is sufficiently small $(\sigma \to 0)$, $f \to 1$ and the bare mutual inductance between the coils,

$$M_0 = \mu_0 \pi \sum_{i,j} r_i r_j \int_0^\infty dq J_1(qr_i) J_1(qr_j) e^{-q(z_i - z_j)} \tag{2.3}$$

is obtained.

Approximations to the General Expression

If the screening length and film thickness are significantly smaller than the coil size l (i.e. $|\lambda_\omega|, d << r_C$, where $r_C \approx r_i \approx r_j \approx z_i - z_j$), we can approximate the mutual inductance as

$$M = \mu_0 \pi \sum_{i,j} r_i r_j \int_0^\infty dq J_1(qr_i) J_1(qr_j) e^{-q(z_i - z_j)} \left[1 + \tfrac{1}{2q\lambda_\omega} \sinh(d/\lambda_\omega)\right]^{-1}. \tag{2.4}$$

This expression has been used by Lemberger[64] and is similar to the expression used by Claussen[65].

Since the integral selects q^{-1} approximately equal to the coil size r_C, we can write the normalized mutual inductance as

$$m \equiv \frac{M}{M_0} \approx \frac{1}{1 + \frac{r_c}{2c\lambda} \sinh(d/\lambda)}, \tag{2.5}$$

where *c* is on the order of 1. To first order in d/λ,

$$m = c\frac{2\lambda^2}{dr_C}\left(1+\mathrm{O}\left(\left(\frac{d}{\lambda}\right)^2\right)\right). \tag{2.6}$$

Values of $c = 3\pi/8$ [66] and $c = 1$ [67] have been found for two different approximations. When the penetration depth is much smaller than d,

$$m \approx c\frac{(2\lambda)^2}{r_C}e^{-d/\lambda} \tag{2.7}$$

and the screening is exponentially attenuated by the film thickness.

Jeanneret[31] solved the mutual inductance for a thin film using Fourier transformations. In the calculation, the penetration depth is assumed to be much larger than the film thickness ($\lambda_\omega >> d$). The mutual inductance in this limit is

$$M = \mu_0\pi\sum_{i,j} r_i r_j \int_0^\infty dq \mathrm{J}_1(qr_i)\mathrm{J}_1(qr_j)e^{-q(z_i-z_j)}\left[1+\frac{d}{2q\lambda_\omega^2}\right]^{-1}. \tag{2.8}$$

Comparison with equation (2.4) reveals that equation (2.8) can be modified to take into account the decay of fields through the film thickness if the screening length λ_ω^2/d in equation (2.8) is replaced with the length $\lambda_\omega/\sinh(d/\lambda_\omega)$. This effective screening length is 4% smaller than the thin film value when $d = \lambda/2$. The effective screening length decreases exponentially as the thickness of the film is increased beyond the penetration depth.

Finite-Diameter Corrections

In practice, the screening is usually strong ($m \ll 1$) at low temperatures and significant error can result from using the general expression without a film-diameter correction. Unfortunately, no closed-form expression has been derived for the mutual inductance near a finite-diameter film[68,69]. Despite the absence of rigorous derivations, two expressions have been proposed that were found to agree with numerical simulations. The primary corrections for the finite-film diameter describe a leakage of field around the finite diameter film.

Hebard and Fiory found that the mutual inductance for a finite diameter film can be approximated by replacing f in equation (2.4) by

$$f' = f \bullet \left(1 - e^{-(q/q_C)^2}\right) + e^{-(q/q_C)^2}, \tag{2.9}$$

where $q_C = 2/\pi r_{\mathrm{f}}$ defines a cutoff for the film radius $\mathrm{r_f}$[70]. This implies that the mutual inductance varies as

$$m_{\text{finite, HF}} = m_{\text{infinite}} - m_{\text{Trans.}} + m_{\text{Leak}}, \tag{2.10}$$

where

$$m_{\text{Leak}} = M_0^{-1}\mu_0\pi\sum_{i,j} r_i r_j \int_0^{\infty} dq \mathrm{J}_1(qr_i)\mathrm{J}_1(qr_j)e^{-q(z_i - z_j)}e^{-(q/q_C)^2}, \tag{2.11}$$

approximates the leakage around the film and

$$m_{\text{Trans.}} = M_0^{-1}\mu_0\pi\sum_{i,j} r_i r_j \int_0^{\infty} dq \mathrm{J}_1(qr_i)\mathrm{J}_1(qr_j)e^{-q(z_i - z_j)}e^{-(q/q_C)^2} f(q,Q,d) \tag{2.12}$$

modifies the transmission through the film.

A second correction method was proposed by Turneaure *et al*., and justified with numerical calculations and data to correct for the low-temperature penetration depth. This method is used throughout this work to correct for the film diameter. The correction method asserts that 1) the mutual inductance with an infinite-diameter film m_{infinite} is related to the mutual inductance with a finite-diameter film m_{finite} by the subtraction of a constant representing the fields leaking around the film m_c [65, 71] and 2) the constant m_c is approximately equal to the normalized mutual inductance of a thick superconducting film with the same shape as the sample. With proper normalization, this formula becomes

$$m_{\text{infinite}} = \frac{m_{\text{finite}} - m_{\text{c}}}{1 - m_{\text{c}}}, \tag{2.13}$$

or

$$m_{\text{finite}} = m_{\text{infinite}}\left(1 - m_{\text{c}}\right) + m_{\text{c}}. \tag{2.14}$$

In order to analyze data m_{c} is measured. However, to simulate the mutual inductance for different film diameters, we substitute m_{Leak} calculated from equation (2.11) for m_c in equation (2.14). The calculated value m_{Leak} is larger than m_c measured for our coils, and therefore the simulation overestimates the correction.

In the simulation we use $h = r_{\text{i}} = r_{\text{j}} = z_i - z_j = 1.8\text{mm}$, $d = 600\text{Å}$, $\lambda \geq 1800\text{Å}$, and $x \equiv \lambda^2/(d\,h) \geq 3\cdot 10^{-4}$. If the radius of the coil is set to 10 mm, the fractional difference between the finite-film expressions (with m_{c}=m_{Leak}) in equation (2.14) and (2.10),

$$\triangle m = \left| \frac{m_{\text{finite}} - m_{\text{finite, HF}}}{m_{\text{finite, HF}}} \right| \tag{2.15}$$

is less than 0.4% for all x. The difference between the finite-thickness expression, equation (2.1), and thin-film expression, equation (2.8), are negligible for this analysis.

The mutual inductance for films with diameters of 10, 12, 14 and 20 mm are shown in Figure 8. At small penetration depths, more than half of the mutual inductance is "leaking around" the film. In this case, the accuracy is limited by the ability to estimate the diameter of the film. At large penetration depths, the mutual inductance is insensitive to the film diameter. It should also be noted that the mutual inductance is not proportional to $\lambda^2/(d\,h)$ for finite film diameters.

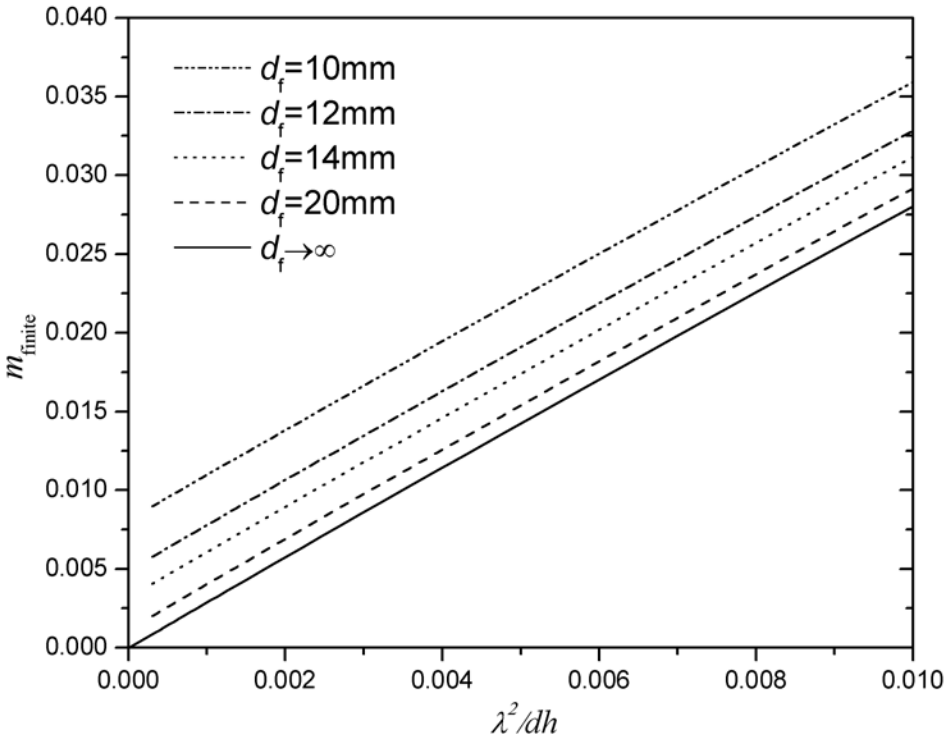

Figure 8: Simulation of normalized mutual inductance as a function of λ^2/dh for different film diameters in standard measurement.

In practice, m_c is measured and the uncertainty in λ can be controlled by measuring sufficiently thin films. When the film screens strongly, equations (2.6) and (2.13) give the uncertainty in λ as

$$\frac{\left|\Delta(m_{finite} - m_c)\right|}{m_{finite} - m_c} = 2\frac{\left|\Delta\lambda\right|}{\lambda} = \frac{\left|\Delta\rho\right|}{\rho}. \tag{2.16}$$

To keep the relative uncertainty in ρ sufficiently low, thin films are chosen such than $m_{finite} > 3m_c$. In our experiments the accuracy of the low-temperature penetration depth is limited by this correction.

Expression with Cylindrical Shield

From the above simulation on a finite film, it is apparent that the power law and the value of the low temperature penetration depth obtained from this technique depends on the finite diameter film correction. To eliminate the error introduced by leakage around the film a new geometry is proposed, which screens the edges of the film and is described by an analytical solution. Since the shield must be superconducting it should be easily implemented for testing low-temperature superconducting films, which can be used in future implementations of the two-coil mutual inductance technique.

The proposed modification of the standard two-coil technique involves shielding the edges of the film with a superconducting cylindrical tube. This geometry has advantages over the conventional method because the measurement is insensitive to the diameter of

the tube and the measurement depends only on the properties in the bulk (center) of the sample (film), since the shield screens out fields at the edges.

From a derivation in Appendix A, the mutual inductance in the presence of a cylindrical shield is

$$M_{shield} = \frac{2\pi\mu_0}{r_s^2}\sum_{r_i,r_j} r_i r_j \sum_n \frac{J_1(\alpha_n r_i) J_1(\alpha_n r_j)}{\alpha_n \left[J_2(\alpha_n r_s)\right]^2} \frac{e^{-\alpha_n |z_i - z_j|}}{1 + \frac{d}{2\alpha_n \lambda_\omega^2}}, \tag{2.17}$$

where r_s is the radius of the shield and $J_1(\alpha_n r_s) = 0$. The normalized mutual inductance is

$$m_{shield} = \frac{M_{shield}(\lambda_\omega)}{M_{shield}(\lambda_\omega \to \infty)}. \tag{2.18}$$

A plot of the normalized mutual inductance is shown in Figure 9. This technique has two advantages over the standard technique: 1) the slope of the penetration depth from the film diameter is less sensitive to the film diameter and 2) the mutual inductance remains proportional to λ^2 for strongly screening films (see equation (2.6)). A superconducting shield could easily be made with Pb foil for future tests of the penetration depth for superconductors with low transition temperatures.

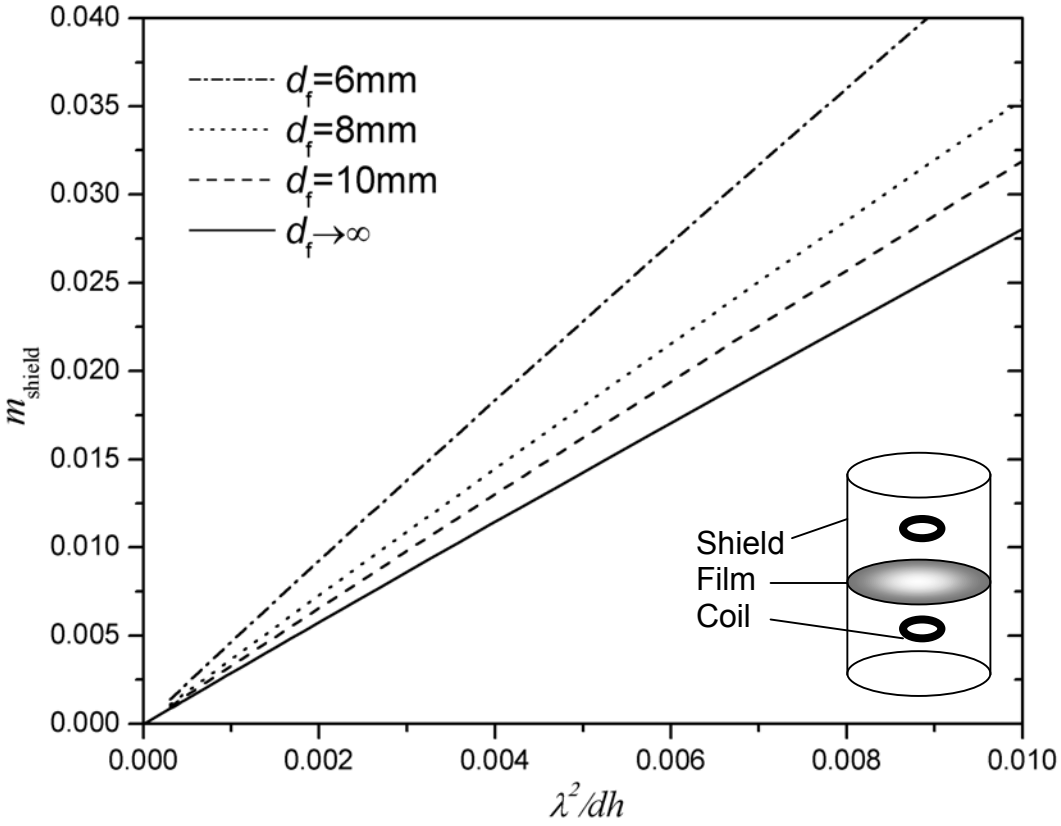

Figure 9: Normalized mutual inductance as a function of λ^2/dh for different film diameters with a cylindrical shield.

3 Superconducting Transition in YBCO Films

The penetration depth in YBCO has been widely studied. We present evidence that the superfluid density in YBCO films is consistent with the 3D-XY static transition observed in YBCO crystals[42,75], but not with other reports on YBCO films. An analysis of the film diameter correction indicates that the observed range of critical fluctuations is modified by the correction.

3.1 Previous Measurements on YBCO

The in-plane penetration depth in YBCO has been measured by many techniques and the functional form is understood near zero temperature and close to the critical temperature. The superconducting order parameter of high-temperature superconductors is d_{x2-y2}, and due to the nodes the density of quasiparticle excitations is linear in temperature. This is seen in microwave[72], muon-spin relaxation[73], and ac-susceptibility[74] measurements as a linear temperature dependence of the penetration depth at low temperatures. Near the transition temperature, a 3D-XY critical exponent is observed in the functional form of the superfluid density in microwave measurements on single YBCO crystals[42,75].

Low temperature measurements on laser-ablated YBCO films generally show a T^2 temperature dependence at low temperatures that is likely due to impurity scattering. In this respect our low-temperature measurements on laser-ablated YBCO are in agreement

with other measurements. We will discuss the low-temperature behavior on epitaxially grown BSCCO films in the next chapter.

Studies on YBCO films disagree with comparable studies on YBCO crystals concerning the observation of the static critical fluctuations. Studies of the superfluid density in YBCO crystals indicate a critical fluctuation regime as large as 10 K below the transition[42,75]. In contrast, previous studies on YBCO films[48,49] and another study of YBCO crystals[76] do not observe the static critical exponent.

3.2 YBCO Film Growth and Properties

YBCO films are grown in our lab by pulsed-laser ablation. The laser is an excimer laser utilizing an Ar-Fl gas. Samples are grown at a temperature of 790-850 C in 500 mTorr of oxygen and are post annealed at 425 C for 1 hour in an atmosphere of oxygen.

The film presented was grown on a $10\times10\times0.5$ mm $SrTiO_3$ substrate grown by Chris Michaels and William Neils. This film had a higher transition temperature than other YBCO films measured and is an optimally-doped film. The thickness, determined from optical ellipsometry, is 505 Å. A unit cell has a thickness of 11.7 Å, and therefore the film has approximately n=43 layers. YBCO has a c-axis coherence length of 5 Å and 25 Å in the c and a-b directions, respectively[59]. The penetration depth from optimally doped crystals is 1400 Å.

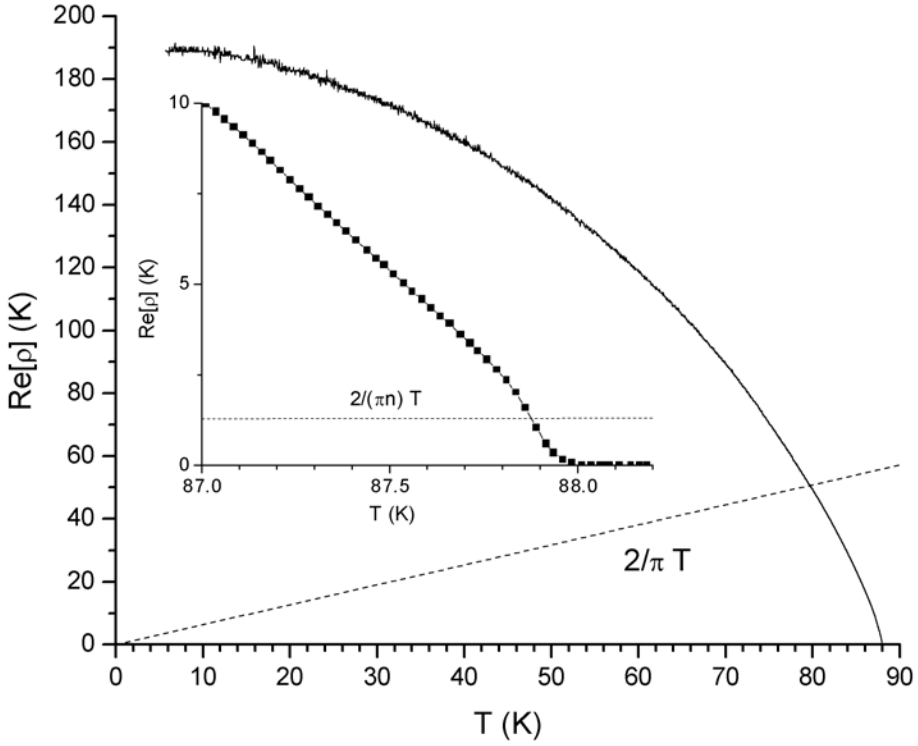

Figure 10: Temperature dependence of Re[ρ] in laser-ablated YBCO film.

Figure 10 is a plot of the superfluid density versus temperature. The penetration depth at 5 K is 1950 Å, which is similar to other laser-ablated films, but is larger than the penetration depth of YBCO crystals (1400 Å). The superfluid density was measured at 100 kHz and 50 μA. The low-temperature dependence of the superfluid density is quadratic, similar to other laser-ablated films[49], and is probably caused by impurity scattering[77]. The figure shows the KTB critical superfluid density, $(2/\pi)T$, for the transition of an isolated unit cell. The superfluid density crosses smoothly through the universal line, indicating an absence of strong phase fluctuations associated with the

individual layers. Some measurements on YBCO films reveal features around this temperature[51]; these are especially strong in oxygen depleted films[78].

The inset to Figure 10 shows the superfluid density close to T_c and the KTB line for the entire thickness of our film, $(2/\pi n)\,T$. Comparison with the KTB line for the film thickness is reasonable, since from equation (1.15) $\lambda = 1.2\,\mu m \gg d_{film}$ at 87.55 K. As the temperature is increased, the superfluid density drops close to the universal line, indicating a quasi-2D transition in a film with small doping inhomogeneity. We regard this as an important criteria for film quality, since the measured critical behavior will depend strongly on sample homogeneity. Note that the 3D-2D crossover predicted by the 3D-XY model, $0.5/n\ T_c$, is close to the KTB transition temperature, and either temperature will approximately describe a crossover to 2D.

3.3 Analysis without Film-Diameter Correction

The first study of the static critical exponent with this technique, reported that a film diameter correction can change the apparent critical exponent[48]. Even though our film is thin ($d \ll \lambda$) and the film-diameter correction approaches zero as the temperature approaches T_C, the correction is not negligible. To resolve these issues, we analyze the data with and without the film-diameter correction. We will first analyze the data without the film-diameter correction and then see how the data close to T_C is perturbed by the correction.

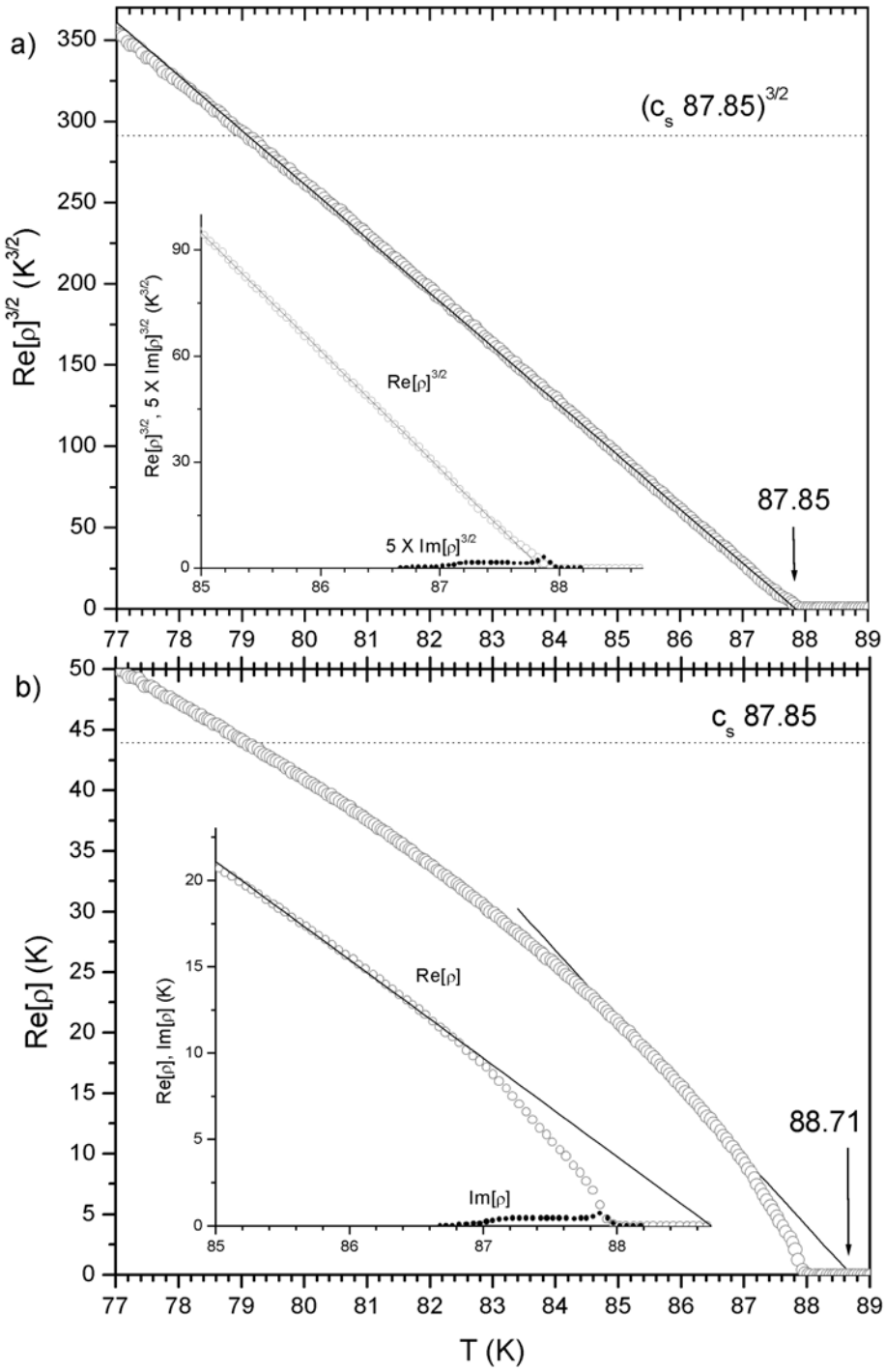

Figure 11: $\mathrm{Re}[\rho]^{3/2}$ **(panel a) and** $\mathrm{Re}[\rho]$ **(panel b) versus temperature around T_c without the finite-film diameter correction.** $\mathrm{Re}[\rho]^{3/2}$ **is linear from 84.5 to 87.5, indicative of 3D-XY critical fluctuations.** $\mathrm{Re}[\rho]$ **is not linear and a linear extrapolation overestimates the transition temperature.**

In Figure 11 a) and b) $\mathrm{Re}[\rho]^{3/2}$ and $\mathrm{Re}[\rho]$ are shown, respectively, without the film-diameter correction. The transition temperature of the film is located within the peak in Im[ρ] at 87.83 ± 0.10 K (see insets to Figure 11). A tail in Im[ρ] persists down to 87 K, which may reflect dynamic fluctuations, $\rho = \xi^{2-D} S(\omega \xi^{z})$, close to the transition temperature. Linear fits are also performed on $\mathrm{Re}[\rho]$ and $\mathrm{Re}[\rho]^{3/2}$ from 85 K to 87 K. $\mathrm{Re}[\rho]^{3/2}$ is linear from 84.5 to 87.5, but no linear regime is identified for $\mathrm{Re}[\rho]$. In addition, $\mathrm{Re}[\rho]^{3/2}$ appears to be approximately linear down to 79 K, where $\xi_c \approx d$, which indicates the critical fluctuations may have influence on the decay of the superfluid density down to this temperature. It is not surprising that $\mathrm{Re}[\rho]^{3/2}$ is linear up to 87.5 K, since $(\mathrm{Im}[\rho]/\mathrm{Re}[\rho])^{3/2} \ll 1$ up to this temperature, and ξ_c has not exceeded the film thickness.

3.4 Standard Analysis of Superfluid Density

In Figure 12 a) and b) , $\mathrm{Re}[\rho]^{3/2}$ and $\mathrm{Re}[\rho]$ are shown, respectively, with the standard film-diameter correction. The transition temperature is located within the peak in $\mathrm{Im}[\rho]$ at $T_C = 87.9 \pm 0.1$ K. Linear fits are also performed on $\mathrm{Re}[\rho]$ and $\mathrm{Re}[\rho]^{3/2}$ from 86 K to 87 K. $\mathrm{Re}[\rho]^{3/2}$ is linear from 86 to 87.2 K, with an intercept of 87.82 K, but no linear regime is identified for $\mathrm{Re}[\rho]$. A comparison of the fits on $\mathrm{Re}[\rho]^{3/2}$ in Figure 11 a) and Figure 12 a) reveal that the range of linear behavior has dropped from 3 K to 1.2 K by

including the finite-film diameter correction. This indicates that the temperature range of observed 3D-XY static exponent, but not the exponent itself[48], is changed by the finite-film diameter correction.

The linear extrapolation of $\mathrm{Re}[\rho]^{3/2}$ in Figure 12 a) yields a transition temperature of T_c^{3D}=87.82 K. In Figure 12 b) $\mathrm{Re}[\rho]=(c_s/n)$ 87.82 K crosses the superfluid density very close to the transition temperature, indicating the finite film thickness only modifies the critical behavior within 0.1 K of the transition temperature. The transition temperature of the sample is modified in principle by the film thickness, but the modification in the transition temperature is unobservable since T_c^{3D} is located within the dissipation peak.

We conclude that critical fluctuations are clearly observed in a YBCO film, although the range of observed critical fluctuations can be altered by the analysis. The finite diameter correction changes the apparent range of critical fluctuations, but does not change the observed exponent. Static critical fluctuations are observed over a 1.2 K temperature interval after the film diameter correction and 3.0 K before the film diameter correction. In terms of the reduced temperature $\varepsilon = 1 - T/T_c$, critical fluctuations are observed between 7.1×10^{-3} and 2.1×10^{-2} after the film diameter correction and between 4.0×10^{-3} and 3.8×10^{-2} before the correction. Since the range of the 3D-XY critical exponent is larger without the film-diameter correction, further numerical studies of the finite-diameter correction would be useful. The film diameter correction used in the following chapters on BSCCO was relatively insensitive to the film diameter correction.

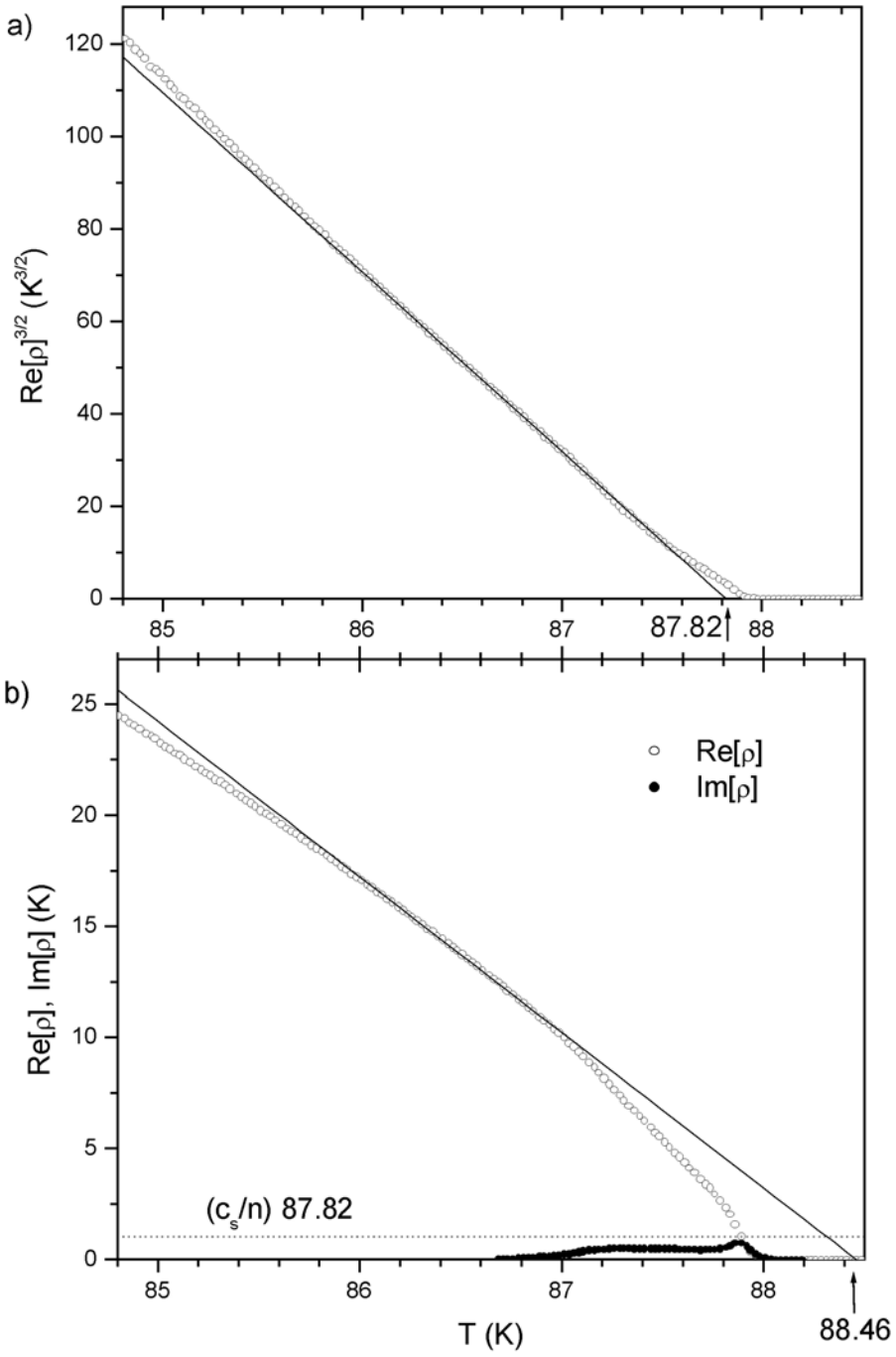

Figure 12: $\mathrm{Re}[\rho]^{3/2}$ **(panel a) and** $\mathrm{Re}[\rho]$ **(panel b) versus temperature around** T_c. $\mathrm{Re}[\rho]^{3/2}$ **is linear in temperature, indicating 3D-XY critical fluctuations, and approximately predicts the transition temperature** T_C. $\mathrm{Re}[\rho]$ **is not linear and overestimates the transition temperature.**

4 Superfluid Density in Doped BSCCO Films

The superfluid density in BSCCO is influenced by the high-anisotropy near the transition temperature, however the doping dependence of the low-temperature superfluid density is expected to be similar in all cuprates. In a heavily underdoped film, the KTB signature in the superfluid density indicates that BSCCO films become more anisotropic as the hole doping is reduced. In the films near optimal doping, the low temperature superfluid density is found to agree with a model of a critical doping state at 0.19 holes per Cu in agreement with a second order parameter model of the pseudogap. In addition, there is no observed interaction of T* with the superfluid density at temperatures $0<T<T_c$, which puts restrictions on second order parameter model.

4.1 Previous Measurements on BSCCO

The large anisotropy of BSCCO has complicated measurements of the in-plane penetration depth. Early measurements of the penetration depth using a parallel plate resonator technique found a T^2 dependence to the penetration depth[79], which was ultimately attributed to the slight misalignment of the substrate in combination with the large anisotropy[80]. Microwave penetration depth measurements on BSCCO crystals[81,82] have observed the expected linear temperature dependence, using published values of the zero-temperature penetration depth in the range from 2100 to 3000 Å[83]. Measurements

of the superfluid density close to the transition temperature will be discussed in the next chapter.

4.2 BSCCO Structure and Film Growth

In Figure 13 the crystal structure of $Bi_2Sr_2CaCu_2O_{8+\delta}$ (Bi-2212) is shown. A unit cell is approximately 15.4 Å along the c-axis direction and easily cleaved between the Bi-O_2 planes, which are separated by 3 Å. The in-plane Cu-O bond distance is 1.9 Å. The Ca and Sr-O sites control the number of holes available for conduction in the Cu-O_2 planes. At optimal doping, δ is approximately 0.38.

The BSCCO films tested were grown by Seongshik Oh and Jim Eckstein using molecular-beam epitaxy[84]. The growth of each atomic layer is deposited in sequence from an array of shuttered thermal effusion cells. High effective oxygen pressures are obtained by inserting ozone into the MBE system close to the substrate. During growth, RHEED is used to monitor the quality of the crystalline film. The films are grown on $SrTiO_3$ and $LaAlO_3$ substrates and 2 layers of Bi-2201 are used to relax the lattice constant before growth of the Bi-2212 film. X-ray diffraction measurements confirm that the c-axis lattice constant is similar to crystals.

Figure 13: Crystal Structure of $Bi_2Sr_2CaCu_2O_{8+\delta}$

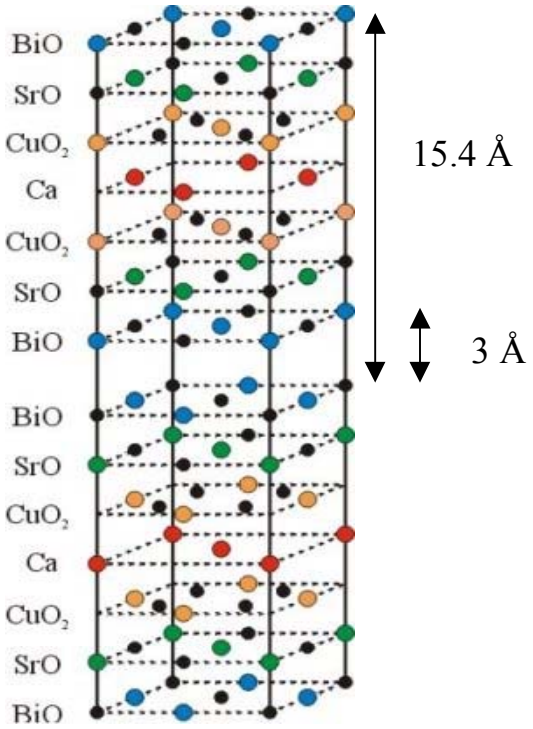

Resistance measurements were taken with the van der Pauw technique on all films to monitor sample quality and hole doping. In Figure 14 the resistance for a optimally doped (OP), critically doped (CD), and overdoped film (OD) are shown, normalized by the resistance at 290 K. Typical of high-temperature superconducting films, the resistance above the transition is nearly linear. A fit to a second order polynomial $R = a + bT + cT^2$ reveals the that the curvature, $\alpha \equiv c/b$, was negative for films doped below critical doping, zero at critical doping, and positive for doping above the critical doping. The inset shows the resistance normalized by a linear fit from 225 to 275 K, which shows the curvature for the films with different doping.

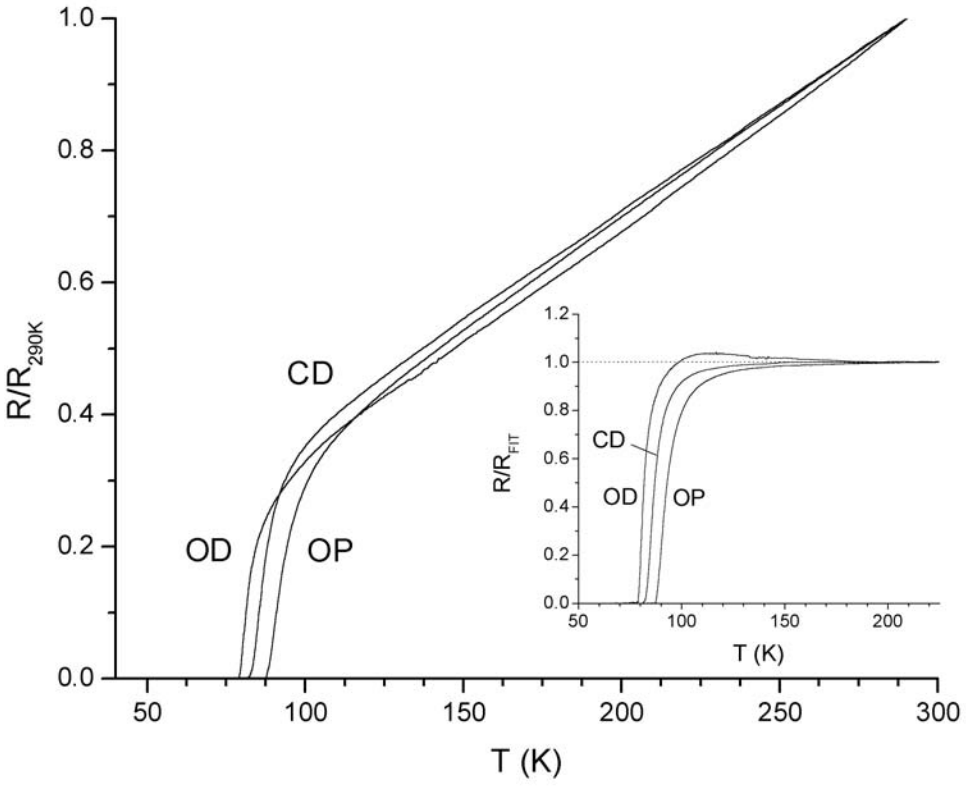

Figure 14: Resistance normalized to 290 K for optimally doped (OP), critically doped (CD), and over doped (OD) film. The inset shows the same films normalized to a linear fit at high temperatures.

4.3 Low Temperature Behavior

The interpretation of the low-temperature superfluid density in the BSCCO films is complicated by two factors. The substrates have a small miscut angle of the substrate, which may change the temperature dependence of the low-temperature superfluid density by mixing in a c-axis component of the penetration depth. In addition, a thin Bi-2201 superconducting buffer layer used to relax the lattice constant before growth of Bi-2212

adds to the screening signal at low temperatures and obscures the superfluid density of Bi-2212 in some films.

The $SrTiO_3$ and $LaAlO_3$ film substrates provided by the manufacturer are nominally oriented with the c-axis normal to the substrate, but have a miscut angle of 0.1 to 0.2 degrees[85]. Because the film grows with the same orientation as the substrate, the film will grow with a-b planes that terminate at the top and bottom of the film. In a 600 Å thick Bi-2212 film on a 0.1 degree miscut substrate, stripes with a width of approximately 34 microns in the a-b plane will form. Because the two-coil inductive technique forces currents to flow in the plane of the film, currents will flow along the c-axis direction, in addition to the a-b planes.

In general our measurements of the superfluid density in BSCCO films vary quadratically with temperature. In Figure 15 the low temperature superfluid density for a series of films is plotted as a function of T^2. The films are labeled in order of increasing doping, starting with film "a". Details of the doping and transition temperature of film "a" through "i" are described in section 4.6. Most of the superfluid density curves in the figure show at T^2 dependence up to approximately 40 K. The c-axis penetration depth of BSCCO and other cuprates[86] varies as T^2, which is caused by either impurity scattering[87] or Cooper-pair tunneling[88]. Since our measured low-temperature superfluid density varies as T^2 and is consistent with c-axis measurements, we attribute this temperature dependence to small c-axis currents caused by the miscut angle of the substrates.

Evidence for a T dependence is seen in an underdoped film below and is consistent with this picture.

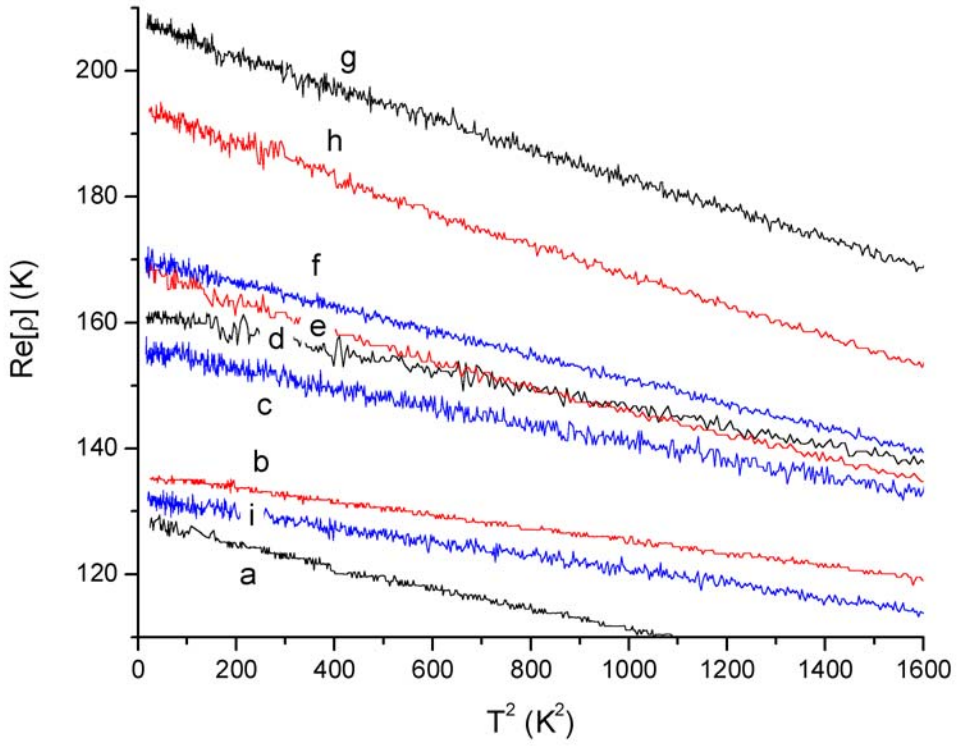

Figure 15: Low-temperature superfluid density versus T^2 in Bi-2212 films. Films a through i are labeled in order of increasing hole doping. The doping levels are given in Table 1.

Two buffer layers of Bi-2201 are grown before every Bi-2212 film to match the lattice constant before growth. The screening from these buffer layers is significant in underdoped films where the total screening of the 2201 layers is comparable to the screening of the 2212 layers. Since the sheet superfluid density is calculated from the number of 2212 layers, additional screening from 2201 layers will cause an additional (error) signal in the superfluid density at low temperatures.

The calculated superfluid density of a La underdoped film is shown in Figure 16. The film has 40 layers of Bi-2212 and 2 layers of Bi-2201. The low-temperature superfluid density is approximately an order of magnitude smaller than films in Figure 17. At 12 K there is a small bend in the superfluid density caused by the additional screening in the BSCCO-2201 layers.

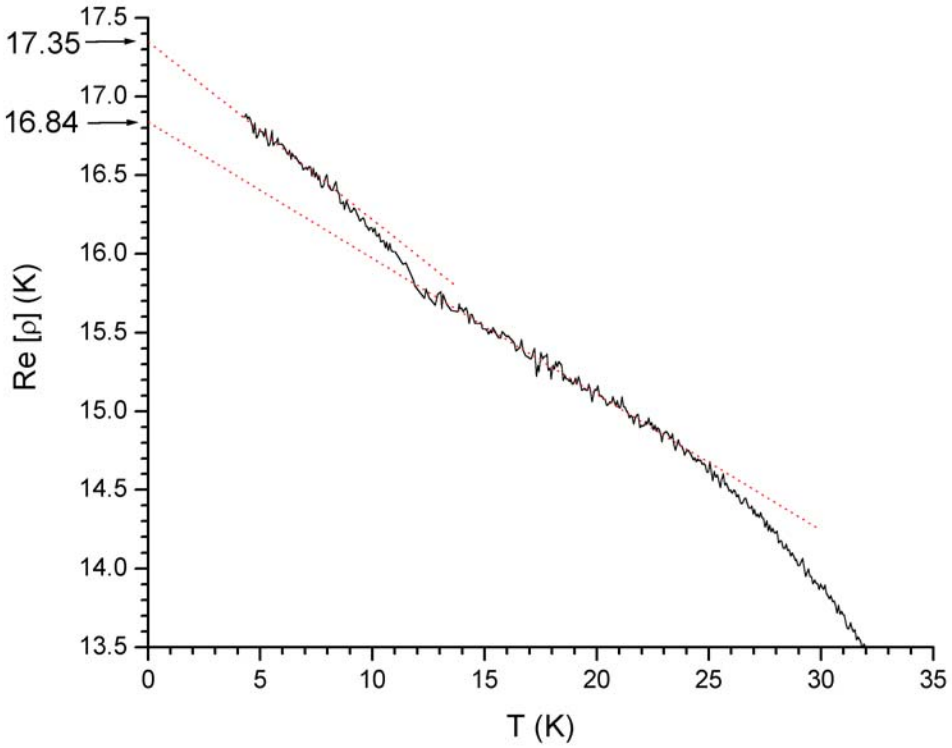

Figure 16: Calculated superfluid density of 40 layer BSCCO-2212 film. Below 12 K, a signal from the 2 layers of BSCCO-2201 is observed.

The superfluid density is linear from 4.5 to 9K and from 12 to 24 K, indicating the superfluid density may vary with T. The functional form of the low-temperature Bi-2212

superfluid density is obscured due to the Bi-2201 screening below 12 K. To estimate the screening from the Bi-2201 layers, a linear fit is performed on the superfluid density along the two linear regions and the zero-temperature values of the superfluid density with and without the Bi-2201.

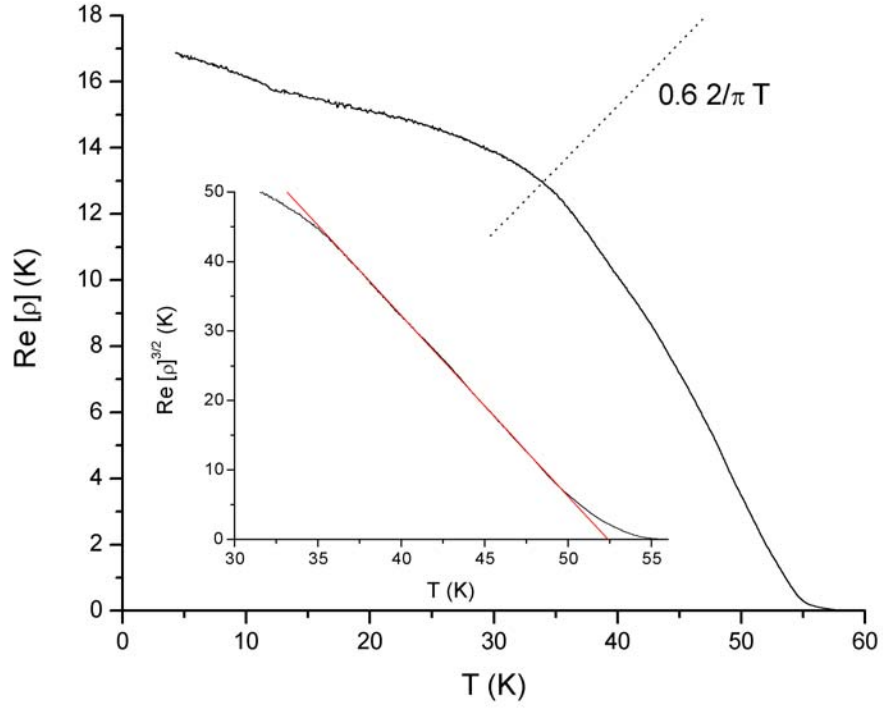

Figure 17: Superfluid density of underdoped $Bi_2Sr_{2-0.22}La_{0.22}CaCu_2O_{8+\delta}$ film. The 0.6(2/π)T line marks a crossover temperature above which phase fluctuations dominate.

The linear fit from 12 to 24 K gives a value of 16.84 K for the zero-temperature superfluid density for the Bi-2212 layers. Since BSCCO-2201 has 1 superconducting layer, instead of 2, we expect the additional signal from the buffer layers to be an additional $1/40^{th}$ of the extracted BSCCO-2212 superfluid density, or 0.42 K. The linear fit from 4.5 to 9 K reveals that the signal at zero temperature is $\rho(0)$=17.35 K, which

means that the additional signal from the Bi-2201 layers is approximately 0.51 K. This is reasonably close to our estimate, and error can be caused by the relative doping of the two superconductors.

In Figure 17 the superfluid density is shown over the entire temperature range. The transition temperature is approximately 55K. In this film, 11% of the Sr sites contain La. Since the Cu-O planes are underdoped from outside the layers, one might expect the planes to decouple, however the bend in the superfluid density occurs above the KTB transition temperaure at 0.6 (2/π) T = 0.38 T which is close to the dimensional crossover, 0.5 T_c, in the 3D-XY model. The inset shows that Re[ρ]$^{3/2}$ is linear in temperature above this line, indicating $\upsilon \simeq 2/3$.

4.4 Secondary Phase

In this section, we present a study on a heavily La-underdoped film. This film, unlike other nominally Bi-2212 films measured, does not have a single phase throughout the sample. A second phase of Bi-2223 is observed in two corners and a transition similar to a KTB transition is observed in other corners. A sharp drop in superfluid density at the KTB critical temperature indicates the layers are decoupled in some corners.

This film is grown underdoped by substituting La^{3+} into the Sr^{2+} sites to lower hole doping, without affecting the $CaCuO_2$ bilayer. In contrast, the La doped crystals can only

be grown in the Ca site. The composition of the film is $Bi_2Sr_{1.70}La_{0.30}CaCu_2O_{8+\delta}$ and is grown on a $LaAlO_3$ substrate. The sources for the elements in the MBE chamber are typically at a 30 degree angle with respect to normal, which causes a 2% nominal difference in elemental concentration from the center to the edge of the film.

In Figure 18 the film superfluid density

$$\rho_{film} \equiv n\rho = \frac{\Phi_0^2 i\sigma\omega d_{film}}{4\pi^2 k_B}, \tag{2.19}$$

is plotted, where $d_{film} \simeq 40\times 15.4$ Å, since there are nominally *n*=40 layers of the Bi-2212 film. This expression only depends on the total thickness of the film, and is therefore suitable for studying a film with a second phase. Curves 1 through 4 are taken at the corners of a 4 mm square aligned with the 14 mm square substrate. The excess concentrations of elements are shown in the inset, indicating the side of the film with the rich concentration. For example, curve 2 gives the superfluid density of a corner with a rich concentration of Sr. Curve 5 was taken at the center of the film. The largest error in these measurements is the broadening of the superfluid density curves due to the finite radius of our coils.

In corners 1 and 2, and the center position, 5, the superfluid densities are similar. At low temperatures the superfluid density smoothly decreases from 1750 K at T=4 K, which corresponds to $\lambda = 4600$Å. At 29 K the superfluid density changes slope at approximately the KTB line for a BSCCO-2212 layer transition ($2/\pi$ 40 T). At 35 K the superfluid density drops again, indicating a second transition in the film.

Based on the low-temperature superfluid density, the Ca rich side of the film exhibits a secondary phase. In curve 3, the superfluid density is 2300 K ($\lambda = 4100$Å) at T=4 K, which is 30% larger than in corners 1, 2, and 5. In curve 4, the superfluid density is 2000 K ($\lambda = 4400$Å) at T=4 K, which is also substantially larger than in corners on the opposite side of the film. The superfluid density, $\sim n_s/m$, should only change by a few percent across the measured area due to a gradient of a cation such as La. Therefore, the low-temperature superfluid density indicates that a second phase is present in corners 3 and 4.

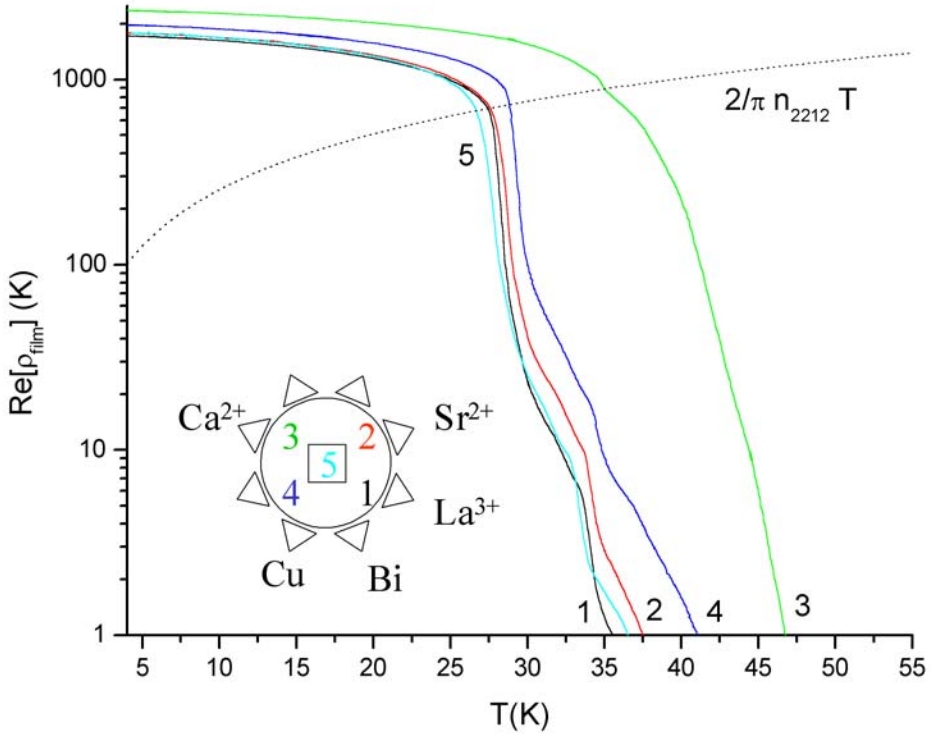

Figure 18: Film superfluid density in different elemental rich corners of $Bi_2Sr_{1.70}La_{0.30}CaCu_2O_{8+\delta}$ film.

The temperature at which the superfluid density vanishes also indicates that a second phase is present. In corners 1, 2, and 5 the superfluid density drops dramatically at 27-29 K, and exhibits a tail up to approximately 37 K at ρ_{film}=1 K. In contrast, curves 3 and 4 from the Ca rich side have a superfluid density up to 41 K and 47 K at ρ_{film}=1 K, respectively. The large change in transition temperature also indicates a second phase is present, since doping would only change the transition temperature by a approximately 2 percent across the measured area of the film.

Secondary phases have been observed in a set of crystals with different elemental concentrations[89,90], including $Bi_2Sr_2Cu_1O_6$ (Bi-2201) and $Bi_2Sr_2Ca_2Cu_3O_{10}$ (Bi-2223). These other phases are members of the homologous series $Bi_2Sr_2Ca_{n-1}Cu_nO_{2n+4}$, along with the infinite layer material $Ca_{0.85}Sr_{0.15}CuO_2$. Characterization studies on $Bi_{2+y}Sr_{2-y-x}Ca_xCu_2O_{8+\delta}$ crystals with magnetic, resistivity and X-ray diffraction, indicate an intergrowth of BSSCO-2223 occurs in Ca rich crystals[90].

The large superfluid density observed in the Ca corner can be accounted for by a large concentration of BSCCO-2223. The c-axis unit-cell distances for BSCCO-2212 and BSCCO-2223 are 15.4 Å and 18.5 Å, respectively. Because we expect the density of superconducting electrons per unit cell to remain constant, BSCCO-2223 should have a superfluid density that is approximately 25% larger. This is in reasonable agreement with the data, since Ca-rich corner 3 has a low-temperature superfluid density that is approximately 30% larger than corners 1, 2 and 5.

The superfluid density drop in curve 3 differs from the other corners. In all curves there is a drop in superfluid density close to the critical line, $(2/\pi)\, n_{2212}\, T$, for a film with decoupled layers. In curves 1, 2, 4, and 5, this drop occurs in the range 27 K to 30 K and the superfluid density at each position drops an order of magnitude over a 1 K temperature range. The location of the drop with respect to the universal line, and the sharp drop indicate the drop is similar to a KTB transition. However, in curve 3 even though initial drop in superfluid density occurs at $(2/\pi)\, n_{2212}\, T$, the drop in superfluid density is small (only 14%). It is likely that the intergrowths of Bi-2223 in corner 3

modifies the material, such that the drop in superfluid is not well described by a KTB model.

In a standard KTB transition, the superfluid density vanishes after the initial drop in the superfluid density, however this film has a second phase which modifies the transition. In curves 1, 2, 4, and 5 a small amount of superfluid density persists, and at approximately 35 K, there is a second drop in superfluid density. The second drop in superfluid density at these locations occurs at approximately the same temperature as the initial drop in superfluid density observed in corner 3, and therefore they are probably related. Since the transition in corner 3 is probably caused by thermally induced vortices and vortices will tend to flow to regions with lower superfluid density, it is possible that the second drop in superfluid density at locations 1, 2, 4, and 5 is caused by vortices that have diffused from corner 3 [91].

Standard dynamic models for the KT transition describe the transition for the dissipation associated with vortex-antivortex pair unbinding at finite frequencies[92]. In Minnhagen's dynamic model, the ratio of the real and imaginary conductivity σ_1 / σ_2 will have a peak height of $2/\pi$. In contrast, in the model by Ambegaokar *et al*. or a Drude model the peak height is predicted to be 1[93,94].

In Figure 19, σ_1 / σ_2 is plotted as a function of temperature for the 4 corner locations. At locations 1, 2 and 4, the peak height is 0.79, 0.65 and 0.61, respectively. The width of the dissipation peaks (FWHM), over the transition temperature for the locations 1, 2, and 4

are 7.0%, 6.5%, and 4.8%. The peak in location 1 and 2 are significantly broadened over location 4, due to the doping gradient across the film. Therefore the most reliable measurement for the peak ratio is 0.61, which is reasonably close to $2/\pi \sim 0.64$, and therefore agrees with Minnhagen's dynamic model and other KTB-like systems including a superconducting wire network[31,93]. The dissipation peaks at approximately 35 K correspond to the second drop in superfluid density mentioned earlier.

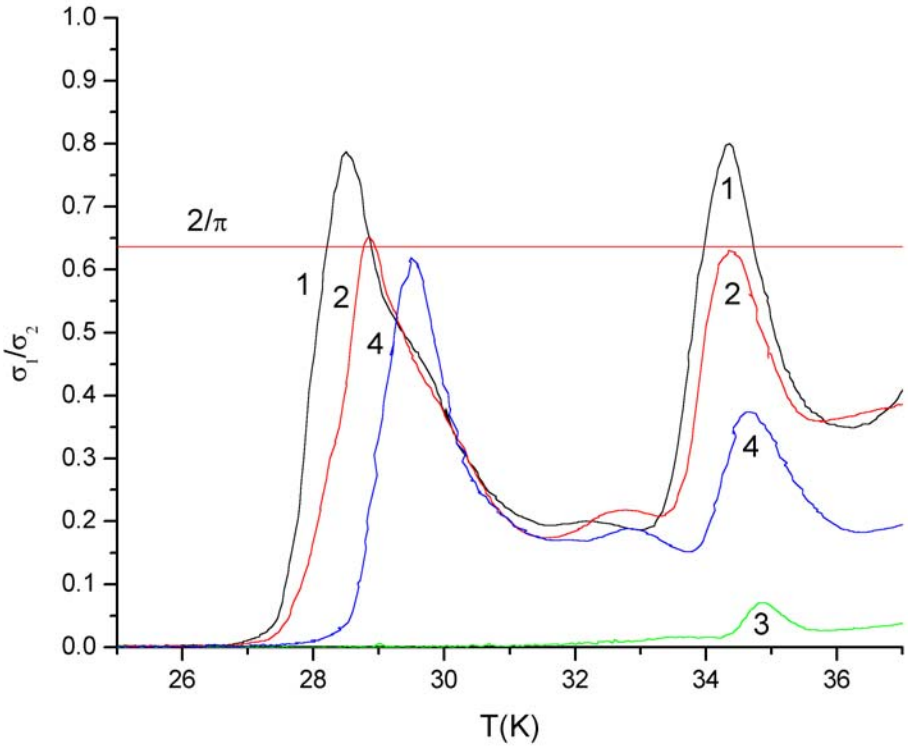

Figure 19: Dissipation peaks in different corners of La-underdoped film

4.5 Oxygen Overdoped Film

Although the doping of most films is stable over time, we have observed a change in doping due to the loss of oxygen in a heavily overdoped film. This film allows us to monitor how doping affects the superfluid density and transition temperature. There are also indications that heavily overdoped BSCCO undergoes a different transition than films with a lower hole doping.

The superfluid density of a 20-layer oxygen-overdoped film measured at 3 different times is shown in Figure 20. The sample is exposed to air between measurements. The curves t_1, t_2, and t_3, were taken 3, 71, and 105 days after growth, respectively. In these samples the low-temperature superfluid density increased from 130 K at t_1 to 140 K at t_2 and t_3. The transition temperature measured inductively is approximately 53 K, 56 K, and 58 K in chronological order at the three measurements times. Transport measurements taken on the day of sample growth and 99 days after growth revealed the transition temperature was 45 K and 65 K, respectively. The resistive transition, determined from a transport measurement with the van der Pauw technique, is typically a few degrees higher than the transition temperature determined inductively. A comparison between the resistivity and the superfluid density will be made in a later section. In this sample the resistive transition was 45 K on the day of growth, while the inductive transition temperature was 53 K only 3 days later *i.e.* the transition temperature rose at least 8 K in the first 3 days. Over time, the rate at which the transition temperature increases, slows considerably. For example, the transition temperature increased 2 K in 34 days after the 71st day.

The time dependence of the transition temperature and superfluid density is attributed to loss of oxygen. From 20 to 37 K, the superfluid density appears linear with a crossover at 37 K. It is possible that this temperature range appears linear because we are primarily measuring the intrinsic a-b penetration depth. As oxygen is lost, the anisotropy becomes larger and creates the quadratic temperature dependence observed in most of the films.

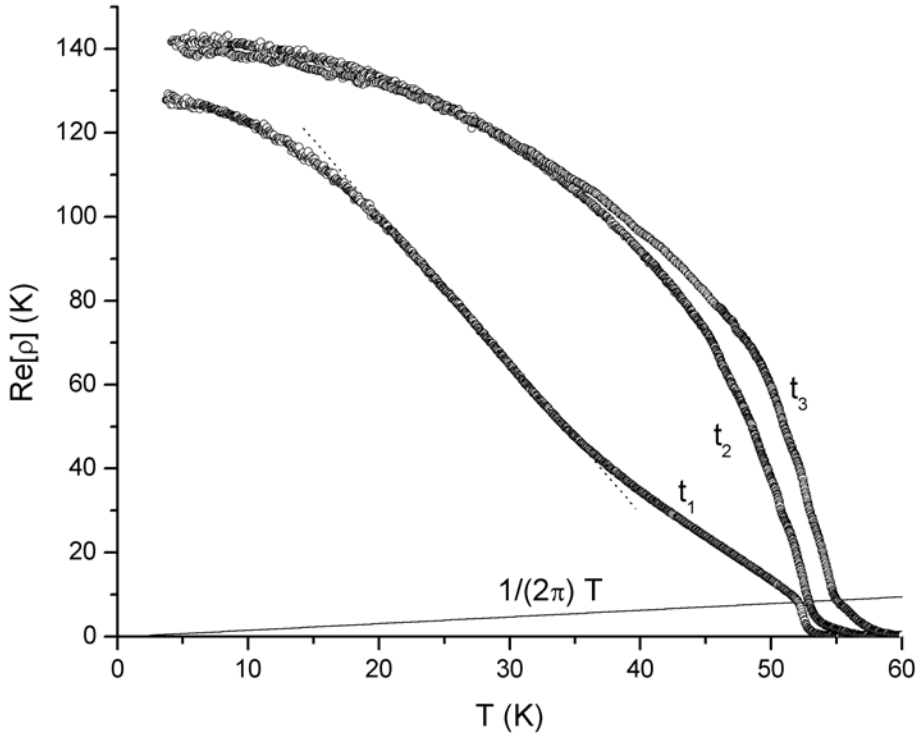

Figure 20: Heavily-overdoped Bi-2212 film measured at t_1=3, t_2=71, and t_3=105 days after growth.

The transition of the film in the heavily overdoped state has a transition different than other films measured. In Figure 21 the superfluid density is shown for the initial

measurement at t_1. From 40 K to 52 K the superfluid density decreases linearly, indicating an absence of 3D-XY phase fluctuations. At 52.2 K it undergoes a jump in the superfluid density of 1/4th the superfluid density of a Kosterlitz-Thouless transition. This is clearly seen in the inset, where the jump is equal to $(1/2\pi)$ T.

The unusual jump height is not observed on other Bi-2212 films and drops at a KTB transition temperature as if vortices have twice the flux of an ordinary vortex (n=2 in equation (1.19)). This observation is interesting in light of the spin-charge separation theory by Sentil and Fisher[95]. In addition to the spin and charge excitations (the "spinon" and the "chargon") of a standard model, they proposed a flux excitation called a "vison". This theory predicts that a *hc/2e* vortex traps a vison in a superconductor, although an *hc/e* vortex does not. In addition, if the energy of a vison is large, the creation of a *hc/e* vortex could have a lower core energy than an *hc/2e* vortex, which could modify the observed transiton.

Effects from visons are only predicted in underdoped HTS, however there are other problems with interpreting an unusual jump height as evidence for KTB transition modified by a vison. The transition on the overdoped side of the cuprates is not expected to undergo a KTB transition, especially since films with a lower doping exhibit 3D phase fluctuations (as discussed in the next chapter). Even if the layers are sufficiently decoupled, *hc/2e* vortices would normally be created at the standard transition temperature and finite size effects, such as sample size or measurement frequency, will be necessary to gap the *hc/2e* vortex excitation in order to observe the *hc/e* excitation[96,97].

More studies are needed before we can conclude the anomalous transition in the heavily overdoped BSCCO is intrinsic. Since the doping changes rapidly with time, it is likely that the unusual transition is caused by doping inhomogeneity. Films overdoped with cations are expected to be more stable and should allow a systematic study of the phase transition in heavily overdoped films.

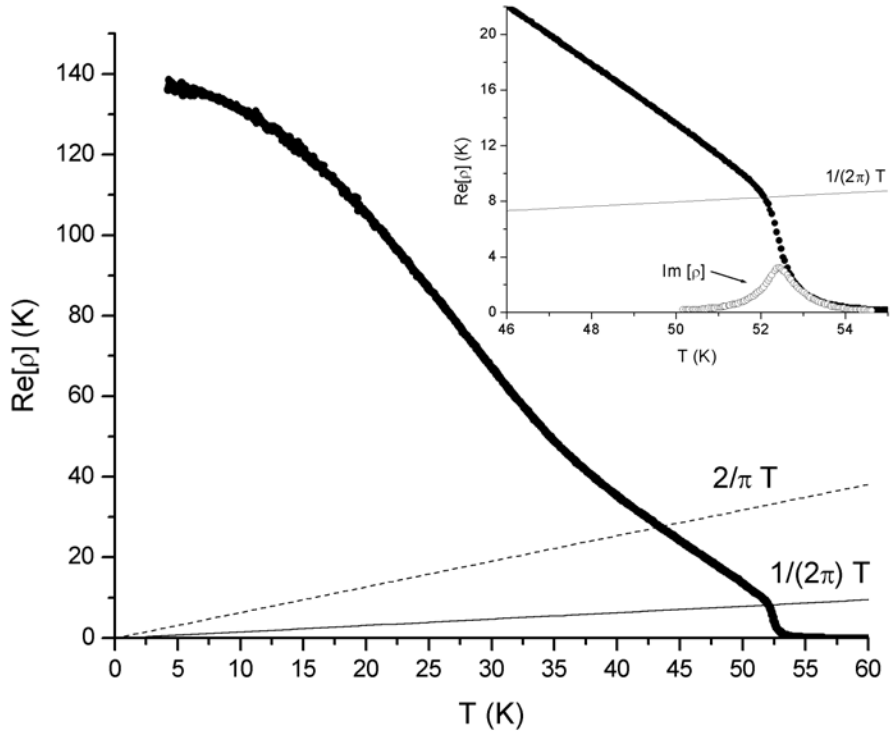

Figure 21: Superfluid density of a heavily overdoped film. The inset shows the dissipation peak and shows a jump value of 1/(2 π) T.

4.6 Doping Dependence of Superfluid Density

As shown in Figure 1, T* either merges with T_C on the overdoped side of the cuprate superconductor (curve a) or crosses through the superconducting phase and terminates at critical doping (curve b). Curve a is associated with the preformed-pair model and the Curve b is associated with a second-order parameter model. There are two possible effects curve b may have on the superfluid density. The first effect is a dramatic suppression in the zero-temperature superfluid density just below critcal doping, which is currently the primary evidence that the T* line may follow curve b. The second possible effect is based on an intuitive model of the T* line representing second-order parameter, which competes with the superconducting state. If we study the superfluid density as T crosses through T*, there may be a change in the superfluid density (perhaps seen as a change in slope) caused by the interaction of order parameters. To search for these two effects, we studied the superfluid density of Bi-2212 films near optimal and critical doping.

Studies of the superfluid density by muon-spin relaxation measurements in $Tl_2Ba_2CuO_{6+\delta}$[12], $Y_{0.8}Ca_{0.2}Ba_2Cu_3O_{7-\delta}$[12], $Tl_{0.5-y}Pb_{0.5+y}Sr_2Ca_{1-x}Y_xCu_2O_7$[98], and $La_{2-x}Sr_xCuO_4$[13], and $HgBa_2CuO_{4+\delta}$[13], reveal a peak in the depolarization rate σ at slight overdoping. In most cuprates the depolarization rate is proportional to n_s/m. In $Bi_2Sr_2CaCu_2O_{8+\delta}$, however, the high anisotropy causes pancake vortices at moderate fields which prevents the determination of n_s/m by this technique[99].

Other measurements confirm there is a peak in n_s/m, however not always at optimum doping. Two-coil inductive measurements on $La_{2-x}Sr_xCuO_4$ films studied doping dependence of the vortex activation energy and low temperature penetration depth[100]. These measurements found that n_s/m has a peak at optimal doping which contrasts reports of a peak at critical doping. Measurements on the superfluid density of Bi-2212 using magnetization measurements[101] found a maximum superfluid density at a hole doping of 0.18 and $\lambda(0)$=1900 Å. The next lowest doping in this study was near-optimally doped (p=0.15) with $\lambda(0)$=2590 Å.

The superfluid density of differently doped $Bi_2Sr_2Ca_1Cu_2O_{8+\delta}$ films was studied near optimal doping and critical doping for signatures of the high-temperature superconducting phase diagram. The transition temperature is taken as the peak in $\mathrm{Im}[\rho]$ and used in the empirical formula[102]

$$T_c = T_{c,\max}[1 - 82.6(p - 0.16)^2], \tag{2.20}$$

to obtain the hole doping. Optimally doped film b gives the maximum transition temperature, $T_{c,\max}$, at 83.74K. The curvature of the resistivity and low-temperature superfluid density indicates if a film is overdoped (p>0.16) or underdoped (p<0.16). The transition temperature and calculated hole doping of the films is shown in Table 1.

Table 1: Film properties forBi-2212 films in Figure 22.

label	Tc	p	layers	sample #
a	83.06	0.150	60	1664
b	83.74	0.160	40	1667
c	83.64	0.164	40	1669
d	83.51	0.166	40	1672
e	83.05	0.170	40	1670
f	77.89	0.189	21	1733
g	76.76	0.192	20	1748
h	74.28	0.197	20	1735
i	70.59	0.204	40	1703

The superfluid density of several films is shown in Figure 22. Film a is slightly underdoped, film b is optimally doped, and film c through film i are overdoped. The films are oxygen doped, with the same nominal stoichiometry, except film d which has a 20% Sr in the Ca sites.

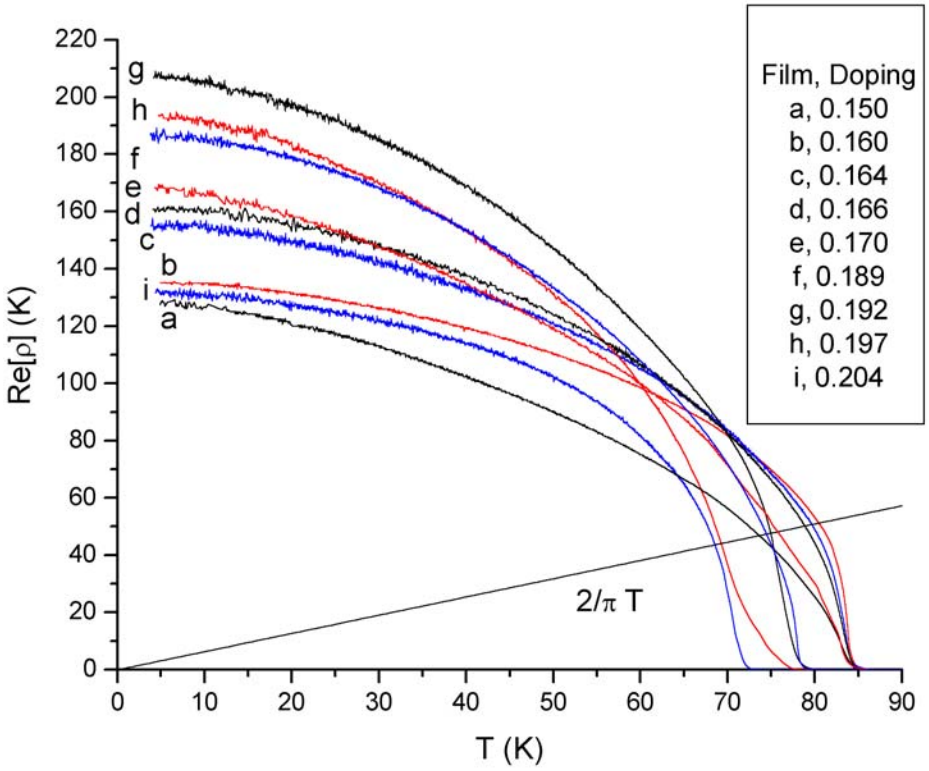

Figure 22: Superfluid density for Bi-2212 films as a function of doping.

As can be seen in Figure 22, the superfluid density curves downward around (2/π) T, indicating the onset of phase fluctuations. However, there is no abrupt drop in the superfluid density around (2/π) T, and therefore the transition is not described by a (2D) KTB model for the individual layers. The transition, primarily described by a 3D-XY model, will be discussed further in the next chapter.

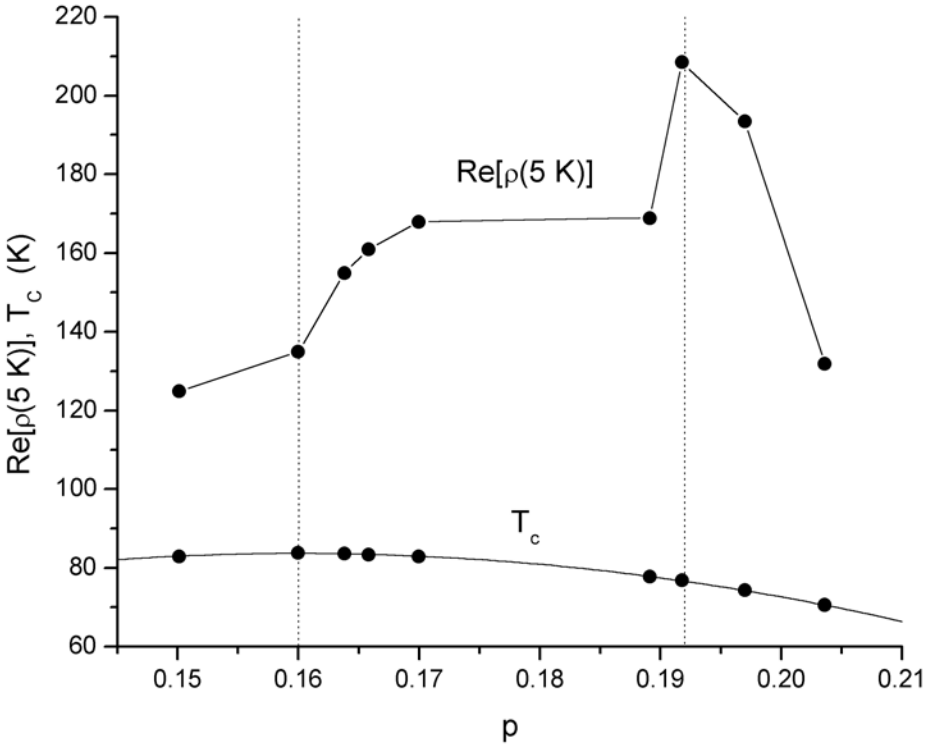

Figure 23: Low-temperature superfluid density and T_c versus doping. Optimal (p=0.160) and critical (p=0.192) doping states are marked with vertical lines.

The superfluid density at 5 K versus doping is shown in Figure 23. The superfluid density increases with hole doping up to a critical doping value of 0.192, and then decreases with additional doping. The peak in the superfluid density at 0.192 holes per Cu, corresponds to a penetration depth of 2100 Å. This is slightly larger than the value λ=1900 Å at 0.18 holes per Cu in another study[101]. At optimal doping (0.16 holes per Cu), we obtain a penetration depth of 2650 Å. From this we conclude that the peak in the superfluid density of BSCCO is at a critically doped state at approximately 0.19 holes per Cu, similar to other cuprates. The accuracy of the low temperature superfluid density is approximately 3%.

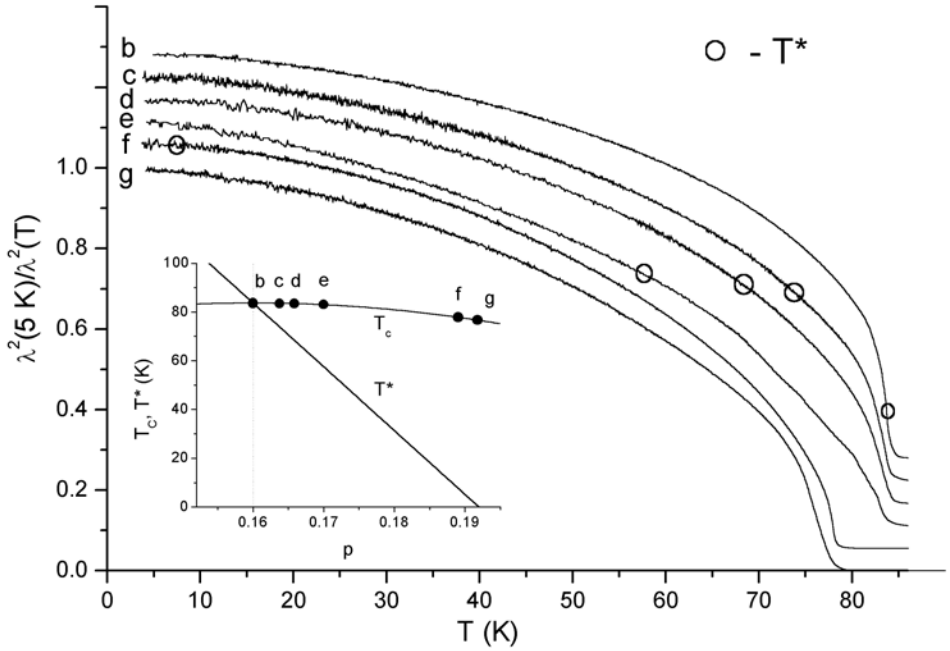

Figure 24: $\lambda^2(5K)/\lambda^2(T)$ **in Bi-2212 films between optimal (film b) and critical (film g) doping. Inset: T* at doping levels b through g in second-order parameter model.**

In Figure 24, $\lambda^{-2}(T)/\lambda^{-2}(5K)$ is shown for films b through g with a vertical offset (note that $\lambda^{-2} \propto \mathrm{Re}[\rho]$). The temperature at which T=T*, according to the second order parameter model, is marked for each curve. The inset shows T* as a function of doping for the second order parameter model and the transition temperatures of the films. In optimally doped film "b", T*=T_c; in critically doped film "g", T*=0. The superfluid density shows no features other than a change in slope $d(\lambda^{-2}(T)/\lambda^{-2}(5K))/dT$ at the lowest measured temperatures. This indicates that the superfluid density is not affected at T*, as may be expected in a second-order parameter model. Because the superfluid

density in film e ($p=0.17$) shows a bend at 68 K, it is possible that the interaction with T* occurs at this temperature.

5 Phase Transition in Doped BSCCO Films

Many experiments on YBCO have been interpreted in terms of a 3D-XY model. Transport[103,104,105,106], magnetization[107, 104], and specific heat[35, 104, 108] measurements have been observed in agreement with a 3D-XY model. In zero applied field, ac conductivity measurements[109] and penetration depth measurements[42] have found agreement with the 3D-XY Model for 5 K above and 10 K below the transition, respectively.

There is less evidence for 3D-XY critical behavior in BSCCO. In low-field conductivity measurements the 3D-XY critical regime has been reported over a relatively short, 0.5 K, temperature interval[110]. At zero field, a similarly short critical regime was reported with a crossover to Lawrence-Doniach[111] Ginzburg-Landau behavior at slightly higher temperatures[112]. In fact, dc[113] and ac[114] conductivity data on BSCCO is generally explained in terms of quasi-2D behavior.

5.1 Static 3D-XY Transition

In Figure 25 Re[ρ] is shown in the region of the transition for films "a" through "i". All the films cross smoothly through the 2D Critical line, indicating that there is significant coupling between the planes.

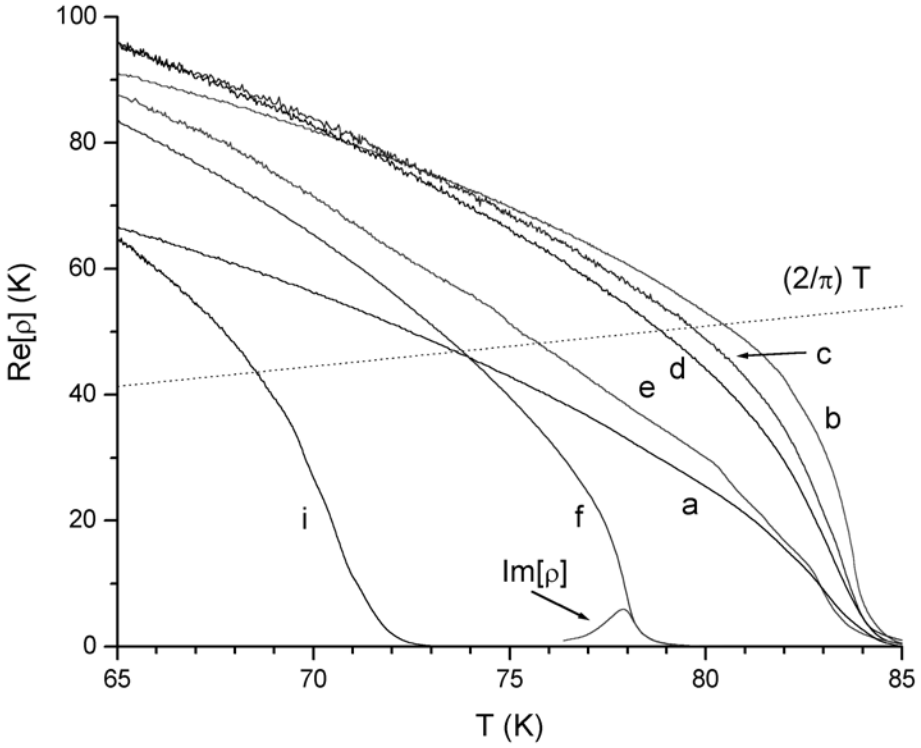

Figure 25: Superfluid density near T_c in Bi-2212 Films. The dissipation peak, Im[ρ], is drawn for film f.

In Figure 26 $\mathrm{Re}[\rho]^{3/2}$ is shown for films a, b, c, d, and f. A horizontal line approximates the superfluid density at which the c-axis correlation length is equal to a layer thickness. The curve of film a and f indicate the static 3D-XY exponent ν is observable at temperatures lower than where frequency dependence begins and $\rho \sim \xi^{-1}$. In film a the 3D-XY critical exponent is observed over a 6 K range, whereas the static exponent is only observed over a 2 K range in film f. In films b, c, and d, there is no linear regime, indicating that dynamic fluctuations are present. In addition, the curvature above the

horizontal line indicates that strong 2-D fluctuations are present before the c-axis correlation length exceeds the layer thickness.

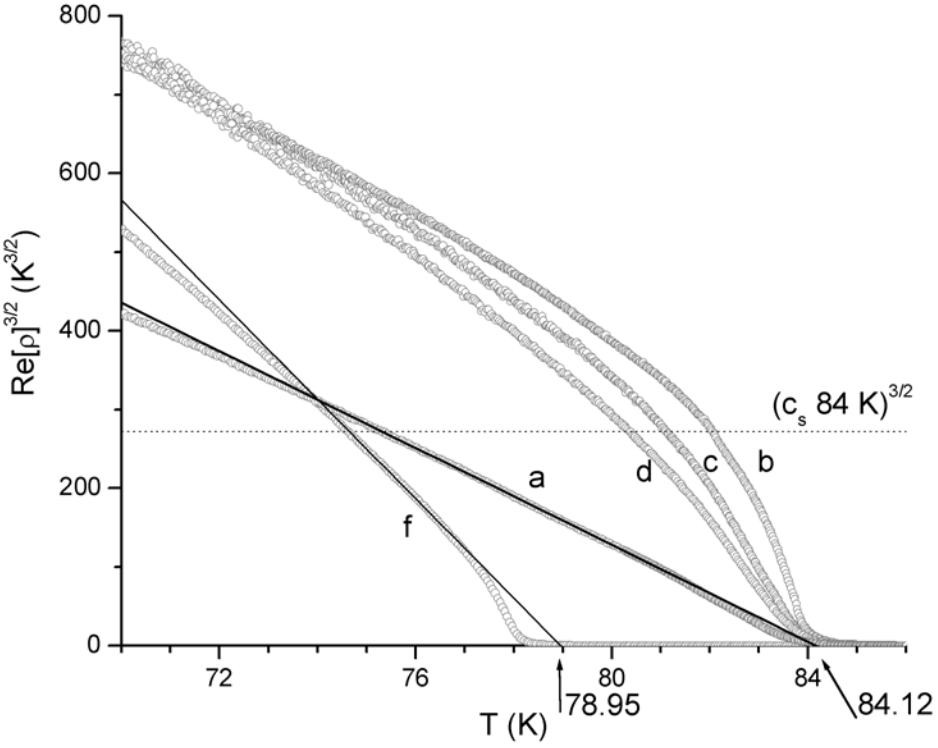

Figure 26: $Re[\rho]^{3/2}$ for several Bi-2212 films. Film a and f exhibit 3D-XY static fluctuations below T_c.

In conclusion, BSSCO films a and f on either side of optimally doped exhibit 3D-XY static critical fluctuations. Films b through d, near optimal doping, do not exhibit 3D-XY static critical behavior, however we will show in section 5.5 that this behavior is due to 3D-XY dynamic and non-linear critical fluctuations $\rho = \xi^{-1} S(\omega\xi^{z}, E\xi^{z+1})$.

5.2 Mean Field Transition Temperature

An important test for the preformed-pair model is the range of classical fluctuations, since, as shown in Figure 2, the range of fluctuations on the underdoped superconductors should be substantially larger than the overdoped superconductors. In Figure 27 the superfluid density near the transition is plotted for films with different dopings. A linear fit is perfomed on each curve for Re[ρ] from 90 to 100 K. This superfluid density range was selected because a linear decrease in superfluid density is observed here in some films and this superfluid density corresponds to $\xi_c \approx d/2$ in the 3D-XY Model. A fit with a 10% larger superfluid density will yield larger estimates for T_{MF}, however T_{MF} will have a similar dependence on doping. The deviation in the linear dependence of superfluid density is caused by phase fluctuations, which begin as 2D fluctuations and then crossover to 3D fluctuations when $\xi_c \simeq d$.

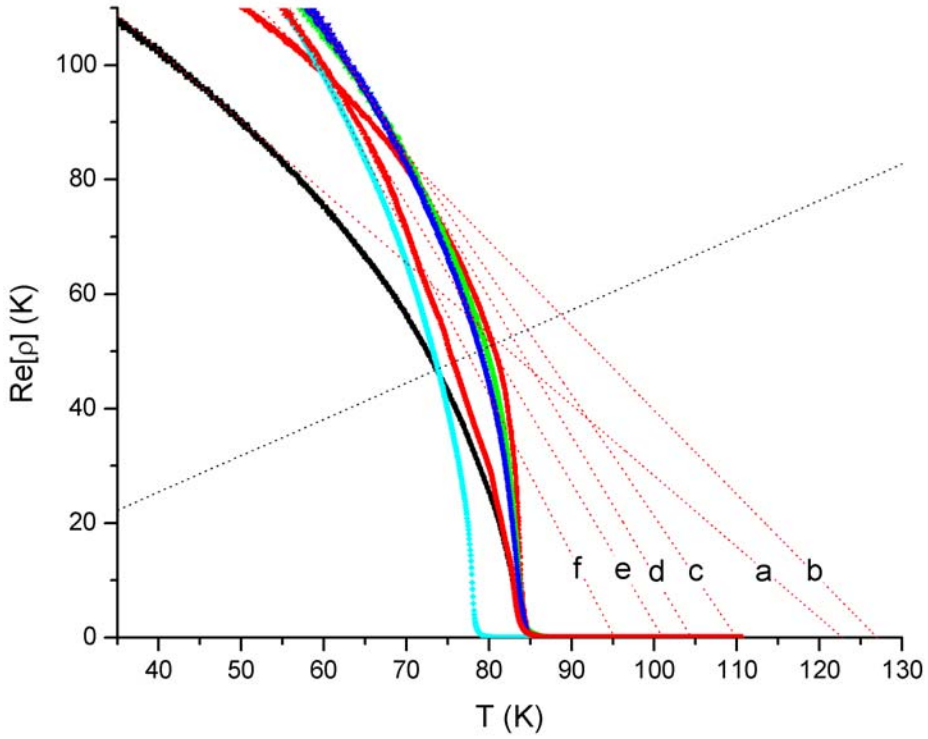

Figure 27: Superfluid density near T_c with linear fits used to estimate the mean-field transition temperature.

In mean field theory, the superfluid density would vanish at the mean-field transition temperature, where the linear fit to the superfluid density reaches zero (in the absence of phase fluctuations). In Figure 28 the mean-field transition temperature is plotted as a function of doping. The temperature range T_{MF} -T_c gives an approximation of the range of phase fluctuations, which can be compared to preformed pair model shown in Figure 2. Above 0.165 hole doping, T_{MF} decreases with increasing hole doping. Below 0.165 hole doping T_{MF} increases rapidly, indicating an increased range of phase fluctuations. The difference between the predicted mean-field transition temperature and the transition temperature is larger at lower hole dopings, which implies the phase fluctuations exist

over a larger temperature range above Tc with underdoping. Therefore there is evidence that the range of phase fluctuations is larger as one decreases the doping, in support of a performed pair model.

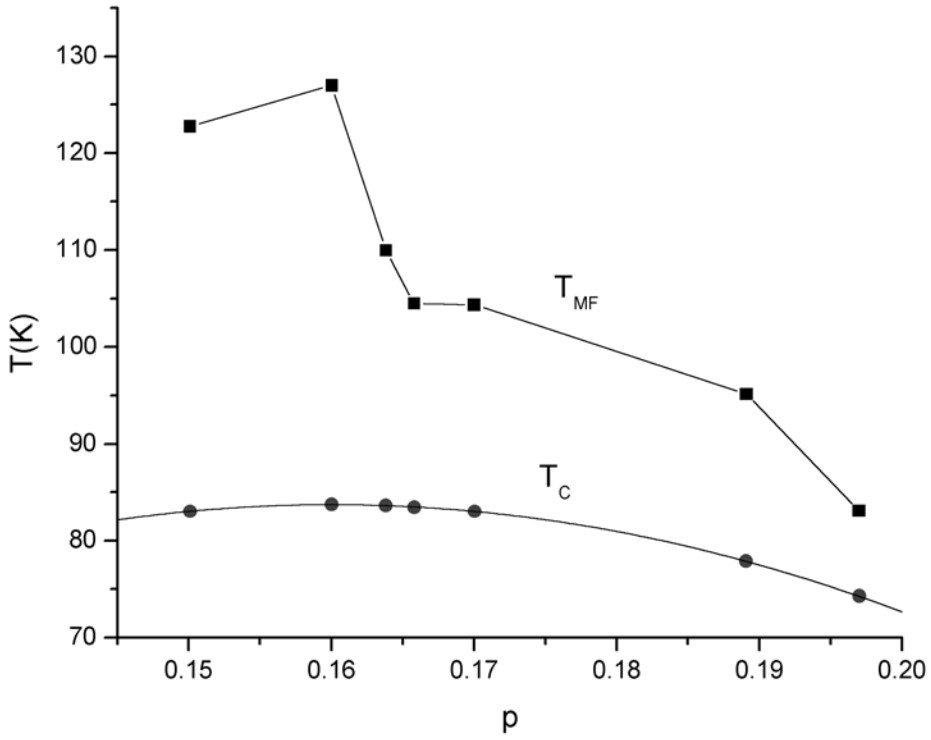

Figure 28: T_{MF} and T_C as a function of doping. T_{MF} is determined from the linear extrapolation shown in Figure 27.

The coupled layer model is not expected to apply to our system since the films show evidence of a 3D-XY transition, however a comparison is useful. In equation (1.31) and (1.33) the temperature difference T_C-T_{KTB} to be proportional to the difference between T_{MF}-T_{KTB}, assuming the non-universal constant b does not significantly change. There is no significant correlation of T_{MF}-T_{KTB} with T_C -T_{KTB}, indicating the theory does not apply

to this system or the parameter b depends strongly on doping. For example, in film b T_{MF}-T_{KTB} is much larger than in film f, although both films have a similar T_C-T_{KTB}.

The predicted temperature at which 2D phase fluctuations begin, described by equations (1.32) and (1.34), are inadequate because T_{MF}-T_{KTB} is found to be much larger than T_{2D}^{f}-T_{KTB}, whereas the model predicts that T_{2D}^{f}-T_{KTB} is approximately 2.3 times larger than T_{MF}-T_{KTB}. Previous estimates in with this model predict T_{KTB}, T_{MF}, and T_C are all within 13 Kelvin[41], whereas the difference between T_{KTB} and T_{MF} are much larger than 13 K, even by performing a linear fit over a region below T_{KTB} to determine T_{MF}. In conclusion, we find that the coupled-layer model is inadequate to describe the phase transition in Bi-2212.

5.3 Comparison with Resistivity

At present it is unclear whether there is any connection between superconducting fluctuations in the resistivity and the hole doping in high-temperature superconductors. Studies of T* in the resistivity of YBCO[115] and BSCCO[116] have been taken over a wide range of doping. These measurements are interpreted in terms of spin singlets in a resonating valence bond theory, which appears as a spin gap in NMR Knight shift measurements. Paraconductivity associated with superconductivity fluctuations, has not been studied as a function of doping. In high-temperature superconductors zero-field paraconductivity is interpreted in terms of Ginzburg-Landau[117,118] and critical fluctuations[119], however it is unclear if there is any dependence of these fluctuations with

hole doping and no consensus on method to determine T_C.

The resistance was measured with 4 point contacts on the film with the Van der Pauw method. The sample and thermometer are cooled in the vapor of a storage dewar. The thermal lag between in the thermometer and sample in the resistive measurement is less than 0.5 K. The thermometers for the resistive and inductive measurements both measure 77.3 K in the same LN_2 bath.

In Figure 29 the normalized resistivity is compared to the superfluid density. The "resistive transition temperature" T_R is obtained by extrapolating to the zero resistance temperature from the slope of the resistance at 10% of the resistance at 290K. The functional form of the resistivity does not fit an Aslamazov-Larkin or critical fluctuation theory and therefore the transition temperature cannot be obtained from the resistivity data.

The transition temperature T_C is determined by fitting a straight line to $\mathrm{Re}[\rho]^{3/2}$. This method is a precise determination of T_c in film a and f , which exhibit 3D-XY static behavior, and a good approximation in films b, c, and d, which exhibit dynamic fluctuation effects close to T_c. Film e has a unique critical behavior which is discussed in the next section, but is left out of this analysis. Drive current sample heating was studied in the inductive measurements and was eliminated as an error source.

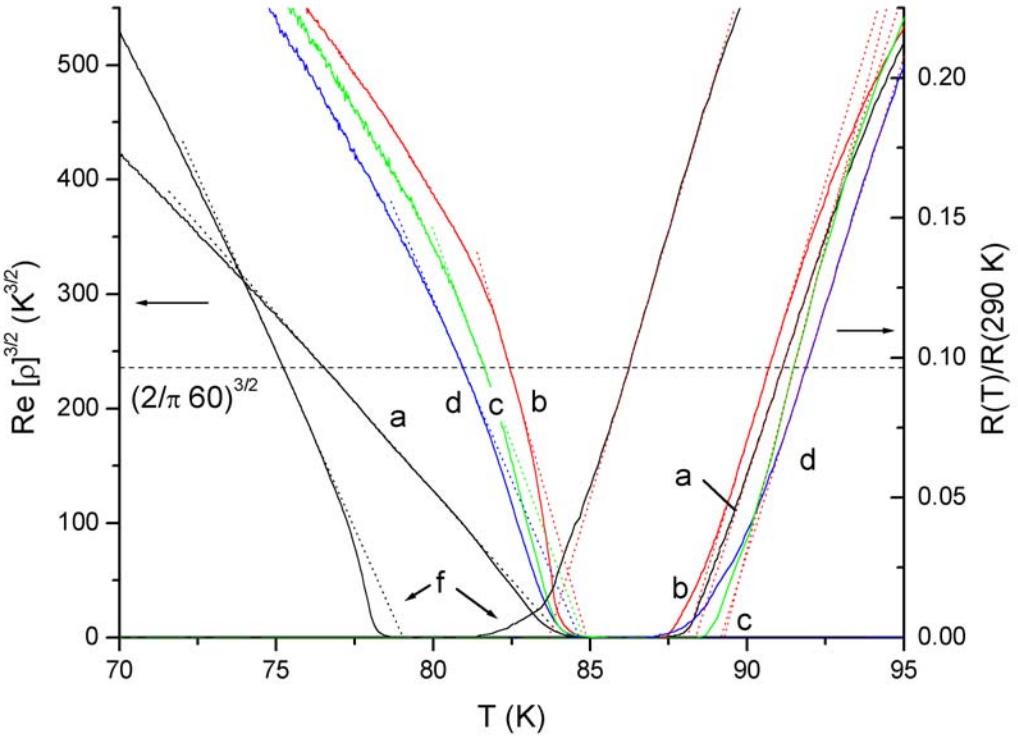

Figure 29: Superfluid density and normalized resistivity close to T_c.

In Figure 30 T_R and T_c are plotted versus hole doping, p. If the temperature difference T_R-T_C measures a range of strong phase fluctuations above T_C, then there is no significant doping dependence to the range of phase fluctuations, in disagreement with the preformed-pair model shown in Figure 2. This analysis suggests that the temperature T_R is a measurement of a mean-field transition temperature, which is higher than the critical temperature, T_c. In future work, a simultaneous resistive and inductive measurement may help determine the meaning of T_R and more precisely determine the doping dependence of T_R-T_C.

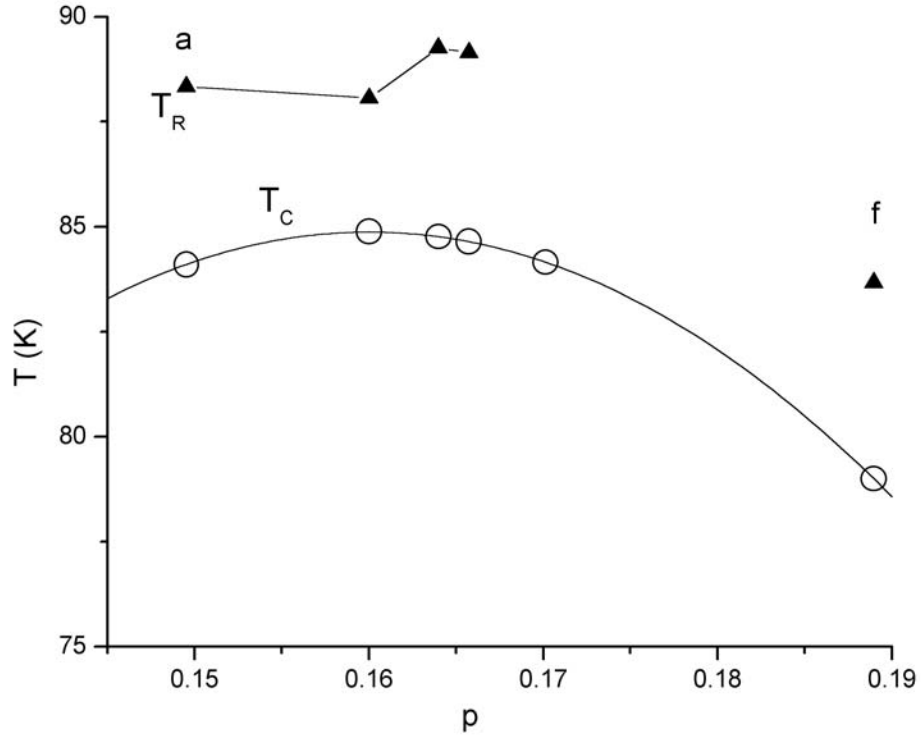

Figure 30: T_c and T_R as a function of hole doping. T_R is determined by the linear extrapolation shown in Figure 29.

5.4 Interaction with the c-axis Correlation Length

The superfluid density indirectly probes the correlation length in a 3D-XY Model. This is most readily seen in the static 3D-XY critical behavior ($\rho \sim \xi^{-1}$) of films a and f, where $\rho \sim (T_c - T)^{2/3}$ is observed, as a result of the temperature dependence $\xi^{-1} \sim (T_c - T)^{2/3}$ predicted in a 3D-XY model. As described below, dynamic critical behavior ($\rho \sim \xi^{-1} S(\omega \xi^{z})$) is necessary to describe films b through d. In these optimally

doped (a through d) and critically doped (f) films, the superfluid density varies smoothly, as ξ increases.

In contrast, film e has a doping of 0.17 and exhibits quantized features in the superfluid density which are related to the c-axis correlation length passing through the layers of the film. According to the static 3D-XY model, the c-axis correlation length is related to the superfluid density $\rho = c_s d\, T_C / \xi_c$, as seen in equation (1.29). In film e, we observe $\rho \approx c_s d\, T_C / \xi_c + F[\xi_c - nd]$, where $F = 0 (\neq 0)$, for $\xi_c \neq nd\,(= nd)$, where n is an integer. This implies that the superfluid density and c-axis correlation length interact with the discrete layers of this film.

$\mathrm{Re}[\rho]^{3/2}$ is shown for film e in Figure 31 a) , and exhibits linear decay similar to static scaling behavior, except for cusps in the superfluid density. There are 3 immediately visible cusps, at approximately 74.5, 80.5, and 82.5 K. On the right-hand axis we set the axis $(d/\xi_c)^{3/2}$ using equation (1.29) with values $c_s = 0.65$ and T_c=84 K. In addition, horizontal lines are drawn at $(1/n)^{3/2}$ for n=1, 2, 3, and 4 on the right-hand scale to represent the location where the c-axis correlation length passes through layers of the film. The three visible cusps occur close to the predicted value of the c-axis correlation length passing through 1, 2, and 4 layers of the superconducting film.

In Figure 31 b) the numerical derivative of the data in panel a), $\mathrm{d}\,\mathrm{Re}[\rho]^{3/2}/\mathrm{d}\,T$, is shown to locate the feature for $\xi_c = 3d$. As part of the cusp around T=80.5 (n=2), there are dips at T=80.3 and T=80.6 K, indicating a large slope, and a peak between these two values at

80.4 K, approximating the center of the cusp. Similarly, at T=81.7 K, there is a peak in the derivative between two large dips, which locates a small cusp at n=3.

The location of the 4 cusps are located by a pertubation of the standard 3D-XY theory with no free parameters other than adjustment of the constant c_s to a value of 0.65, which is 30% larger than an estimate given by calculation. This gives strong evidence that we are observing an interaction between the superfluid density and the layers of the film. In a system with Landau levels, magnetization and other properties are modified as the Fermi energy crosses through the quantized peaks in the density of states. In a similar way, this observation implies that the superfluid density can be modified as the correlation length crosses through layers of charge.

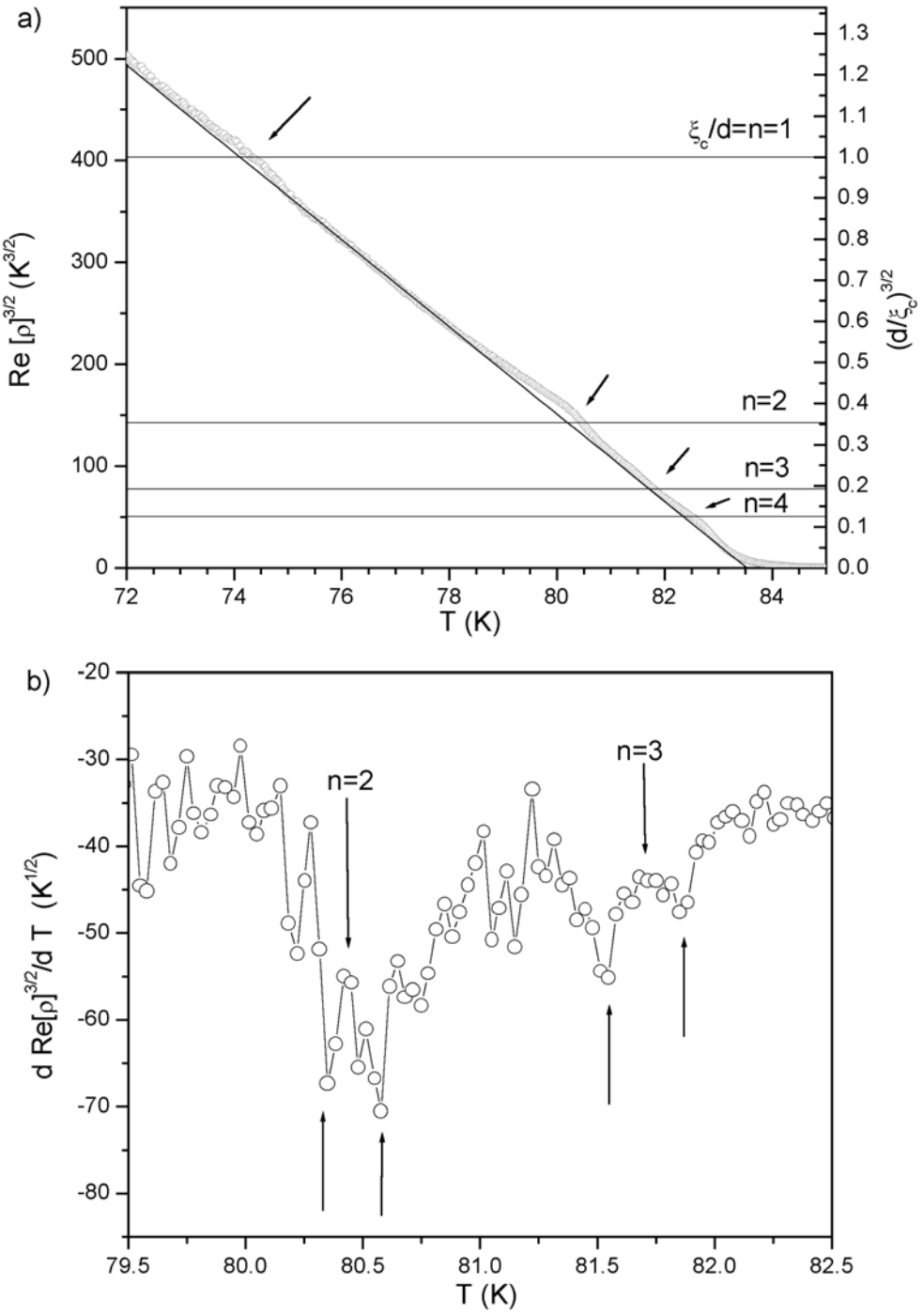

Figure 31: a) Measured Re[ρ]$^{3/2}$ versus temperature. Right axis shows $(d/\xi_c)^{3/2}$, with c_s = 0.66 and T_c=83 K. b) Numerical derivative dRe[ρ]$^{3/2}$/dT, showing features for n=2 and n=3.

5.5 Dynamic Critical Exponent

The dynamic critical exponent, z, describes the relationship between the time and size of the critical fluctuations. According to XY theory, the dynamic scaling relationship $\rho = \xi^{2-D} S(\omega \xi^z)$ describes the frequency dependence of a high-temperature-superconductor as one approaches T_c. The dimension, D, can change as the c-axis correlation length exceeds the film thickness, as observed chapter 3. We have studied the dynamic critical behavior with Vivek Aji and Nigel Goldenfeld and we report on two novel measurements of z. First we will scale the raw data, in D=2 where the c-axis correlation length exceeds the film thickness to find T_c and z_{2D}. Then, at lower temperatures where D=3, we will apply the linear-response analysis to find z_{3D}.

Measurements in HTS report different values of the dynamic critical exponent *z*. Booth et al[109] measured the microwave conductivity above the transition temperature in YBCO and found $z = 2.3 - 3.0$ and D=3, although z=2 gives reasonable agreement according to a recent model of the fluctuation conductivity[120]. In scaling studies of the non-linear transport around T_C in a $YBa_2Cu_3O_{7-\delta}/PrBa_2Cu_3O_{7-\delta}$ multilayer, a YBCO monolayer, and a BSCCO crystal, $z \approx 5.5$ was reported, assuming D=2[120, 121]. The power law of the voltage $V = I^{\alpha}$ in BSCCO also implies $z \gg 2$ for sufficiently small currents[122]. Paraconductivity measurements on BSCCO crystals (D=3) are consistent with *z*=2, but

are dependent on the static exponent ν[119]. From transport studies on YBCO in a magnetic field, the dynamic critical exponent is reported as 2.3[123,124] and 1.5[106].

The z extracted from Monte Carlo simulations of a 3D-XY model with diffusive dynamics is still unresolved. A recent paper calculates the expected result z=2[125]. However, previous Monte Carlo simulations have also found z=1.5[126] in the same (intermediate) regime where $\lambda \gg \xi$. The result z=1.5 in some experiments and simulations implies a propagating mode such as second sound in He^4. In superconductors, however, the Coulomb force typically gaps longitudinal current fluctuations which prevents this propagating mode and one expects z=2.

In previous measurements the temperature was ramped, while monitoring the magnitude and phase of the mutual inductance. In these measurements the mutual inductance was needed for several frequencies and currents close to the transition temperature. To take the necessary data, a Labview program was written to vary the applied current amplitude and frequency at a series of specified temperatures. This allowed us to characterize the dynamics and non-linear response of films.

Film b, shown in Figure 25, has a superfluid density that vanishes faster than predicted by 3D-XY static scaling, indicative of a film with dynamic fluctuations. The temperature at which the fluctuations become 3D is T_{cr}^{3D} = 81.8 K, the 3D transition temperature is approximately T_c^{2D}=85.1 K, and there are 40 layers in the film. From the 3D-XY model, we estimate the temperature range over which the correlation length exceeds the film

thickness as $\Delta T_{2D} = 2\bullet(T_c^{3D} - T_{cr}^{3D})(1/40)^{3/2} = 0.26$ K. This suggests the superfluid density in a 0.26 K range around T_c, will have 2D fluctuations. In addition, the 3D critical behavior must be analyzed at least 0.13 K below T_c, where $\xi_c < d_{film}$.

Since $\frac{d\phi_\rho}{df}$ is 0 at T_C in 3D linear-response theory, we expect $\frac{d\phi_M}{df}$ to change sign close to the 3D transition temperature. In Figure 32 the difference between the phase angle of M at 100 kHz and 10 through 90 kHz, is shown. The curves all cross through zero by T=85.08 K, indicating $T_{C,3D} \approx 85.1$ K. Close to this temperature we expect to crossover to 2D, as discussed above.

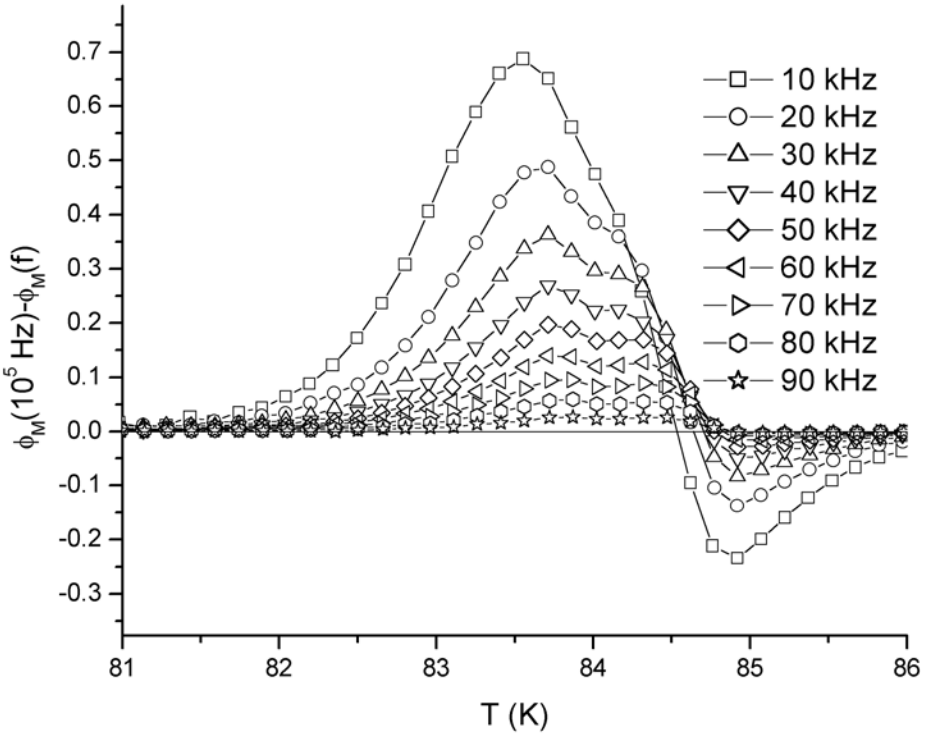

Figure 32: Mutual inductance phase angle difference versus temperature for several frequencies.

For a precise analysis of z_{2D}, non-linear scaling is performed on the raw data with a new method. According to equation (A.8), at $T=T_C$ the mutual inductance should scale as $M = F(I\omega^{-1/z})$. To find T_C and z, the mutual inductance at f=50 kHz and various currents was compared to the mutual inductance at I=100 μA for various frequencies to find the best fit for $|M| = F(I\omega^{-1/z})$. To obtain the error between the two scans a fit was performed on the mutual inductance for the constant frequency data on a scale $I\omega^{-1/z}$. The fit is adjusted for a small temperature drift between current and frequency scans (typically 0.02 K) by performing a linear correction with data at adjacent temperatures. Then the mutual inductance was extracted from the fit to compare with the constant current mutual inductance. The error is the sum of the square of the difference between the measured mutual inductance points at I=100 μA and the mutual inductance points obtained from f=50 kHz, using the formula $\Delta_M{}^2 = \sum\left(|M_{const.f}| - |M_{const.I}|\right)^2$.

In Figure 33 b) Δ_M is plotted for different values of z and temperatures. The best fit is obtained for T_C=85.22 K and z_{2D}=2.0. This is reasonable since the T_c is expected to be within 0.13 K of $T_{C\,3D}$=85.1K. A plot of the constant frequency and constant current data for different temperatures is shown in Figure 33 a) assuming z_{2D}=2. This behavior is also consistent with a similar analysis of film d.

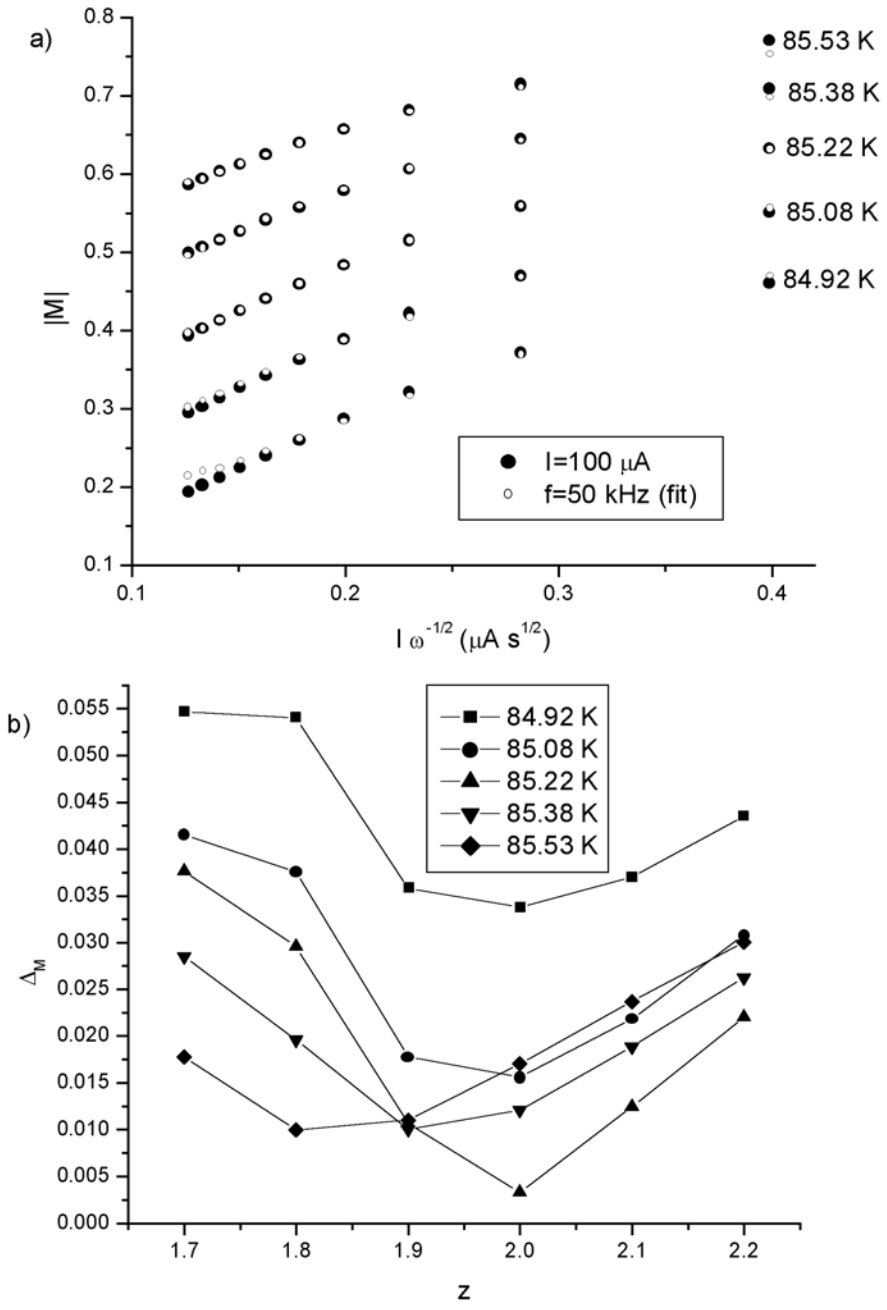

Figure 33: a) |M| versus I $\omega^{-1/z}$, where z=2. b) Δ_M vs. z for different temperatures. Minimum in error gives T_C=85.22 K and z=2.0.

To determine the dynamic critical exponent in the 3D regime z_{3D} we use the standard inversion method, which allows us to approximately extract the superfluid density below T^{3D}_{cr}, since we are close to the linear response regime. In Figure 34 a) the magnitude of ρ is plotted as a function of temperature. Using the equation (1.30), and the estimate T_c^{3D}= 85.1 K, we plot the superfluid density at which ξ_c is equal to the unit cell thickness, $c_s 85.1K$, and the thickness of the film, $c_s / n\ 85.1K$. From these two lines we get the crossover values T_{cr}^{3D} = 81.8 K and T_{cr}^{2D}=85 K. Strong frequency dependence of ρ appears shortly above T_{cr}^{3D}, indicating dynamic fluctuations are present.

In panel b) of Figure 34 the graph the phase angle of the superfluid density is shown as a function of temperature for a set of frequencies. Around 85 K the superfluid density approaches a constant phase angle. From the scaling theory, the superfluid density is expected to reach a frequency independent value of $\phi_z = \frac{\pi}{2}\frac{D-2}{z}$ in linear response scaling theory.

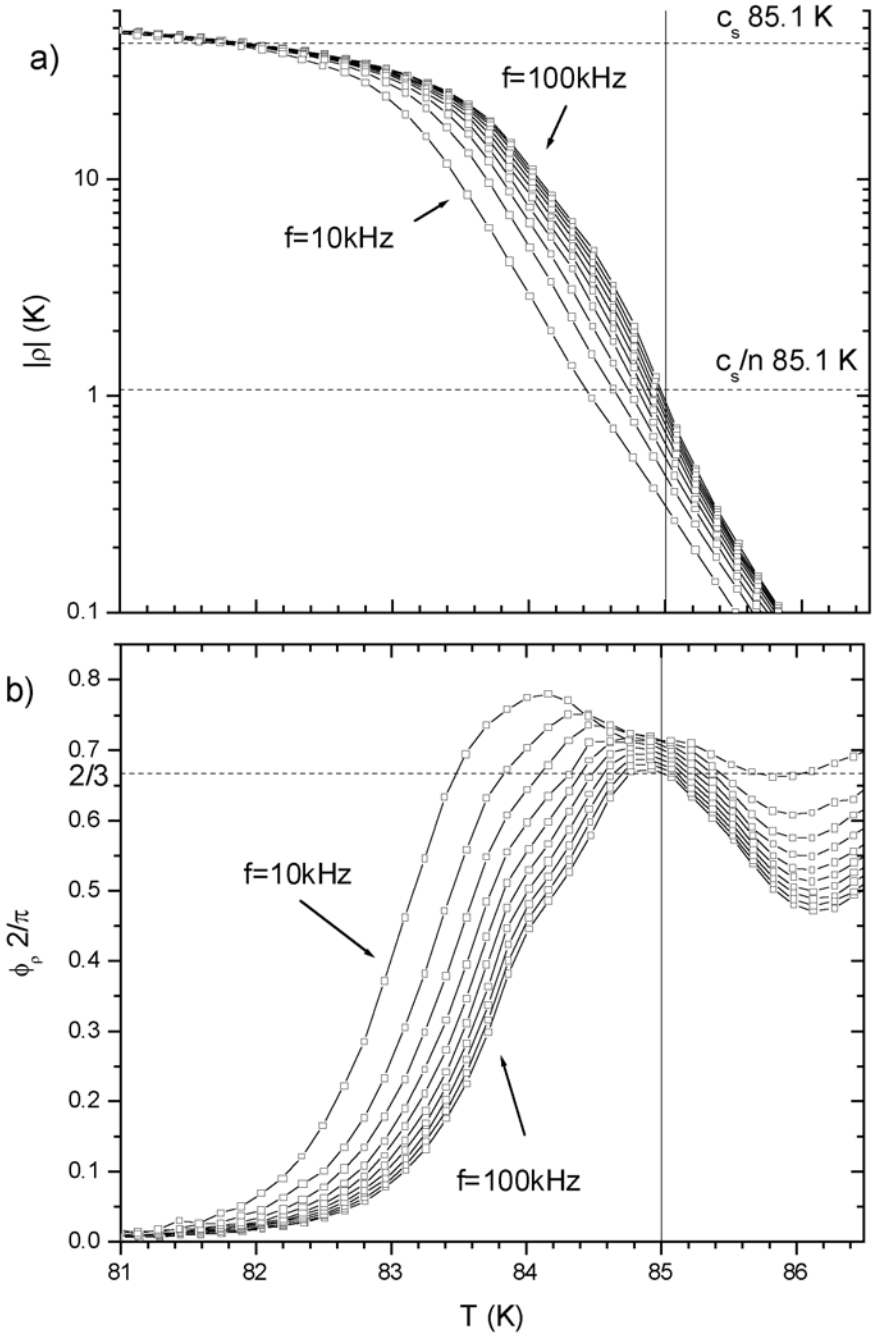

Figure 34: $|\rho|$ and ϕ_ρ versus temperature with an applied current of 100μA.

We observe a dependence of the mutual inductance on applied current and frequency. At high frequencies and low currents we should approach the linear response regime, that should give a constant phase angle from which we can extract z. In Figure 35 a) the superfluid density (also plotted in Figure 34 b) is shown below the dimensional crossover, T_{cr}^{2D}. By fitting a line to the last three points at each frequency, we see that the phase angles intersect (at T_c^{3D}= 85.1 K), as expected for system in the linear response regime. In Figure 35 b) the phase is shown at different applied currents between 50 and 150 μA at a measurement frequency of 50 kHz. A fit is performed on the last 3 points of the curves, similar to fits performed in panel a). As the current is decreased, the phase angle approaches 0.7 ($\pi/2$) at T_c^{3D}, which implies z_{3D}=1.43.

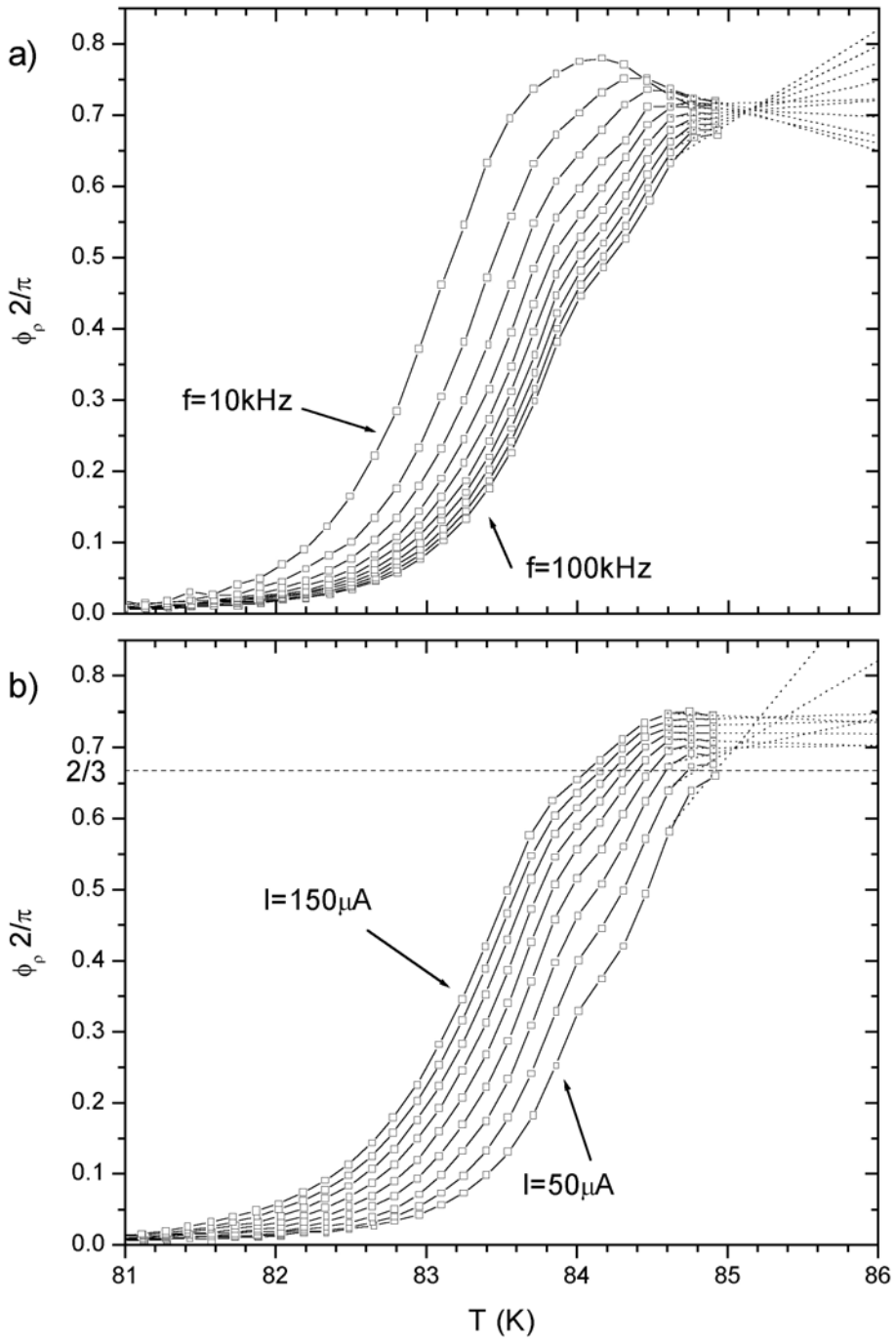

Figure 35: a) Phase angle at different frequencies with I=100μA. Linear fits indicate T_c^{3D}=85.1 K. b) Phase angle at different currents with f=50 kHz. Linear fits indicate phase angle is equal to 0.7(π/2) at T=85.1 K and therefore z_{3D}=1.43.

From linear response theory, we expect $|\rho| \sim \omega^{1/z}$ at T_c for a 3D transition in the linear response regime. In Figure 36, the magnitude of the superfluid density is shown versus $\omega^{2/3}$. At temperatures T=84.77 K and 84.62 K just below T_{cr}^{2D}, the scaling relationship holds, which supports the conclusion $z_{3D} \approx 1.5$. This result is consistent with some experiments mentioned earlier and is consistent with a propagating mode.

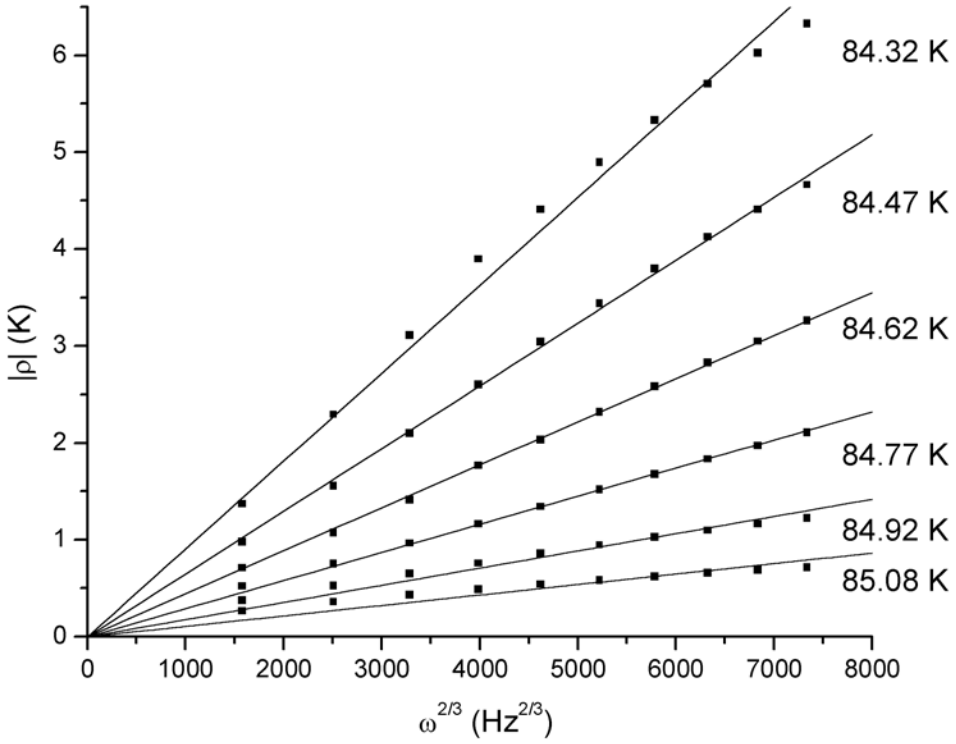

Figure 36: $|\rho|$ versus $\omega^{2/3}$ for temperatures below T_c. The drive current is fixed at 100 μA.

6 Conclusions

We have developed a two-coil inductive system that measures the superfluid density of superconducting films. The experimental system allows precise determination of the penetration depth from 4.2 K up to room temperature, in superconducting films. A numerical inversion program developed allows the superfluid density to be extracted from the raw data over several orders of magnitude.

In an optimally doped YBCO film the superfluid density vanishes according to the static fluctuations in a 3D-XY model. This result is in agreement with other studies on YBCO crystals which observe the critical exponent, but counters previous studies on YBCO films. The temperature range of the critical exponent, $\nu = 2/3$, changes as a result of the film-diameter correction, however the observed temperature range of critical fluctuations is at least 1.2 K. The dimensional crossover to 2D is observed close to T_C, where the c-axis correlation length exceeds the film thickness.

Superfluid density measurements in BSCCO films reveal many doping dependent properties. In a strongly La-underdoped film, the superfluid density appears to exhibit a universal drop in the superfluid density, indicative of KTB transition in individual layers of the Bi-2212 film. The low temperature superfluid density also exhibits a peak at a doping of 0.19 holes per Cu, which is in agreement with other doping dependent studies. In films between optimal and critical doping, we find no evidence that the pseudogap

temperature T* interacts with the superfluid density at T=T*, as may be expected in a second order parameter model.

The phase transition in near-optimally doped BSCCO is described by critical fluctuations of a 3D-XY model with crossover to 2D close to T_c, similar to YBCO films. The 3D-XY static exponent is observed in a film near optimal and critical doping over a 6 K and 2K range, respectively. From analysis of the doping dependent superfluid density we find evidence that phase fluctuations exist over a larger temperature range as doping is decreased, in support of the preformed pair model. However the range of phase fluctuations deduced by transport measurements, indicates no doping dependence. In thin optimally-doped BSCCO films, we find z_{2D}=2.0 at T_c, where the c-axis correlation length exceeds the film thickness. This result contrasts reports of a much larger z. In the 3D regime, we find evidence for z_{3D}=1.5, which indicates that high temperature superconductors have a propagating mode.

Appendix A: Non-Linear Scaling of Mutual Inductance

The scaling behavior of the mutual inductance can be calculated from the fundamental equations for the two-coil inductive technique[127]. In the Coulomb gauge the field equation is

$$\nabla^2 \vec{A} = -\mu_0 \vec{J}, \tag{A.1}$$

where $\vec{B} = \nabla \times \vec{A}$. The Vector Potential is determined by the drive current

$$\vec{J}_C = I\delta(r - r_C)\delta(z - z_C)\hat{\phi}, \tag{A.2}$$

in a coil and the current in a film around z=0 is

$$\vec{J}_f = -i\omega\sigma\,\theta(d_f/2 - z)\,\theta(d_f/2 + z)\,\vec{A}, \tag{A.3}$$

where θ is a step function. The fields in this geometry yield a field equation

$$\nabla^2 A = -\mu_0 (I\delta(r - r_C)\delta(z - z_C) - i\omega\sigma\,\theta(d_f/2 - z)\,\theta(d_f/2 + z)\,A), \tag{A.4}$$

where $\vec{A} = A\hat{\phi}$. Since $i\omega\sigma \sim \xi^{2-D} f(\omega\xi^z, A\xi)$, we can rewrite this equation as

$$\tfrac{1}{\mu_0}\nabla^2 A = \xi^{2-D} f(\omega\xi^z, A\xi)\,\theta(d_f/2 - z)\,\theta(d_f/2 + z)A - I\delta(r - r_C)\delta(z - z_C). \tag{A.5}$$

Converting the equation to dimensionless units implies that the vector potential has the scaling form

$$A = \xi^{-1} g(\omega\xi^z, I\xi, \xi^{2-D}, d_f, r, r_c, z, z_c). \tag{A.6}$$

The coil/film geometry is fixed and the voltage in a turn of a pickup coil, $i\omega 2\pi r A$, measures a mutual inductance $M = -2\pi r A / I$. This implies that the mutual inductance scales as

$$M = F(\omega\xi^z, I\xi, \xi^{2-D}). \tag{A.7}$$

At $T=T_C$, this equation reduces to

$$M = F'(I\omega^{-1/z}). \tag{A.8}$$

Appendix B: Mutual Inductance with a Cylindrical Shield

The mutual inductance for two coils on the opposite sides of a superconducting film and inside a cylindrical shield are calculated below.

In the Coulomb gauge the field equation is

$$\nabla^2 \vec{A} = -\mu_0 \vec{J}\,, \tag{B.1}$$

where $\vec{B} = \nabla \times \vec{A}$. The Vector Potential, $\vec{A}$, is determined by the drive current

$$\vec{J}_{\mathrm{C}} = I\delta\left(r - r_{\mathrm{C}}\right)\delta\left(z - z_{\mathrm{C}}\right)\hat{\phi}\,, \tag{B.2}$$

and the boundary conditions of the film

$$\vec{J}_{\mathrm{f}} = -i\omega\sigma d_{\mathrm{f}}\delta(z)\vec{A} \tag{B.3}$$

and shield. With a sufficiently conducting shield, the fields decay quickly to zero within the shield and we impose the boundary condition

$$\vec{A}(r_{\mathrm{S}}) = 0\,. \tag{B.4}$$

Symmetry provides $\vec{A} = A\hat{\phi}$ and the can be expressed with Bessel Functions of first order with roots at the radius of the shield

$$J_1(\alpha_{\mathrm{n}} r_{\mathrm{S}}) = 0\,. \tag{B.5}$$

The solution in region 1, 2, and 3 can be written as,

$$\begin{aligned} A_1 &= A_{\mathrm{c}>} + A_{\mathrm{f}>} \\ A_2 &= A_{\mathrm{c}<} + A_{\mathrm{f}>}\,, \\ A_3 &= A_{\mathrm{c}<} + A_{\mathrm{f}<} \end{aligned} \tag{B.6}$$

the sum of fields from the coil and film. The field from the coil is

$$\begin{aligned} A_{c>} &= \sum_n B_{>,n} e^{-\alpha_n (z-z_c)} J_1(\alpha_n r) \\ A_{c<} &= \sum_n B_{<,n} e^{+\alpha_n (z-z_c)} J_1(\alpha_n r) \end{aligned}. \tag{B.7}$$

The coefficients

$$B_n = \mu_0 I \frac{J_1(\alpha_n r_c) r_c}{\left[J_2(\alpha_n r_s)\right]^2 \alpha_n r_s^2}, \tag{B.8}$$

where $B_n = B_{>,n} = B_{<,n}$, can be solved from equations (B.1) and (B.2) with the orthogonality condition

$$\int_0^{r_s} r \mathrm{d}r J_1(\alpha_n r) J_1(\alpha_m r) = \frac{r_s^2}{2} \left[J_2(\alpha_n)\right]^2 \delta_{n,m}. \tag{B.9}$$

The field produced by the coil

$$\begin{aligned} A_{f>} &= \sum_n C_{>,n} e^{-\alpha_n z} J_1(\alpha_n r) \\ A_{f<} &= \sum_n C_{<,n} e^{+\alpha_n z} J_1(\alpha_n r) \end{aligned}, \tag{B.10}$$

is controlled by the boundary condition

$$\left.\frac{\partial A_{f,>}}{\partial z}\right|_{z=0} - \left.\frac{\partial A_{f,<}}{\partial z}\right|_{z=0} = d \lambda_\omega^{-2} A\big|_{z=0}, \tag{B.11}$$

where $\lambda_\omega = (i \mu_0 \omega \sigma)^{-1/2}$. The coefficients for the field produced by the film are

$$C_{>,n} = C_{<,n} = \frac{1}{1 - 2\alpha_n \lambda_\omega^2 / d} B_n e^{-\alpha_n z_C}. \tag{B.12}$$

From equation (B.6), (B.7), (B.10), and (B.12), we can write the field as

$$
\begin{aligned}
A_1 &= \sum_n B_n J_1(\alpha_n r)\left(e^{-\alpha_n(z-z_c)} - \frac{e^{-\alpha_n(z+z_c)}}{1+\frac{2\alpha_n\lambda_\omega^2}{d}} \right) \\
A_2 &= \sum_n B_n J_1(\alpha_n r)\left(e^{-\alpha_n(z_c-z)} - \frac{e^{-\alpha_n(z+z_c)}}{1+\frac{2\alpha_n\lambda_\omega^2}{d}} \right). \\
A_3 &= \sum_n B_n J_1(\alpha_n r)\frac{e^{-\alpha_n(z_c-z)}}{1+\frac{d}{2\alpha_n\lambda_\omega^2}}
\end{aligned}
\tag{B.13}
$$

Since the electric field $\vec{E} = -\frac{\partial \vec{A}}{\partial t}$, and $V = i\omega MI$, the mutual inductance for coils at (r_c, z_c) and (r_r, z_r) on opposite sides of the film is

$$
M = 2\pi\mu_0 \frac{r_r r_c}{r_s^2} \sum_n \frac{J_1(\alpha_n r_c) J_1(\alpha_n r_r)}{\alpha_n \left[J_2(\alpha_n r_s) \right]^2} \frac{e^{-\alpha_n(z_c - z_r)}}{1+\frac{d}{2\alpha_n\lambda_\omega^2}}. \tag{B.14}
$$

References

[1] T. Timusk, B. Statt, Rep. Prog. Phys. **62**, 61 (1999).
[2] V. J. Emery, S. A. Kivelson, Nature **374**, 434 (1995).
[3] Y. J. Uemura, Phys. Rev. Lett. **62**, 2317 (1989).
[4] J. M. Tranquada *et al*. Nature **375**, 561 (1995). M. V. Zimmerman et al. Europhys. Lett. **41**, 629 (1998). K. Yamada *et al*. Phys. Rev. B **57** 6165 (1998).
[5] V. J. Emery, S. A. Kivelson, and O. Zachar, Phys. Rev. B **56**, 6120 (1997). V. J. Emery, S. A. Kivelson, and O. Zachar, Physica C **282**, 174 (1997). V. J. Emery and S. A. Kivelson, J. Phys. Chem. Solids **59**, 1705 (1998).
[6] K. Ghiron, M. B. Salamon *et al*. Phys. Rev. B **46**, 5837 (1992). K. Ghiron, M. B. Salamon *et al*. Phys. Rev. B. **48**, 16188 (1993).
[7] J. W. Loram *et al*., J. Supercon. **7**, 243 (1994).
[8] Sudip Chakravarty, R. B. Laughlin, Dirk K. Morr, Chentan Nayak, cond-mat/0005443.
[9] J. L. Tallon, J. W. Loram, *et al.*, Phys. Stat. Sol. **215**, 531 (1999).
[10] J. L. Tallon, J. W. Loram, cond-mat/0005063 (2000).
[11] J. L. Tallon *et al*.,Phys. Rev. Lett. **74** 1008 (1995).
[12] C. Bernhard, *et al*. Phys. Rev. Lett. **86** 1614 (2001).
[13] C. Panagopoulos, *et al*. Phys. Rev. B **60**, 14617 (1999).
[14] Z. A. Xu, N. P. Ong, Y. Wang, T. Kakeshita, and S. Uchida, Nature **406**, 486 (2000).
[15] J. Corson, R. Mallozzi, J. Orenstein, J. N. Eckstein, and I. Bozovic, Nature **398**, 221 (1999).
[16] C. Maingast, V. Pasler, P. Nagel, A. Rykov, S. Tajima, and P. Olsson. Phys. Rev. Lett. **86**, 1606 (2001).
[17] J. Mesot, M. R. Norman, H. Ding, *et al.*, **83**, 840 (1999). A. J. Millis, S. M. Girvin, L. B. Ioffe, A. I. Larkin, **59**, 1742 (1998).
[18] D. S. Fisher, M. P. A. Fisher, and D. A. Huse, Phys. Rev. B **43**, 130 (1991).
[19] E. W. Carlson, S. A. Kivelson, V. J. Emery, and E. Manousakis, Phys. Rev. Lett. **83**, 612 (1999).
[20] A. Paramekanti, M. Randeria, T. V. Ramakrishnan, S. S. Mandal, cond-mat/0002349.
[21] S. Tewari, H.Y. Kee, C. Nayak, and S. Chakravarty, cond-mat/0101027.
[22] V. M. Krasnov, et al. Phys. Rev. Lett. **84**, 5860 (2000). M. Ya Amusia and V. R. Shaginyan, cond-mat/0102252.
[23] P. M. Chaikin and T. C. Lubensky, *Principles of Condensed Matter Physics*, 288, Cambridge University Press (1995).
[24] M. Tinkham, *Introduction to Superconductivity*, 321, McGraw-Hill (1996).
[25] J. C. Martinez, S. H. Brongersma, A. Koshelev, B. Ivlev, P. H. Kes *et al*., Phys. Rev. Lett. **69**, 2276 (1992).
[26] W. J. Skocpol and M. Tinkham, Rep. Prog. Phys. **38**, 1049 (1975).
[27] J. M. Kosterlitz, D. J. Thouless, J. Phys. C **6**, 1181 (1973). J. M. Kosterlitz, J. Phys. C **7**, 1046 (1974). V. L. Berezinskii, JETP **34**, 610 (1972).
[28] D. J. Bishop, J. D. Reppy, Phys. Rev. Lett. **40**, 1727 (1978).
[29] D. W. Abraham, C. J. Lobb, M. Tinkham, and T. M. Klapwijk, Phys. Rev. B **26**, 5268 (1982).
[30] A. F. Hebard, A. T. Fiory, Phys. Rev. Lett. **44**, 291 (1980). K. Epstein, A. M. Goldman, A. M. Kadin, Phys. Rev Lett. **47**, 534 (1981). K. Epstein, A. M. Goldman, A. M. Kadin, Phys. Rev B **26**, 3950 (1982). A. M. Kadin, K. Epstein, A. M. Goldman, Phys. Rev B **27**, 6691 (1983).
[31] B. Jeanneret, Ph. Fluckiger, J. L. Gavilano, et al. Phys. Rev. B **40**, 11374 (1989).
[32] M. R. Beasley, J. E. Mooij, T. P. Orlando, Phys. Rev. Lett. **42**, 1165 (1979).
[33] V. Ambegaokar, B. I. Halperin, D. R. Nelson, E. D. Siggia, Phys. Rev. B **21**, 1806 (1980).
[34] P. Minnhagen, Rev. Mod. Phys. **59**, 1001 (1987).
[35] S. E. Inderhees, M. B. Salamon, J. P. Rice, and D. M. Ginsberg, Phys. Rev. Lett. **66**, 232 (1991).
[36] A. T. Dorsey, Phys. Rev. B **43**, 7575 (1991).
[37] For an introduction see: N. Goldenfeld, "Lectures on Phase Transitions and the Renormalization Group", Perseus Books (1992).
[38] The classification of dynamics, *e.g.* Model A and Model E, is addressed in: P. C. Hohenberg and B. I. Halperin. Rev. Mod. Phys. **49**, 435 (1977).

[39] Private Communication, Nigel Goldenfeld
[40] B. Chattopadhyay and S. R. Shenoy, Phys. Rev. Lett. **72** 400 (1994).
[41] G. Blatter, M. V. Feigel'man, V. B. Geshkenbein, A. I. Larkin, V. M. Vinokur, Rev. Mod. Phys. **66**, 1125 (1994).
[42] S. Kamal, D. A. Bonn, N. Goldenfeld, P. J. Hirshfeld, Ruixing Liang, W. N. Hardy, PRL **73** 1845 (1994).
[43] D. I. Glazman, A. E. Koshelev, JETP **70**, 774 (1990).
[44] A. F. Hebard, A. T. Fiory, Phys. Rev. Lett. **44**, 291 (1980).
[45] J. Y. Lee, K. M. Paget, T. R. Lemberger *et al*., Phys. Rev. B **50**, 3337 (1994). J. Y. Lee, K. Paget, T. R. Lemberger *et al*., **71** 1605 (1995).
[46] K. M. Paget, S. Guha, M Z. Cieplak, I. E. Trofimov, S. J. Turneaure, T. R. Lemberger, **59**, 641 (1999)
[47] C. W. Schneider, Z. H. Barber, J. E. Evetts, *et al*., Physica C **233**, 77 (1994).
[48] Z.-H. Lin, G. C. Spalding, A. M. Goldman, et al., Europhys. Lett. **32**, 573 (1995).
[49] K. M. Paget, B. R. Boyce, T. R. Lemberger, Phys. Rev. B **59**, 6545 (1999).
[50] A. T. Fiory, A. F. Hebard, P. M. Mankiewich, R. E. Howard, Appl. Phys. Lett. **52**, 2165 (1988). A. T. Fiory, A. F. Hebard, P. M. Mankiewich, R. E. Howard, Phys. Rev. Lett. **61**, 1419 (1988).
[51] A. T. Fiory, A. F. Hebard, W. I. Glaberson, Phys. Rev. B **28** 5075 (1983).
[52] A. Yazdani, "Phase Transitions in Two-Dimensional Superconductors", Thesis, Standford University (1994). S. J. Turneaure, T. R. Lemberger, J. M. Graybeal, Phys. Rev. Lett. **84**, 987 (2000).
[53] J. H. Claassen, J. E. Evetts, R. E. Somekh, Z. H. Barber, Phys. Rev. B **44**, 9605 (1991).
[54] C. W. Schneider. R. E. Somekh, J. E. Evetts, et al., IEEE Trans. Appl. Supercond. **5** 1432 (1995).
[55] R. C. Taber, Rev. Sci. Instrum. **61**, 2200 (1990). S. M. Anlage, B. W. Langley, G. Deutscher, J. Halbritter, and M. R. Beasley, Phys. Rev. B **44**, 9764 (1991).
[56] A. Porch, M. J. Lancaster, and R. G. Humphreys, IEEE Trans. MTT **43**, 306 (1995).
[57] M. C. Nuss and J. Orenstein in Millimeter and Submillimeter Spectroscopy of Solids 7-50 (Topics in Applied Physics Vol. 74, Springer, New York, 1998).
[58] Private Communication, J. Orenstein
[59] A. Umezawa, G. W. Crabtree, *et al*. Phys. Rev. B **38**, 2843 (1988).
[60] M. Niderost, R. Frassanito, *et al*. Phys. Rev. Lett. **81**, 3231 (1998).
[61] C. V. Dodd, W. E. Deeds, Jour. Appl. Phys. **39,** 1819 (1968).
[62] J. R. Clem, M. W. Coffey, Phys. Rev. B **46**,14662 (1992).
[63] M. W. Coffey, Jour. Appl. Phys. **87**, 4344 (2000).
[64] S. J. Turneaure, A. A. Pesetski, T. R. Lemberger, Jour. Appl. Phys. **83**, 4334 (1998).
[65] J. H. Claassen, M. L. Wilson, J. M. Byers, S. Adrian, J. Appl. Phys. **82**, 3028 (1997).
[66] A. B. Pippard, Supercond. Sci. Technol. 7, 696 (1994).
[67] J. H. Claassen, J. E. Evetts, R. E. Somekh, Z. H. Barber, Phys. Rev. B **44** 9605 (1991).
[68] Private Communication: J. R. Clem, M. W. Coffey, T. Lemberger, and A. F. Hebard.
[69] I acknowledge S. Kos, D. Sheehy, R. Ramazashvili, and M. Stone for helpful discussions on mathematical issues related to fields produced by a finite-diameter film.
[70] A. T. Fiory and A. F. Hebard, pp 437 , "Magnetic Susceptibility of Superconductors and Other Spin Systems", ed. R. A. Hein, Plenum Press (1991).
[71] S. J. Turneaure, E. R. Ulm, T. R. Lemberger, J. Appl. Phys. **79** 4221 (1996). S. J. Turneaure, A. A. Pesetski, T. R. Lemberger, J. Appl. Phys. **83** 4334 (1998).
[72] W. N. Hardy, D. A. Bonn, *et al*. **70**, 3999 (1993). D. A. Bonn, S. Kamal, *et al*. **50**, 4051 (1994).
[73] J. E. Sonier, R. F. Kiefl., *et al*. **72**, 744 (1994).
[74] C. Panagopoulos, J. R. Cooper, T. Xiang, *et al*. **57**, 13422 (1998).
[75] S. Kamal, Ruixing Liang, A. Hosseini, D. A. Bonn, W. N. Hardy, PRB **58** R8933 (1998).
[76] H. Srikanth, Z. Zhai and S. Sridhar, PRB **57** 7986 (1998).
[77] J. Annett, N. Goldenfeld, S. R. Renn, Phys. Rev. B **43**, 2778 (1991). P. J. Hirschfeld, N. Goldenfeld, Phys. Rev. B **48**, 4219 (1993).
[78] B. Boyce, K. M. Paget, T. R. Lemberger cond-mat/9907196.
[79] Zhanxiang Ma, R. C. Taber, L. W. Lombardo, A. Kapitulnik, M. R. Beasley, *et al*. Phys. Rev. Lett. **71**, 781 (1993).
[80] D. A. Bonn, and W. N. Hardy in *Physical Properties of High Temperature Superconductors V*, Ed. D. M. Ginsberg, (1996).
[81] T. Jacobs, S. Sridar, Qiang Li, G. D. Gu., N. Koshizuka, Phys. Rev. Lett. **75**, 4516 (1995).

[82] Shih-Fu Lee, D. C. Morgan, R. J Ormeno, D. M. Broun, R. A. Doyle, J. R. Waldram, K. Kadowaki, Phys. Rev. Lett., **77**, 735 (1996).
[83] V. G. Kogan *et al*. Phys. Rev. Lett. **70**, 1870 (1993).
[84] J. N. Eckstein, I. Bozovic, Annu. Rev. Mater. Sci. **25** 679, (1995).
[85] The miscut angle from the manufacturer specifies a miscut angle less than 0.2 degrees and Bruce Davidson has measured the a miscut angle of 0.1 to 0.2 degrees on substrates from the manufacturer.
[86] H. Kitano, K. Kinoshita, Y. Tasuchiya *et al*. Proc. of the 12th Intnl. Sym. On Superconductivity (ISS'99) Springer Verlag 268 (2000).
[87] J. Annett, N. Goldenfeld, S. R. Renn, Phys. Rev. B **43**, 2778 (1991). P. J. Hirschfeld, N. Goldenfeld, Phys. Rev. B **48** 4219 (1993).
[88] T. Xiang, J. M. Wheatley, Phys. Rev. Lett. **76**, 134 (1996).
[89] Ming Xu *et al*., Appl. Supercond. **1** 1547 (1993). Peter Majewski *et al*., Jour. Electr. Mater. **24** 1937 (1995).
[90] K. Knizek, E. Pollert, *et al*. Physica C, **216** 211 (1993).
[91] Private communication with Harry Westfahl.
[92] P. Minnhagen Rev. Mod. Phys. **59** 1001 (1987). V. Amgegaokar, B. I. Halperin, D. R. Nelson, E. D. Siggia, Phys. Rev. B **21** 1806 (1980).
[93] M. Wallin, Phys. Rev. B **41** 6575 (1990).
[94] M. Cappezzali, H. Beck, S. R. Shenoy, Phys. Rev. Lett. **78** 523 (1997).
[95] T. Senthil, M. P. A. Fisher, cond-mat/0006481. T. Senthil, M. P. A. Fisher, cond-mat/0008082.
[96] J. E. Mooij p.325-370 in "Percolation, Localization, and Superconductivity." Proceedings of a NATO Advanced Study Institute. Plenum, New York, NY (1984)
[97] Private Communication with T. Senthil
[98] Ch. Niedermayer, C. Bernhard, *et al.* Phys. Rev. Lett. **71** 1764 (1993).
[99] C. Bernhard, Ch. Niedermayer, *et al*. Phys Rev. B **52** 10488 (1995). D. R. Harshman and A. T. Fiory Phys. Rev. Lett. **72** 2501 (1994).
[100] J. P. Locquet, Y. Jaccard, *et al*. Phys. Rev. B **54** 7481 (1996).
[101] G. Villard, D. Pelloquin, *et al*. Phys. Rev. B **58** 15231 (1998).
[102] M.R. Presland *et al.*, Physica C **165**, 391 (1991).
[103] M. A. Howson, N. Overend, and Ian D. Lawrie Phys. Rev. B **51**, 11984 (1995).
[104] M. B. Salamon, Jing Shi, N. Overend, M. A. Howson, Phys. Rev. B **47**, 5520 (1993).
[105] N.-C. Yeh, W. Jiang, D. S. Reed, and U. Kriplani, Phys. Rev. B **47**, 6146 (1993).
[106] J. T. Kim, N. Goldenfeld, J. Giapintzakis, D. M. Ginsberg, Phys. Rev. B. **56**, 118 (1997).
[107] M. B. Salamon and J. Shi, Phys. Rev. Lett. **69**, 1622 (1992).
[108] N. Overend, M. A. Howson, and I. D. Lawrie, Phys. Rev. Lett. **75**, 1870 (1995). M. A. Howson, I. D. Lawrie, and N. Overend, Phys. Rev. Lett. **74**, 1888 (1995). N. Overend, M. A. Howson, and I. D. Lawrie **72**, 3238 (1994).
[109] Steven M. Anlage, J. Mao, J. C. Booth, Dong Ho Wu, J. L. Peng, PRB **53** 2792 (1996).
[110] R. Menegotto Costa, P. Pureur, *et al*. Phys. Rev. B **56** 10836 (1997).
[111] W. E. Lawrence and S. Doniach, in Proc. of the 12th Intnl. Conf. on Low Temp. Phys., Ed: E. Kanda (Keigaku, Tokyo, 1971), p. 361.
[112] S. H. Han, Yu. Eltsev, and O. Rapp. Jour. Low Temp. Phys. **117** 1259 (1999).
[113] L. Miu *et al*. Phys. Rev. B **57** 3144 (1998). G. Balestrino, *et al*. Phys. Rev. B **51** 9100 (1995). Y. M. Wan. S. E. Hebboul, D. C. Harris, and J. C. Garland Phys. Rev. Lett. **71** 157 (1993). S. Martin, A. T. Fiory, R. M. Fleming. G. P. Espinosa, and A. S. Cooper Phys. Rev. Lett. **62** 677 (1989). S. N. Artemenko, I. G. Gorlova, Y. I. Latyshev, Phys. Lett. A **138** 428 (1989).
[114] J. Kotzler, M. Kaufmann, Phys. Rev. B **56**, 13734 (1997).
[115] T. Ito, K. Takenaka, and S. Uchida, Phys. Rev. Lett. **70**, 3995 (1993).
[116] T. Watanabe, T Fujji, and A. Matsuda, Phys. Rev. Lett. **79**, 2113 (1997).
[117] C. Carballeira, S. R. Curras, Jose Vina, *et al*. Phys. Rev. B. **63** 144515 (2001).
[118] S. H. Han, Yu. Eltsev, O. Rapp, Phys. Rev. B **57** 7510 (1998).
[119] S. H. Han, Yu. Eltsev, O. Rapp, J. Low Temp. Phys. **117** 1259 (1999). S. H. Han, Yu. Eltsev, O. Rapp, Phys. Rev. B **61** 11776 (2000).
[120] R. A. Wickham and A. T. Dorsey Phys. Rev. B **61** 6945 (2000).
[121] S. W. Pierson, M. Friesen, *et al*. Phys. Rev. B. **60** 1309 (1999).

[122] L. Miu, P. Wagner, *et al*. Phys. Rev. B **52** 4553 (1995).
[123] K. Moloni, M. Friesen, *et al*. Phys. Rev. B **56** 14784 (1997).
[124] Earlier work in the following reference found z=1.25. K. Moloni, M. Friesen, *et al*. Phys. Rev. Lett. **78** 3173 (1997).
[125] V. Aji and N. Goldenfeld, cond-mat/0105622.
[126] J. Lindmar et al., Phys. Rev. B **58**, 2827 (1998). H. Weber and H. J. Jensen, Phys. Rev. Lett. **78**, 2620 (1997).
[127] The scaling formula was derived by Vivek Aji as suggested by Nigel Goldenfeld.